MASTER THESIS

QUANTIFICATION AND OPTIMIZATION OF METAL ARTEFACT REDUCTION IN HIP PROSTHESES IMAGING USING NOVEL CT-TECHNIQUES

R.H.H. Wellenberg

TNW/TECHNICAL MEDICINE

PROF.DR.IR. C.H. SLUMP

EXAMINATION COMMITTEE
Drs. M.F. Boomsma
Drs. N.S. Cramer - Bornemann
Prof.dr.ir. H.F.J.M. Koopman
Ir. J.A.C. van Osch
Prof.dr.ir. C.H. Slump

UNIVERSITY OF TWENTE.

15-04-2015

Abstract

Quantification and optimization of metal artefact reduction in hip prostheses imaging using novel CT-techniques.

Purpose: To quantify the value of three novel CT-techniques: iterative model-based reconstruction (IMR), orthopaedic metal artefact reduction algorithm (O-MAR) and virtual monochromatic Spectral CT-imaging in the CT-imaging of metal hip prostheses.

Methods and Materials: A water-filled phantom was used made of PMMA containing different prostheses surrounded by 18 hydroxyapatite pellets representing bone. Scans were acquired on the 256-slice iCT scanner and the 128-slice Spectral IQon CT-scanner at various dose-levels and kVp-settings. Images were reconstructed with filtered back projection (FBP), iterative reconstruction (IR, iDose^4) and model-based iterative reconstruction (IMR). Polychromatic images were reconstructed with and without the use of O-MAR. Spectral virtual monochromatic images were analysed and high keV (max 200 keV) monochromatic images were compared to monochromatic images of 70 and 74 keV, which are the effective energies of polychromatic images acquired at 120 and 140-kVp. In order to determine the degree of metal artefacts and metal artefact reduction (MAR) image quality parameters: mean Hounsfield Unit (HU), noise [HU] and contrast-to-noise-ratio (CNR) of all pellets with and without the insertion of different prostheses were calculated and analysed using a standardized measurement template.

Results: At all dose-levels and kVp settings, mean CNRs are statistically higher ($p<0.001$) and noise levels [HU] are statistically lower ($p<0.001$) for IMR relative to FBP and iDose^4 reconstructions. A categorisation into four degrees in metal artefacts is made: no, mild, moderate and severe artefacts. O-MAR is capable of substantially reducing metal artefacts. O-MAR is most effective at 140-kVp, for severe artefacts and when combined with IMR ($p<0.005$) resulting in the greatest HU, noise and CNR corrections towards baseline values of unaffected pellets. Virtual monochromatic imaging reduces metal artefacts by reducing beam-hardening effects and streak artefacts and is most effective for moderate artefacts. High-keV monochromatic imaging decreases deviations in mean HUs, noise and CNRs of by metal artefact affected pellets but results in a reduced overall image contrast. With the use of IMR and O-MAR, acceptable CNR and noise levels are maintained with a reduction in radiation dose of 80% relative to current clinical practice.

Conclusions: Image quality with IMR is superior compared to FBP and iDose^4 at all dose levels and kVp settings. IMR combined with O-MAR significantly improves CNR and reduces noise and metal artefacts in the CT-imaging of metal hip prostheses. O-MAR is more effective in MAR compared to high-keV monochromatic imaging and it is most effective at 140-kVp and when combined with IMR. Virtual monochromatic imaging reduces beam-hardening effects and streak artefacts but is incapable of reducing metal artefacts caused by photon-starvation, unlike O-MAR. IMR combined with O-MAR allows for significant radiation dose reduction of 80% while maintaining sufficient image quality. This research fuels the necessity of combining O-MAR, IMR and Spectral CT in prosthetic imaging. Further clinical validation is needed to give more insights in the additional value of these techniques in clinical practice.

Acknowledgements

After conducting two 2 of the 4 M2 internships at the nuclear medicine and orthopaedics departments at Isala Clinics Zwolle my ambition and preference was to execute my graduation internship on an imaging topic due to previous positive clinical and technical experiences. The increasing research interests within the radiology department raised the idea of facilitating internships for Technical Medicine students. Radiologist Martijn Boomsma composed a research proposal in collaboration with two medical physicists Jochen van Osch and Dr. Jorn van Dalen in line with the existing research agreement with Philips.

First of all, I would like to thank my medical supervisor and driving force of research within the Radiology department radiologist Martijn Boomsma. He and his radiologist colleagues gave me the opportunity to execute my graduation research at their radiology department in the first place. Martijn also gave me the unique opportunities to go to Haifa to acquire scans, to go to users meetings and to present the first part of my graduation research at the European Congress of Radiology in Vienna this year. It would have been unable to achieve what I have achieved during this graduation research without his intellectual input, supervision and stimulating and enthusiastic guidance during the project.

Secondly, I thank medical physicist Jochen van Osch who provided great technical input, feedback and guidance during the entire project. The weekly consults helped me to focus and to keep the important goals and aims in mind. One of the reasons to execute my graduation internship at Isala was the great technical supervision by the medical physicists department in the previous M2 internship.

I would also like to thank head of the graduation committee and technical supervisor Prof. Kees Slump. Your lectures and supervision in previous internships and especially during my graduation research had a large contribution to the final results. The intellectual talks at the University of Twente were valuable and pleasant. I hope to continue our collaboration during the planned PhD trajectory.

I thank my supervisor profession behaviour Nicole Cramer-Bornemann for the pleasant guidance during all the master internships. The scheduled meetings with other students and the reflection reports made me realise and think about important competencies which where valuable in the process of becoming a Technical Medicine graduate. I am grateful for supporting and providing the opportunity of executing part-time internships during my short 2-year professional soccer adventure. Dr. Marleen Groenier, thank you for being part of the graduation committee replacing Nicole.

I would also like to thank the external member of the graduation committee Prof. Bart Koopman for your interests in this master thesis and for taking the time and effort for being part of the graduation committee.

Special thanks goes to the people of Philips that I have been involved with. Leon de Vries facilitated the essential Philips part of the internship by arranging scan possibilities in Haifa and reconstruction possibilities in Best. The close collaboration with CT specialists Dr. Alain Vlassenbroek and Dr. Julien Milles was essential during the entire project. Thank you both for the intellectual, detailed and always quick feedback, and thank you Alain for going to Israel with me. Also thanks to Prof. Sosna and Romam Zimam from Hadassah Medical Centre Jerusalem for the guidance and the possibility to scan at their scanner in Israel. I would also like to

thank application specialist Walter Giepmans from Philips Best for helping me with the large amount of reconstructions.

I would also like to thank all of my Isala colleagues and in particular Robbert Smit and Niek Warringa for helping me with the many phantom scans and initial setups. Also thanks to epidemiologist Dr. Mireille Edens for helping me with the statistical analyses of the large datasets.

I thank Prof. Mario Maas and Dr. Geert Streekstra from the AMC who provided external intellectual guidance based on the collaboration between Isala and AMC in previous studies and the PhD trajectory of radiologist Martijn Boomsma.

En natuurlijk wil ik graag mijn ouders Gerard en Hermien en broertje Tim bedanken. Zonder jullie financiële steun was het voor mij onmogelijk om deze studie succesvol af te ronden. Naast dat jullie mij de kans gaven om te studeren boden jullie mij altijd een fijn thuis. Enorm bedankt hiervoor!

Many thanks to all of you!

Ruud

Abbreviations and Acronyms

Al	Aluminium
ANOVA	Analysis of variance
ART	Algebraic reconstruction technique
BMI	Body-mass-index
CNR	Contrast-to-noise-ratio
Co	Cobalt
Cr	Chrome
CT	Computed tomography
CTDI	Computed tomography dose index
DECT	Dual-energy computed tomography
DLP	Dose length product
FBP	Filtered-back-projection
FOV	Field of view
HA	Hydroxyapatite
HU	Hounsfield unit
IMR	Iterative model-based reconstruction
IR	Iterative reconstruction
keV	Kilo electron-volts
kV	Kilo-voltage
kVp	Peak kilo voltage
mAs	Mill ampere-second
MBIR	Model-based iterative reconstruction
mGy	Milligray
Mo	Molybdenum
MoM	Metal-on-metal
MRI	Magnetic resonance imaging
O	Oxygen
O-MAR	Orthopaedic metal artefact reduction
PET	Positron emission tomography
PMMA	Poly-methyl-methacrylate
ROI	Region of interest
SD	Standard deviation
SNR	Signal-to-noise ratio
STD	Standard reconstruction
STP	Standard pressure
THA	Total hip arthroplasty
Ti	Titanium
UHMWPE	Ultra-high-molecular-weight-poly-ethylene
Va	Vanadium
WED	Water equivalent diameter
Y	Yttrium
Z	Zirconia

Table of contents

1 Introduction

Technical innovations in CT imaging are introduced regularly. Two potentially major innovations recently introduced by Philips are Spectral CT (IQon) and iterative model-based reconstruction (IMR). Full validation, exploration and quantification of the effects and benefits for different applications has yet to be done. The main focus of this graduation research lays on investigating the impact of these technologies on metal artefacts caused by orthopaedic hip prostheses likely to occur in clinical practice, and on the reduction of metal artefacts using an orthopaedic metal artefact reduction algorithm (O-MAR). The additional value of the model-based iterative reconstruction technique IMR, the orthopaedic metal artefact reduction algorithm O-MAR and the use of virtual monochromatic Spectral CT-imaging in the suppression of metal artefacts is quantified using different metal hip prostheses, kVp settings and dose-levels.

An extensive quantitative phantom analysis is performed using several different metal prostheses in a unilateral and bilateral configuration. Scans were acquired on a 256-slice CT-scanner at Isala Clinics Zwolle and on a Spectral CT-scanner located in Haifa, one of the three available 128-slice Spectral CT-scanners worldwide. Reconstructions and further analyses took place at Isala Clinics Zwolle, Philips Haifa, Philips Best and the University of Twente.

2 Clinical relevance

Hip replacement surgery, or hip arthroplasty, significantly improves the quality of life of millions of people worldwide. Due to the high incidence of hip failure and increasing varieties regarding hip prostheses, quality assurance is essential. There is a great variety of hip prosthesis based on different composites, geometrics and shape regarding cup, head and stem. Total hip arthroplasty (THA) involves either the total replacement of the femoral head as well as neck and the acetabulum by separate prosthesis, or a resurface replacement of a double cup resurfacing arthroplasty where only resurfacing of the femoral and the acetabular articular surfaces with metal cups is done (1). Various complication can emerge after hip replacement surgery such as: aseptic loosening, particle disease (osteolysis), infection, component wear, dislocation, fracture, heterotopic ossification, metal-induced reactive mass, abductor muscle tear, iliopsoas impingement and muscle atrophy (1).

The incidence of pseudo-tumours or capsule reactions increases in particular due to an increase in metal ion levels caused by MoM (metal-on-metal) prostheses (2). Therefore, the use of fully metal-based prostheses is avoided in some countries. Despite the fact that the prosthesis itself is thought not to be the cause of the problem, the articulating surfaces between especially the stem and head, referred as taper wear, seems to be the problem (3,4). The increasing incidence of failures and complications leads to an increasing need of an early and reliable diagnosis. A recent study by Bosker et al. (2015) confirmed a high incidence of pseudo-tumours in 219 of the 626 included patients treated with large head metal-on-metal total hip arthroplasty, therefore advising proper cross sectional imaging as the mean screening tool during follow-up (4).

Medical imaging can provide important clinical information to determine the success rates of surgically implanted hip prostheses. In computed tomography (CT) imaging metallic composites can cause severe artefacts, especially in case of a large Metal-on-Metal hip prostheses used for total hip arthroplasties. Photon detection is severely distorted due to photon-starvation, beam-hardening and scatter resulting in sub-optimal image quality, illustrated in Figure 2.2. A reliable diagnose of pseudo-tumours, capsular reactions and other soft tissue pathologies is difficult or even impossible. There are different ways to suppress metallic artefacts interacting at several steps from data-acquisition to the actual resulting CT-image. Differences in type of scanner, tube, detectors, reconstruction technique, post-processing techniques and image presentation play an important role in the CT imaging of metallic composites.

Figure 2.1: X-ray image of a unilateral total hip arthroplasty on the left side (61).

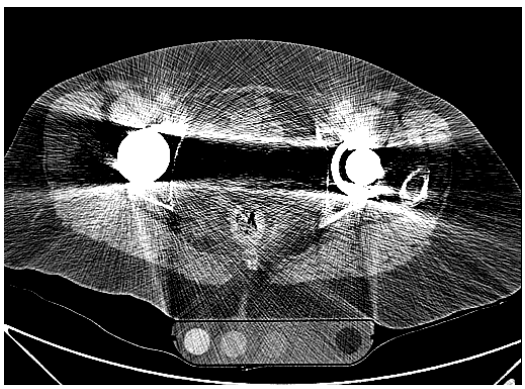

Figure 2.2: Metal artefacts in case of bilateral CT-imaging.

Philips has recently introduced potentially major innovative CT techniques with promising impact on current and future CT imaging. Full validation and exploration of the effects and benefits of the orthopaedic metal artefact algorithm O-MAR, the Dual-layer detector Spectral CT scanner and the model-based iterative reconstruction technique (IMR) has yet to be done. The possible additional value of these innovative CT techniques will be determined focussing on image quality parameters influenced by metal artefact. Further on, dose-reduction possibilities within orthopaedic CT imaging of hip prostheses will be investigated.

Several different metal artefact reduction (MAR) techniques have shown to be valuable in the suppression of metal artefacts and thereby improving qualitative and quantitative image quality with improved diagnostic confidence (5,6). Most of these MAR techniques are based on the modification of the by metal contaminated data by the replacement with data obtained from unaffected regions in the projection space (6,7). HUs are corrected towards baseline levels thereby improving subjective and objective image quality parameters (8,9). Also in radiotherapy an improved confidence in target delineation during treatment planning and position localization can be accomplished since crucial structures can be visualized using MAR techniques (6,9). Philips' O-MAR is an iterative algorithm where an output correction image is subtracted from the original input image. The resulting image can then become the new input image and the process can be repeated. With O-MAR, not only are severe streaking artefacts reduced, substantial portions of obscured anatomy can now be visualized. This new algorithm not only aims at the reduction of the most severe artefacts but also improves the low-contrast visibility close to the implant.

Recently, Boomsma et al. (2015) showed in a previous quantitative phantom study that orthopaedic metal artefact reduction (O-MAR) algorithm significantly reduces metal artefacts caused by large MoM-prostheses using standard filtered-back-projection (FBP) reconstruction and the partial iterative or hybrid reconstruction technique iDose^4 using different kVps, mAs, filter types and noise reduction levels (2).

Another potential way to suppress metal artefacts in CT is the use of Dual-Energy CT (DECT). Absorption spectra at different monochromatic energy levels retrieve additional information compared to the conventional polychromatic CT images. DECT has proven to be valuable in several areas like the subtraction of tissue, virtual unenhanced abdominal organ imaging, kidney stone characterisation, evaluation of lung perfusion defects, effective atomic number imaging, lesion characterization and optimum contrast-to-noise (CNR) imaging.

Metal artefact can be reduced using DECT due to the elimination of the beam-hardening effect (10–14). DECT showed to be valuable in reducing metal artefacts by providing a better metal-tissue separation since information of both absorption spectra is taken into account. DECT can be acquired in several ways using two detector rows, two tubes or using kVp switching. Recently, Philips introduced the IQon CT-scanner based on a dual-layer detector row technique providing simultaneous and acquisitions at both kVp settings providing perfectly synchronous projection data. It contains a single tube and detectors with simultaneous high and low energy discrimination. Its value in metal artefact reduction needs to be investigated.

The use of more advanced reconstruction techniques has proven to be of great importance especially in current clinical CT-practice focusing on low-dose imaging with improved image quality parameters. Recently, a new model-based iterative reconstruction (MBIR) called iterative model-based reconstruction (IMR, Philips Healthcare) was introduced. Standard reconstruction techniques like filtered back-projection

(FBP) are fast but produce noisy images. At low-dose FBP is not capable to suppress noise resulting in poor image quality.

First generation iterative reconstruction techniques indicated that a reduction of 23%-66% radiation dose can be achieved while maintaining the image quality (15,16). With this hybrid reconstruction technique (iDose^4, Philips Healthcare) a certain amount of image noise and artefacts is still present, especially at low-dose. The combination of providing high quality images with a great low contrast detectability and high spatial resolution within a single image remained challenging.

IMR, a full iterative model-based reconstruction, does not involve blending with FBP images during image reconstructions. Applying mathematically complex and accurate algorithms and using a model-based approach virtually noise free images can be produced. Model-based means an optimization process where within many iterations data statistics, image statistics and system models are taken into account in order to produce the best-fit image (17). Several recent studies show that model-based iterative reconstruction techniques are able to reduce image noise up to 75%-88% and radiation dose up to 75%-92% (5,18–21). Despite hip arthroplasty mostly involves older patients in which the long-term radiation risk is less of concern, the ALARA (as low as reasonably achievable) principle still holds strong especially in current healthcare.

2.1 Goals

Exploration and full validation of these innovative CT techniques, and quantifying the possible additional value of combining these techniques has yet to be done. Therefore, an extensive quantitative phantom study has been executed. The main goal of this graduation research is to quantify the additional value of IMR, O-MAR and Spectral CT in the CT imaging of metal hip prostheses. We divided our phantom study into 5 parts:

1 - Part 1 will focus on the quantitative additional value of O-MAR, IMR and the combination of both techniques relative to FBP and iDose^4 reconstructions with and without the use of O-MAR. Different kVps and mAs' will be used to determine optimal settings for the investigated techniques.
2 - Part 2 will focus on quantitative differences in mean HUs, noise and CNRs on the iCT and IQon CT-scanners in conventional polychromatic imaging. Analyses will be performed with and without the influence of metal artefacts.
3 - Part 3 will focus on the effects of monochromatic CT-imaging. 120 and 140-kVp results at conventional dose at Isala for different prosthetic configurations will be analysed focusing on mean HUs, noise and CNRs.
4 - In part 4 a quantitative analysis will be performed focusing on O-MAR and monochromatic Spectral CT imaging. Conventional images with and without the use of O-MAR will be compared to the corresponding 70 or 74 keV and 200 keV images to quantify the degree of MAR at various kVps and mAs'.
5 - In part 5, all novel CT-techniques will be taken into account. The value of individual techniques and possible combinations of techniques will be quantified based on deviations and corrections of the image quality parameters HU, noise and CNR from high to ultra-low-dose with a maximal radiation dose reduction of 80% relative to current clinical practice.

A full elaboration of the research questions and a detailed overview of sub-parts are given in "Chapter 4: Study design: research questions and objectives".

3 Background

3.1 Metal artefacts

CT imaging is superior to MRI in several diagnostic imaging areas imaging due to shorter acquisition times, good soft tissue differentiation, higher imaging resolution and its superiority in bone pathology imaging. Both MR and CT are influenced by metal artefacts due to its distorting effect on magnetic fields and high attenuation of photons. In CT, different tissue types will interact differently to the attenuation of photons. Especially materials with a high density and a high atom number will attenuate the incoming photons which will lead to a decrease of the amount of photons that will reach the detector. Increasing the intensity and the amount of the emitted photons will result in more photons reaching the detector at the opposite side of the patient, but will consequently lead to an increased patient radiation dose.

Metallic implants are known to generate bright and dark streaking artefacts and beam-hardening artefacts in CT images, as shown in Figure 3.1. These distorting artefacts impede the diagnostic imaging possibilities especially for soft tissue pathology. The metal composite itself causes beam-hardening, scatter effects or streak artefacts. Beam-hardening is caused by the absorption of the polychromatic X-ray beam while it crosses the object being radiographed, whereas the lower energy portion of the spectrum is absorbed more than that at high energy. Consequently, the beam at the exit of the object is harder than at the entrance and its spectral composition is shifted toward higher energies (22). This is a particular problem with high atomic number materials such as bone, iodine, or metal. Compared to low atomic number materials such as water, these high atomic number materials have dramatically increased attenuation at lower energies. For low energy X-rays, attenuation is caused primarily due to the photoelectric effect, and is proportional to Z^3/E^3, where Z is the atomic number, and E is the energy. At high energies, attenuation is primarily caused due to Compton scatter, and is proportional to $1/E$. Compton scatter causes X-ray photons to change direction and energy and so these X-rays end up in a different detector (23). This creates the greatest error when the scattered photon ends up in a detector that otherwise would have very few photons. In particular, if a metal implant blocks all photons, then the corresponding detector element will only detect scattered photons (24).

Beam-hardening and scatter result in dark streaks between metal, with surrounding bright streaks. Streak artefacts appear in imaging objects with a high attenuation caused by their high density and high atom number. In case of very dense metals or very large metal objects, no or hardly any photons will eventually reach the detector, which is referred as photon starvation. The high density of metal results in an attenuated beam which will impede a correct reconstruction due to gaps in projection data. The metal edges can additionally cause streaks due to under-sampling, motion, cone beam, and windmill artefacts (24).

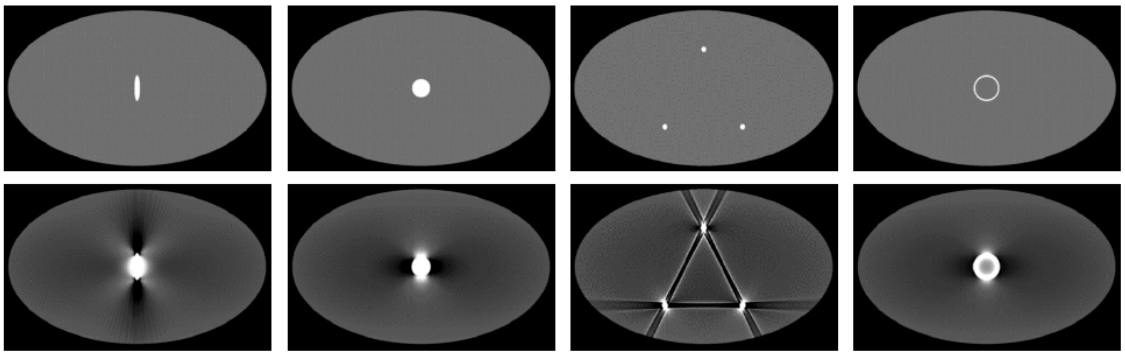

Figure 3.1: Beam-hardening artefacts due to metal parts (24). Differences in location, shape and composition of metallic parts result in various artefacts in different directions.

These metal artefacts are mostly pronounced in cases of high atomic numbers of the used composites. Cobalt-chromium (CoCr) alloy based prostheses will induce higher photon attenuation relative to stainless steel and titanium-based composites, where the less dense titanium shows the lowest photon attenuation of these three. Besides the effect of different composites, complex prostheses geometry also affects the rate of metal artefacts. Large and heavy hardware such as the femoral head and stem components produce more severe artefact than smaller pieces of hardware such as screws or plates. Thereby asymmetric hardware geometry produces non-uniform artefacts that are most severe in the direction of the greatest cross-sectional profile. The beam-hardening and scatter artefacts are most pronounced in the line with the greatest attenuation as illustrated in Figure 3.1.

3.2 Image noise

Image noise is a measure of statistical fluctuations in the image. It is a consequence of a variety of statistical processes that occur in the detection of x-rays by a CT system. There are different kinds of noise. The most important noise is caused by the quantum fluctuations in x-rays. The number of x-rays will fluctuate around a mean value according to a Poisson distribution. This fluctuation at the source results in fluctuations at the detector and in the actual image. This noise is measured by calculating the standard deviation of pixels in a ROI (region of interest). Increasing the tube current and voltage will reduce the standard deviation of the noise (25). As more quanta are detected in each measurement, the relative accuracy of each measurement improves (26). This kind of noise is called quantum noise or statistical noise.

Electronic noise is mainly generated in analogue signal processing. In processing electrical signal this will result in a small addition of noise. This kind of noise is in current CT-scanners a negligibly small part of the total amount of noise in a CT image at normal dose. An additional small contributor to the actual amount of noise is noise caused by round off errors accumulated in the reconstruction process.

A potentially large contributor to image noise is the influence of artefacts. Different kinds of artefacts impede the correct reconstruction of projection data into an actual CT image. Metal-artefacts for example will induce large streak artefacts and beam-hardening artefacts resulting in dark streaks in the image. A more detailed description will be given further on. Other artefacts are for example movement artefacts, photon starvation artefacts and ring artefacts. These kinds of artefacts do not produce random noise since this noise will be unchanged in similar repeated scans (26).

3.3 Reconstruction techniques

An important step in obtaining the actual CT image is the reconstruction of X-ray projection data acquired at different angles around the patient. During this step, attenuation information obtained by the detector located at the opposite site of the patient relative to the tube is used to generate attenuation profiles at many angles. The reconstruction process has a great impact on the image quality and therefore on radiation dose. Novel reconstruction techniques produce images with lower noise levels, thereby improving image quality. This can be translated into a radiation dose reduction since images with similar image quality parameters can be acquired at lower dose.

Improving image quality, reducing radiation dose and ease of integration into routine hospital workflow are key aspects in the development of new reconstruction algorithms (25). Dose reduction has become an essential issue in CT-imaging hence the ALARA principle.

Two major categories of methods, analytical reconstruction and iterative reconstruction (IR) are used in current clinical practice. Methods based on standard reconstruction or filtered back-projection (FBP) are the type of analytical reconstruction that is currently widely used on clinical CT scanners because of their computational efficiency and numerical stability (27). Recently, Philips introduced a model-based iterative reconstruction technique applying mathematically complex and accurate algorithms producing virtually noise free images (28). This may subsequently increase the possibilities of further decreasing radiation dose.

3.3.1 Standard reconstruction

Filtered-back-projection is a fast and robust reconstruction technique at routine radiation dose but is prone to image noise and artefacts. Dose reduction is difficult in FBP due to the rapidly increasing noise (29). FBP cannot handle the noise level when lowering the tube current and voltage resulting in a poor image quality. Remarkable progress has been made in the past few years on iterative techniques for reducing metal artefacts and noise. These techniques do not only improve image quality, but also can reduce the radiation dose, improve spatial resolution, and improve diagnosis (24). With standard reconstructions (STD), simple and fast calculations result in short reconstruction times. Nevertheless, standard reconstructions result in noisy images therefore impeding low-dose imaging. With iterative reconstruction techniques, reconstruction times are increased, dose can be lowered, noise can be decreased resulting in a high spatial and contrast resolution (30).

When lowering the dose with FBP, the variance in the photon count statistics increases. When these high levels of noise are propagated through the reconstruction algorithm, the result is an image with significant artefacts and high quantum noise (31).

Improvements were made when incorporating de-noising techniques in the image domain. Images with reduced noise could be produced helping to manage radiation dose levels (25). Nevertheless, image quality benefits were limited and artefacts associated with significantly reduced doses remained problematic. It is a cost-effective solution but with very little benefits especially at low-dose.

3.3.2 Iterative reconstruction

The basics of iterative reconstruction techniques were already founded in the early 70's. Gordon et al. developed an Algebraic Reconstruction Techniques (ART) for three-dimensional electron microscopy and X-ray photography using early iterative principles (32). Clinical possibilities were limited due to a lack of computational power at the time. Nowadays, iterative reconstruction techniques are replacing FBP as the standard of CT reconstruction.

Philips' iDose^4 is an iterative reconstruction algorithm where image data is modified through the use of mathematical models. IR is a method to reconstruct 2-dimentional and 3-dimensional images from measured projections of an object, beginning with an initial guess of the object composition and iteratively improving on it by comparing a synthesized projection from the object estimate with the acquired projection data and making incremental changes to the previous guess (33). IR techniques treat noise properly at very low signal levels, and consequently reduce the noise and artefacts present in the resulting reconstructed image (34).

With this reconstruction technique image quality is increased by reducing image noise, thereby facilitating imaging at lower dose. iDose^4 can be applied in different levels ranging from 1 to 7 with different levels of dose reduction. iDose^4 is used in a clinical setting with up to 68% resolution improvement and up to 80% dose reduction while preserving the natural appearance and preventing artefacts (31). Several studies showed that subjective and objective image quality parameters improve using iterative reconstruction techniques, therefore subsequently increasing dose reduction possibilities (35). Nevertheless, a substantial amount of image noise and artefacts are still present using a hybrid type of iterative reconstruction. Especially when combining low-dose imaging with image quality improvements, benefits with these algorithms are limited (25).

3.3.3 Model-based iterative reconstruction

Model-based iterative reconstruction realises even further noise reduction through the use novel and more computationally intensive models. FBP is a fast and robust method but it is a suboptimal algorithm choice for poorly sampled data or in cases where noise overwhelms the image signal (25). IR techniques such as IMR attempt to formulate image reconstructions as an optimization problem i.e., IR attempts to find the image that is the 'best fit' to the acquired data, while penalizing the noise.

Scanning at ultra-low-dose will eventually result in photon starvation causing ring and streak artefacts, will increase quantum mottle and extensive noise in the images. Also the visibility of small structures will decrease resulting in insufficient image quality for clinical practice.

Knowledge-based iterative reconstruction algorithms such as IMR differ from FBP methods in that the reconstruction becomes an optimization process that takes into account the data statistics, image statistics, and system models. Knowledge of the system geometry, X-ray statistics, object properties and desired characteristics are incorporated. By taking this knowledge into account, pathways are enabled between projection and image domains and real noise can be identified and reduced (28).

With Philips' IMR, an improved version of iDose^4, images are claimed to be virtually noise free (36). IR techniques such as iDose^4 and especially IMR are capable of maintaining the noise level even at a substantially

reduced radiation dose. IMR is a fully iterative reconstruction technique with no additional blending with FBP techniques. The effectiveness of noise reduction by IMR is more significant (37). Even at extreme low-dose, IMR image can keep noise in a tolerance interval. iDose^4 does not maintain sharpness at very low-dose where the minimal dose, without loss of sharpness, depends on the target organ contrast.

IMR is beneficial in improving the low contrast resolution even further while maintaining this low contrast resolution at low-dose. This results in an improved low contrast resolution and an improved spatial resolution (30). An additional downside caused by the IR methods is the on-going smoothening effect resulting in surreal looking images and a loss of contrast. Radiologists will need to get used to the virtually noise free images when using them in a clinical setting. Figure 3.2 illustrates the clearly visible improvements of diagnostic images reconstructed with the FBP, iDose^4 and IMR.

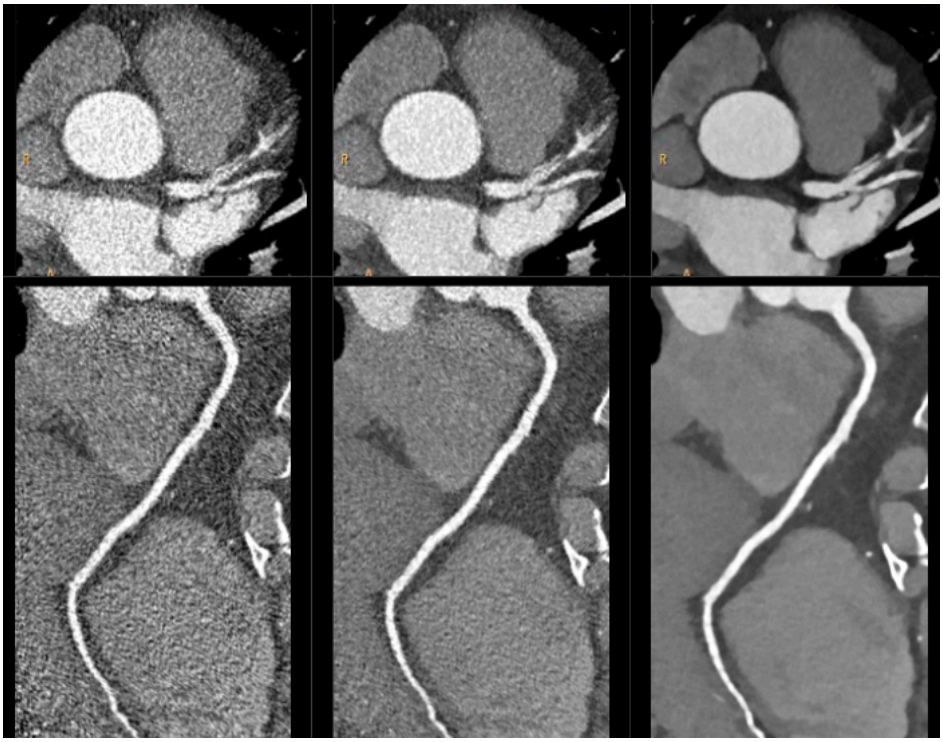

Figure 3.2: CT-imaging of coronary arteries using reconstruction techniques FBP, iDose^4 and IMR showing clearly improved image quality in case of IMR reconstructions (30).

Löve et al. (2013) conducted a phantom study quantifying image quality parameters using six different iterative reconstruction algorithms in brain CT at different radiation dose levels (38). Iterative reconstruction algorithms of different algorithms on CT systems from four different vendors including Philips' iDose^4 and IMR where investigated at four different radiation dose levels. All iterative algorithms showed a clear improvement in image quality in brain CT relative to FBP but show different strengths and weaknesses. Iterative reconstruction algorithms of Siemens and Toshiba where taken into account where GE and Philips provide model-based iterative reconstruction algorithms beside iterative reconstruction techniques. The contrast-to-noise ratio (CNR) was much higher for Philips than for GE in the low-contrast module due to a higher contrast and lower mean noise levels. Both iterative reconstruction algorithms of Philips and GE clearly improve spatial resolution where Philips' IMR is capable of reducing noise at the same time.

Specialists at the Catholic University of Leuven (UCL) performed a phantom study using the Catphan phantom using the standard reconstruction technique and the model-based iterative reconstruction technique IMR at various dose levels and slice thicknesses (39). Images were acquired at 120-kVp at four different dose levels and reconstructed with FBP and IMR level 1.

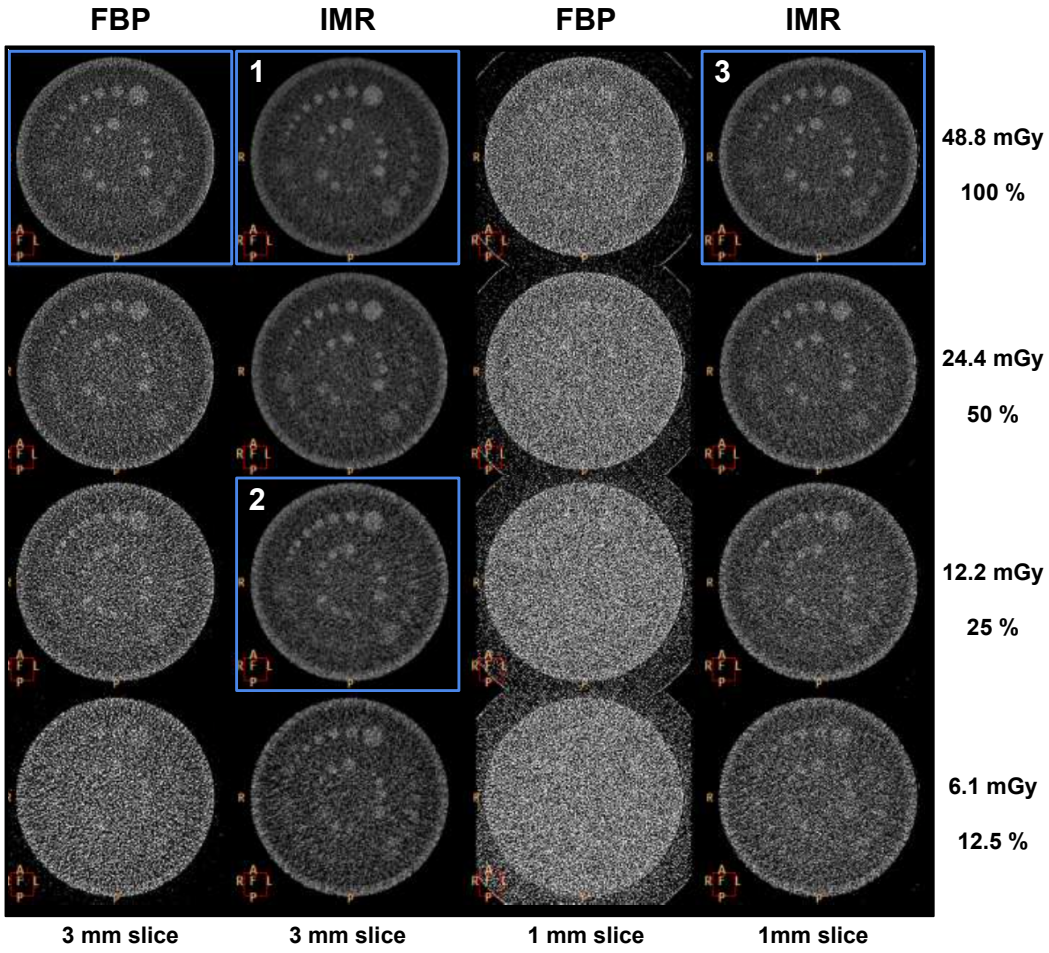

Figure 3.3: IMR versus FBP reconstructions at various dose-levels and 1 and 3 mm slice thicknesses (39). The 2 columns on the left were reconstructed with standard resolution to mimic soft tissue reconstruction in the chest. The 2 columns on the right were reconstructed with high resolution to mimic optimal lung parenchyma reconstruction in the chest. 1) IMR improves low contrast resolution. 2) With IMR, low contrast is maintained at reduced dose. 3) No compromise is needed between low contrast detectability and spatial resolution.

Figure 3.3 illustrates the three main benefits of reconstructing with IMR at different dose-levels and slice thicknesses relative to FBP images. The three main benefits of IMR are:

1) Improved low contrast resolution and detectability.
2) Low contrast maintained at reduced dose.
3) No compromise is needed between low contrast detectability and spatial resolution.

IMR is capable of improving both low contrast and spatial resolution within the same image. This results in thin slice imaging without dose penalties. Phantom tests demonstrate that IMR may simultaneously enable 60% - 80% lower radiation dose, 43% - 80% low-contrast detectability improvement, and 70% - 83% less image noise, relative to FBP. Alternatively, IMR may enable 1.2 × – 1.7 × high contrast spatial-resolution improvement; or 2.5 × – 3.6 × low contrast detectability improvement; or 73% - 90% image noise reduction, relative to FBP (25).

What the possible additional value of IMR can be in the reduction of metal artefacts in hip prosthesis imaging needs to be investigated. O-MAR, when combined with iDose^4, proved to be valuable in metal artefact reduction. Promising results are expected using IMR in this setting especially in image quality improvement and scanning at ultra-low-dose. The possible combination of IMR with O-MAR will be investigated. We want to apply IMR in low-dose CT imaging of hip prostheses and aim to evaluate its benefits for image quality improvement and investigate which lowest radiation dose level remains acceptable.

3.4 Metal artefact reduction algorithm

Distorting imaging artefacts caused by metal components can be suppressed using Philips' orthopaedic metal artefact reduction algorithm O-MAR. O-MAR is an effective iterative loop-algorithm where corrected output images are subtracted from the original image. All pixels around the HU of water (0) are classified as tissue and are set to a single value. An initial metal only projection image is created setting all other pixels to zero.

The metal only, tissue classified and input images are all forward projected to generate the corresponding sinogram data. In this way a metal only sinogram is compared to the original sinogram, illustrated in Figure 3.4, and is used to correct for imaged metal parts. This process can be repeated or iterated numerous times till this results in an acceptable image. Metal related components are in this way filtered and corrected for in the raw sinogram data before reconstruction takes place (40). Both streak and darkening effects are mitigated using O-MAR.

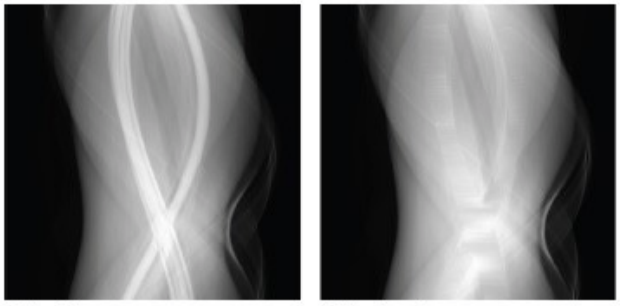

Figure 3.4: Original sinogram (left) and the metal replaced by tissue equivalent sinogram (right) (40).

An innovative aspect of this O-MAR algorithm is in the first iteration. The tissue-classified image is not produced from the original uncorrected image. Rather the metal data points in the sinogram are identified and removed. These points are replaced with interpolated values that simulate tissue in place of the metal. This sinogram is back-projected and the resulting image is used to segment tissue and create the tissue-classified image. For following iterations, this step is not executed.

With O-MAR, not only are severe streaking artefacts reduced, substantial portions of obscured anatomy can now be visualized. Using a higher kVp will have a positive result on the effect of O-MAR, therefore scanning at 140-kVp is advised. This not only decreases the impact of beam-hardening, it also decreases statistical noise which benefits the O-MAR algorithm (41).

This new algorithm not only aims at the reduction of the most severe artefacts but also improves the low-contrast visibility close to the implant. A combination of edge-preserving correction algorithms and interpolation schemes allowed for improvements in image quality far better than results from clinical CT without degrading spatial resolution (42).

Figure 3.5 illustrates the difference between the conventional and O-MAR image. Especially at the centre of the image and around the prosthesis soft tissue pathologies cannot be diagnosed correctly especially due to the

high rate of streak artefacts and beam-hardening effects. Differences are observed in the average HUs and standard deviations thus resulting in improved CNR in case of the O-MAR image (40). O-MAR only influences regions that are affected by metallic artefacts and has no influence on non-metal images.

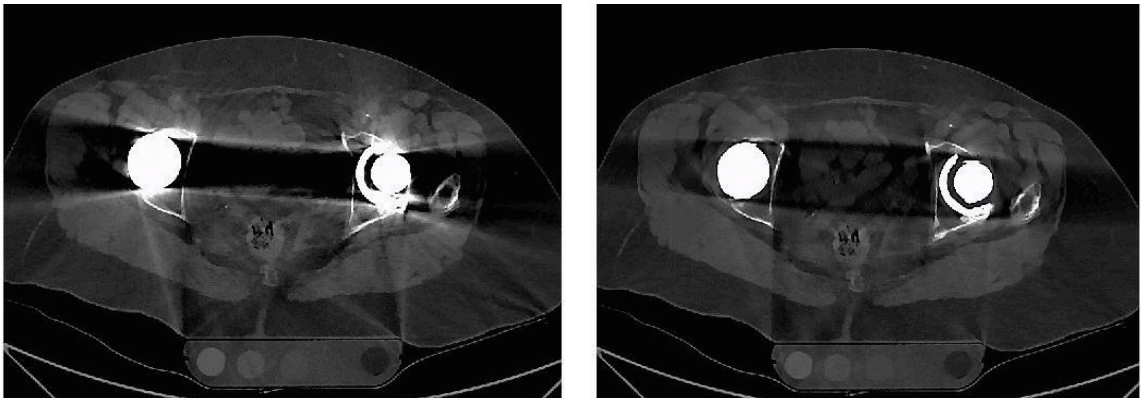

Figure 3.5: The effects of O-MAR combined with iDose^4 in a patient with large bilateral MoM-prostheses. HU, noise and CNR deviations caused by metallic components are corrected for using O-MAR.

3.5 Dual-energy Computed Tomography (DECT)

3.5.1 Developments in DECT

The introduction of dual-energy CT has provided the ability of material differentiation and tissue characterization beyond the traditional CT attenuation scale. Since differences in CT values can occur due to differences both in energy-dependent mass attenuation coefficient μ/ρ and in density ρ, this may lead to ambiguities in CT value interpretation. DECT strives for removing such ambiguities and to provide additional material- or tissue-specific information. The principle of DECT is always the same: acquire two separate attenuation data sets for the object in question and extract material-specific information from these data. The physical basis for this is given by the energy dependence of x-ray attenuation.

Dual Energy CT scans (DECT) can be acquired in several ways. Already in the 1970's, DECT was obtained by acquiring two separate scans in a sequential manner. By scanning at 80-kVp and 140-kVp for example, two different datasets with high-energy and low-energy data were obtained. Early investigators recognized the potential of DECT for improving tissue characterisation. However, the CT-scanners' hardware and software at that time were limiting factors and restricted its clinical usability (29).

Since the 1980's, two separate scans can be obtained with faster acquisition times called rapid kVp-switching where only a slight pause between both scans was needed. Around the 1990's Philips investigated the possible use of novel detectors in an experimental setting (43). In the 2000's, the use of two independent tube sources became an interesting new approach. In this way scanning simultaneously with two kV levels during a single scan became possible resulting in two datasets, referred as Dual-Source CT imaging.

In the 2010's, energy discriminating detectors were developed and formed the basics of Spectral CT imaging. In this way, data can be obtained for multiple energy intervals during a single scan by using an energy-discriminating Dual-Layer detector. This study will focus on the Dual-Layer approach, which will be highlighted further on. Photon-counting is considered as the latest and most advanced form of spectral CT. Highly efficient 'low-dose' detectors which count each individual incident x-ray and measure the energy of each photon which may facilitate k-edge imaging. Early results are promising, despite the fact that clinical photon counting would require 100 times faster detectors than currently available (44).

3.5.2 Binary separation

Scanning at low kVp will increase noise and can be problematic in the imaging of large patients. Besides noise issues, FOV limitations and image quality may affect dual–energy post-processing possibilities (45). On the other hand, scanning at two different kVp levels provides additional information including tissue characterization referred as binary separation.

As in conventional CT, DECT water is used as a reference. The binary separation in DECT is based on two effects described in the original work of Alvarez and Macovski in which X-ray interacts with matter, Compton scattering and photoelectric absorption (46).

$$\mu_x(E) = a_1\,\sigma(E) + a_2\,\tau(E) \tag{3.1}$$

In Equation 3.1, σ represents the Compton effect and τ represents the photoelectric effect. a_1 and a_2 are weights representing the sample's composition. μ_x can be described as a linear combination of any two materials because again, only σ and τ will contribute (42,46). In Equation 3.2, 1 and 2 are called basic materials and c_1 and c_2 relate to the concentration or density of the respective basis material in a given voxel. Water and calcium are practically relevant examples as choice for basis materials. Also, when focusing on separating different tissues, water and iodine, or calcium and iodine can be used (42).

$$\mu_x(E) = c_1\,\mu_1(E) + c_2\,\mu_2(E) \tag{3.2}$$

The photoelectric effect is affected by the energy level and depends on the effective atomic number (Z_{eff}) of the material. Choosing a material with a Z_{eff} below water will increase the HU with increase of energy. Bone, which has a higher Z_{eff} compared to water, will decrease the HU values with increase of energies (47). The effects of binary separation are most pronounced when differences in Z_{eff} are increased.

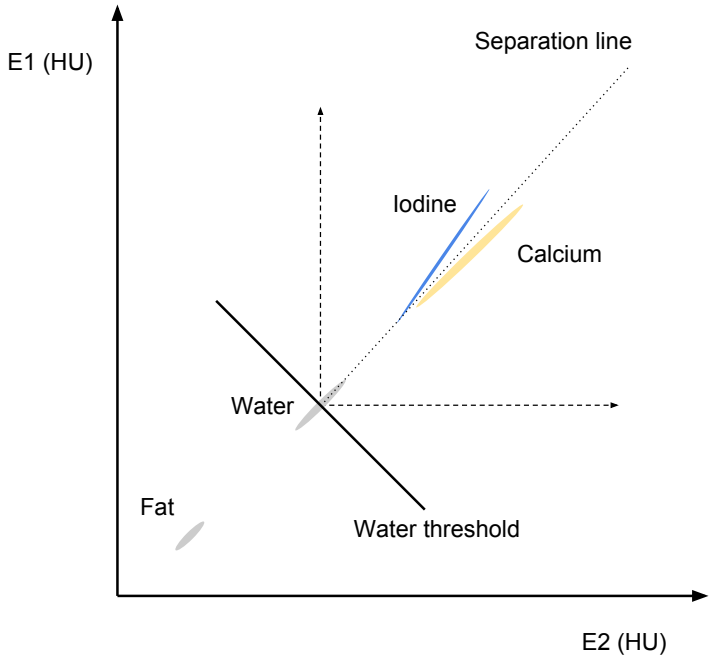

Figure 3.6: HU plot at two different energies (47). By placing voxels in an energy map with high and low energies, a separation can be made in order to obtain material specific information.

Figure 3.6 illustrates a plot of the HU values at different energies E_1 (low energies) and E_2 (high energies). The voxels are placed in an energy map with high and low energies. By plotting these voxels iodine (shown in blue) or calcium (yellow) a binary separation can be obtained. The perpendicular line indicates the threshold of water. Fat is negative, with a HU below water. When the SD or noise is small (at high dose), the cloud is clear. The SD is high at a low-dose, resulting in a large cloud where differentiation can be impossible (47).

Dual energy CT is especially useful for material characterisation. The additional clinical value of DECT especially lies in the following areas (42):

- Direct subtraction of bone
- Differentiation between plaque and contrast agent
- Virtual unenhanced abdominal organ imaging
- Kidney stone characterisation
- Visualisation of cartilage, tendons, ligaments
- Evaluation of lung perfusion defects
- Heart perfusion blood volume
- Uric acid crystal visualisation
- Lung vessel embolization
- Brain haemorrhage differentiation
- Metal artefact reduction

In the 2010's the implementation of innovative detectors further improved the possibilities of DECT. Dual-layer detectors acquire separate energy levels of a single polychromatic source in a single scan. Spectral CT is based on this principle.

3.5.3 Dual layer detectors (Spectral CT)

Dual-Energy CT can be obtained in several ways as mentioned earlier. With dual source imaging, two tubes are used in a simultaneous and non-isopedic manner where the separation is obtained in the image space. In kVp-switching DECT, scans are obtained non-simultaneously and in a non-isopedic manner where separation takes place in the projection space after temporal and angular interpolations. In Dual Spin CT, separation also occurs in image space where scans are obtained non-simultaneously and in a non-isopedic manner. With this dual detector technique different acquisition-energies are captured simultaneously and in an isopedic way and enable an exact spectral separation in the projection space without the need of spatial and temporal interpolations (47).

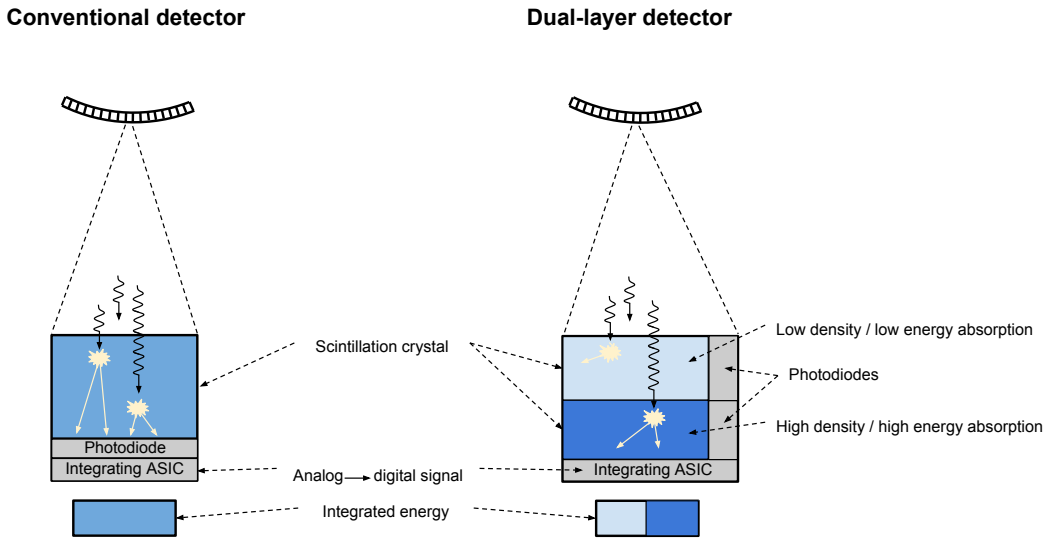

Figure 3.7: Conventional detector vs. a dual layer detector (47). Two different detector layers with low and high density absorb respectively low- and high-energy photons in case of the Dual-Layer detector principle.

The dual-layer detector, illustrated in Figure 3.7, acquires single source CT-data using two scintillation layers on top of each other. In this way, two different energy datasets are acquired simultaneously. In normal CT imaging, the entire spectrum is used containing all energies.

The dual-layer detectors separate the x-ray beam into two components resulting in two different overlapping energy windows (layer 1 and layer 2) instead of the conventional spectrum illustrated in the background in Figure 3.8. Spectral analysis can be performed from the projections acquired with the two layers separately and a conventional image sensitive to the entire spectrum can always be reconstructed summing the signals from both layers.

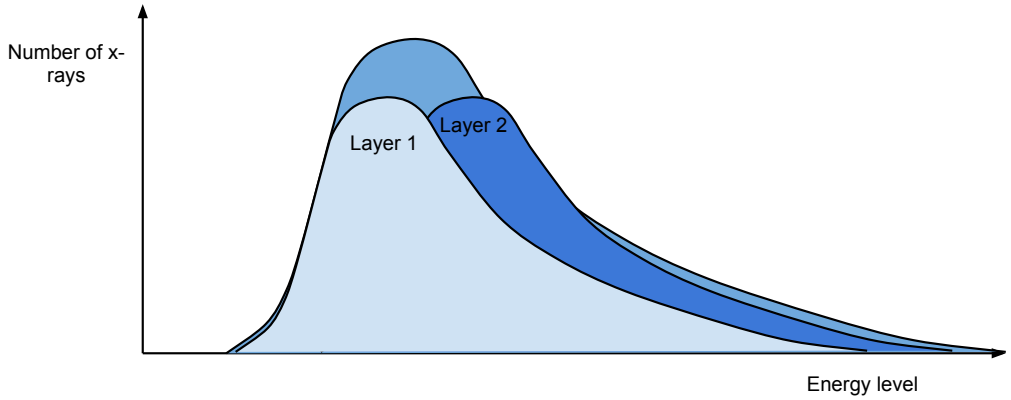

Figure 3.8: Spectrum separation (47). Layer 1 mainly absorbs low-energy photons where layer 2 absorbs the remaining high-energy photons that pass layer 1.

3.5.4 Clinical additional value of Spectral CT

With Spectral CT, monochromatic extrapolation from 40 up to 200 keV is possible. Interactions of tissue can be observed at any given keV within this range. This Spectral reconstruction method provides additional information, which can be used retrospectively and combined with the clinical information provided by the conventional reconstructions. Retrospective spectral analysis can also be used in case of incidental findings.

With Spectral CT, promising clinically valuable improvements can be achieved with extra visualization, extra information, extra IQ and extra dose saving. Contrast iodine concentrations can be decreased, x-ray dose can be minimized with improved virtual non-contrast imaging possibilities, giving the possibility to remove a non-injected scan. Also in the imaging of large patients, the additional spectral analysis results in improved image quality parameters.

In contrast to other kinds of DECT, both low and high energy x-rays are captured simultaneously without the need of additional exposure of radiation. This subsequently eliminates the time lag in case of sequential DE techniques (44). Also dual kVp imaging suffers from an inferior image quality since the low voltage scan produces very low signal at the CT detector, especially in large patients and metal implants.

3.5.5 Monochromatic imaging and the reduction of metal artefacts

The main focus of Spectral CT imaging within this research will be the additional value of Spectral CT in metal artefact reduction. At high virtual monochromatic keV, metal artefacts are reduced by reducing beam-hardening effects caused by polychromatic x-ray beams. Spectral CT imaging can result in an improved image quality in imaging metallic implants by decreasing the HU shift caused by metallic composites and boosting the image CNR. Using this dual-layer technique, raw data-based DECT is passing the raw data through a decomposition function followed by an image reconstruction. This raw data-based decomposition results in a final image without any or little beam-hardening artefacts (44). This can be a huge improvement in imaging metal implants. In principle, projection-based methods should be more effective relative to image-based methods in terms of beam-hardening artefact correction because beam hardening occurs in each X-ray projection. Conventional beam-hardening correction techniques are not always accurate. Even with iterative beam-hardening correction methods, residual artefacts may still exist after correction when exact knowledge of the physical model (spectrum, detector, imaging materials) is not available. Therefore, virtual monochromatic images created in the image domain may still contain beam-hardening artefacts propagated from the low- and high-energy images, especially in the presence of dense bone or iodine (14).

DECT has proven to be a valuable tool in the suppression of metal artefacts as well based on several studies. Dual energy CT reduces beam-hardening, but not scatter and photon starvation. Thus, some dark streaks between high attenuation objects remain in a dual energy scan (24). The energy extrapolation decreases the severity and the streak intensity thereby improving the median diagnostic image quality (48). Especially the combination of DECT with specific post-processing can significantly improve the diagnostic value in imaging with metallic implants. Since metallic artefacts are a mixture of beam-hardening, streak artefacts and photon starvation, it is expected that metallic artefacts can be reduced but its effectiveness will depend on the kind of metallic composites. Since photon starvation cannot be corrected for, these effects are expected to still be present in the monochromatic keV images, also at high keV.

Using virtual monochromatic images at high keVs have demonstrated the ability to reduce artefacts caused by metal implants on dual-source, dual-energy CT, where optimal energies vary between 95 and 150 keV (12,13). Scanning at a higher kV results in a harder X-ray beam, and thus less beam hardening artefacts. In addition, metal is more “transparent” to higher energy photons, making it less likely to block all photons, thus reducing scatter artefacts. However, the downside is that there is less tissue contrast at high kV (24). Goodsitt et al. (2011) evaluated the accuracy of CT number and effective atomic number measured in virtual monochromatic images obtained with a projection-based fast kVp switching Dual-Energy technique. Their results showed CT number inaccuracies especially for dense materials at low energies and that the beam-hardening artefacts were still present, mainly at lower monochromatic energies (11). Their evaluation demonstrates that the synthesized virtual monochromatic images generated from the current fast kVp switching dual-energy technique are not truly monochromatic, even though they are processed in the projection domain. Further research is required to fully realize the theoretical benefit of the projection-based method. Currently, it remains unclear which implementation has an advantage over the other regarding beam-hardening artefact reduction and quantitative CT number accuracy.

4 Study design: Research questions and objectives

In order to quantify the additional value of O-MAR, IMR and Spectral CT, this research is divided into 5 separate parts. Each part has its own aims and research questions.

1 - Part 1 will focus on the quantitative additional value of O-MAR, IMR and the combination of both techniques relative to FBP and iDose^4 reconstructions with and without the use of O-MAR. Different kVps and mAs' will be used to determine optimal settings for the investigated techniques.
- What is the quantitative additional value on image quality parameters using IMR relative to FBP and iDose^4 reconstructions?
- Is O-MAR capable of reducing metal artefacts?
- Under which circumstances results O-MAR in the smallest deviations in mean HUs, noise and CNRs relative to reference values? Which kVp, which dose-level and which reconstruction algorithm is superior?
- Does the use of IMR in combination with O-MAR enable a reduction in radiation dose while maintaining sufficient image quality?

2 - Part 2 will focus on quantitative differences in mean HUs, noise and CNRs on the iCT and IQon CT-scanners in conventional polychromatic imaging. Analyses will be performed with and without the influence of metal artefacts.
- What are the actual differences in image quality parameters between both CT-scanners when focussing on unaffected pellets and on the by metal artefact most affected pellets?

3 - Part 3 will focus on the effects of monochromatic CT-imaging. 120 and 140-kVp results at conventional dose at Isala for different prosthetic configurations will be analysed focusing on mean HUs, noise and CNRs.
- What is the effect of monochromatic imaging without metal artefacts on mean HU, noise and CNR?
- What is the effect of monochromatic imaging on mean HU, noise and CNR when inserting different prosthetic alloys?
- Is high monochromatic keV imaging capable of reducing metal artefacts?
- What is the optimal monochromatic energy level in the CT-imaging of metal prosthesis?

4 - In part 4 a quantitative analysis will be performed focusing on O-MAR and monochromatic Spectral CT imaging. Conventional images with and without the use of O-MAR will be compared to the corresponding 70 or 74 keV and 200 keV images to quantify the degree of MAR at various kVps and mAs'.
- Are mean HU values in monochromatic images reliable and similar to polychromatic images at similar dose levels and kVp settings?
- Are CNRs and noise levels similar for conventional polychromatic images and monochromatic kVp equivalent keV images?
- How well is the beam-hardening artefact and streak-artefact corrected for using different metal alloys?
- Which of the two approaches is superior in MAR?

5 - In part 5, all novel CT-techniques will be taken into account. The value of individual techniques and possible combinations of techniques will be quantified based on deviations and corrections of the image quality parameters HU, noise and CNR from high to ultra-low-dose with a maximal radiation dose reduction of 80% relative to current clinical practice.

- How accurate remain CT numbers at ultra-low-dose using various CT-techniques?
- Which combination of novel CT-techniques is superior in the ultra-low-dose imaging of the most commonly used hip prosthesis?

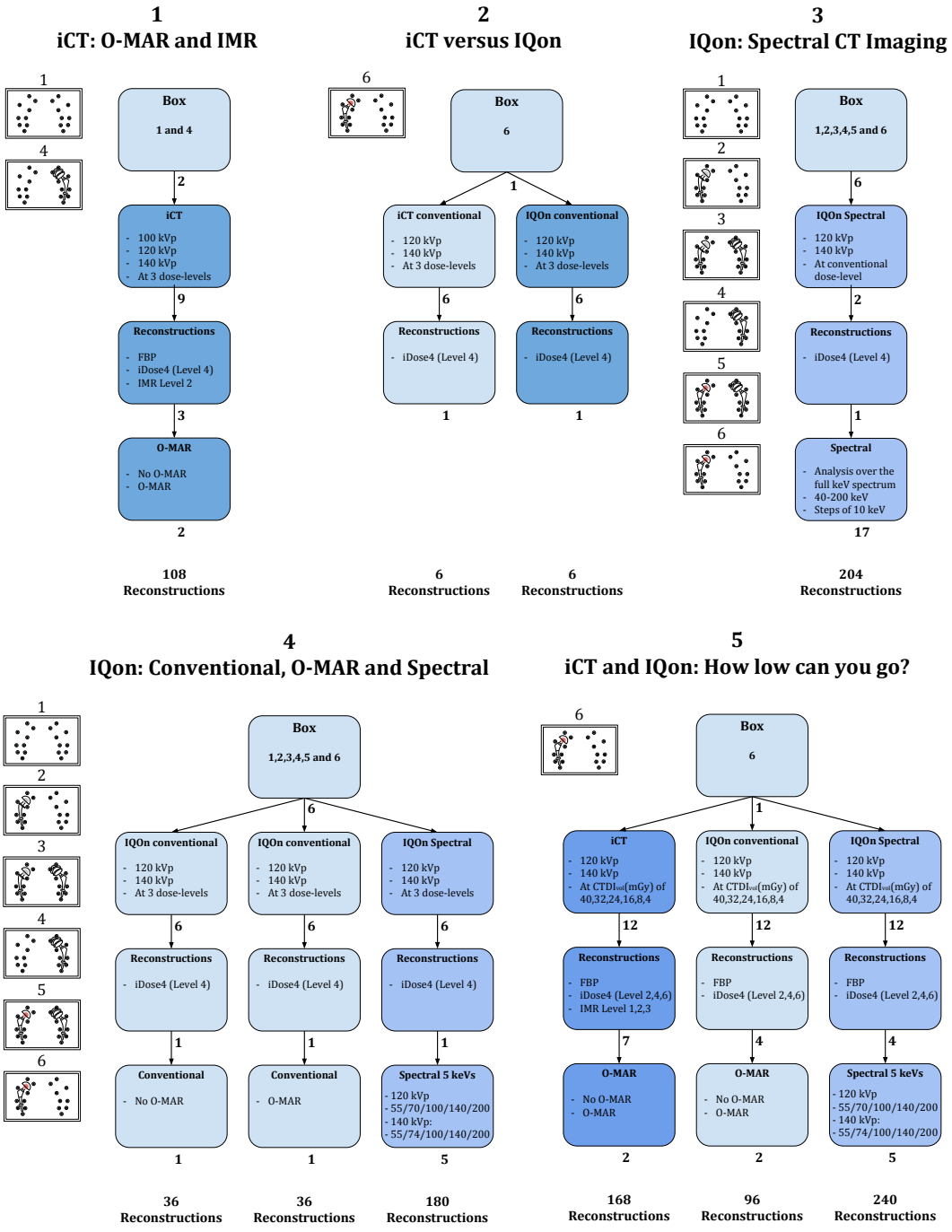

Figure 4.1: General overview of the 5 parts. Different scanners are highlighted in different shades of blue.

5 Materials and methods

5.1 Hip phantom

The base of the phantom box consists of Poly-Methyl-Meth-Acrylate (PMMA) with a length, width and height of respectively 42×29.5×13.5 cm, illustrated in Figure 5.1. PMMA is an excellent substitute for water due to a relative attenuation of 119% relative to water at relevant photon-energies (49).

In order to represent a realistic phantom, shields are placed inside the phantom to decrease the coronal diameter of 42 cm to 32 cm, which is a representative coronal diameter in patients. Detailed phantom size calculations are made based on extensive water-equivalent diameter (WED) calculations based on different body sizes executed by Menke et al. (2005). The water-equivalent diameter is the circular diameter of only water to ensure the exact same attenuation of x-rays. A BMI of 25 results in a WED of 29.15 cm (50).

To derive a correct sagittal diameter based on the WED of 29.15 cm and a coronal diameter of 32 cm, the surface area of a circle with the size of the WED is needed as a reference. The surface area of a circle with a WED of 29.15 cm is 667.37 cm^2, which results in a sagittal diameter of 20.86 cm dividing 667.37 cm^2 to the minimal coronal diameter of 32 cm. To increase the sagittal diameter from 13 cm to 20.86 cm an increase of 7.86 cm of water is needed. This results in a diameter of 6.60 cm PMMA based on its density of 1.19 g/cm^3. Six PMMA shields of 10 mm were used where three shields were placed below on top of the phantom since only 10 mm shields were available.

The phantom contains 18 cylindrical hydroxyapatite (HA) pellets representing bone with a certified calibration with a documented tolerance of ± 0.5% (2). Within a tolerance of 0.05 and 0.1 mm in the X, Y and Z-axis, the centre of the pellets is situated within one plane. On each side the 9 pellets with a height and diameter of 10 mm are fixated onto PMMA pillars to ensure correct alignment of the pellets at the middle of the phantom.

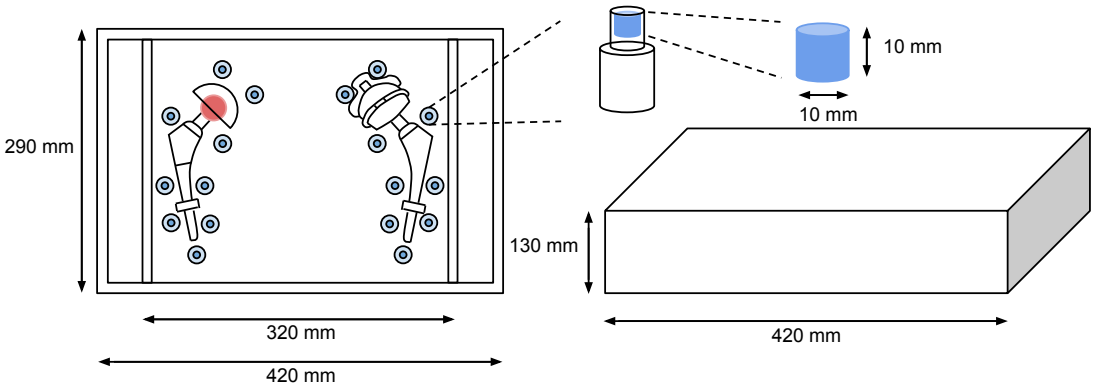

Figure 5.1: A detailed overview of the hip prostheses phantom including two different hip prostheses and 18 hydroxyapatite pellets.

5.2 Prostheses

The acquisitions are obtained with and without the insertion of three different hip prostheses with different stem, head and cup composites. Different prostheses configurations, referred as 'boxes', are investigated using unilateral and bilateral hip prostheses settings. The prostheses are fixated with custom-made PMMA moulds in order to prevent movement and provide correct alignment at the middle of the phantom. Unlike other solid phantoms, this phantom can be filled with water and several different prosthetic configurations can be inserted.

The first prosthesis consists of a cemented cobalt-chrome-molybdenum alloy stem, the Lubinus® SP II® hip prosthesis stem (Link Hamburg, Germany). Its S-shape resists rotational forces and sleeves over the length of the prosthesis are used to obtain a good fixation using cement. The head consists of the same cobalt-chrome-molybdenum alloy. The cup consists of ultra-high-molecular-weight-poly-ethylene (UHMWPE) (Link Hamburg, Germany) and is fixated in the acetabulum using bone-cement. The deep design of the cup resists luxation. The configuration of this THA is one of the two most commonly used at Isala Clinics Zwolle.

Figure 5.2: Prosthesis 1

The second hip prosthesis is a large cement-less Metal-on-Metal (MoM)-prosthesis (Biomet Warsaw, Ontario). It consists of a Titanium Aluminium Vanadium (Ti_6Al_4V) stem. The M2a-MagnumTM System is the only MoM-implant to offer a titanium insert. The cement-less ReCap-M2a-Magnum™ cup is made of a cobalt-chrome-molybdenum alloy and is covered with a porous titanium PPS® coating that encourages bone growth (51). Its large diameter provides up to 165 degrees of acetabular head coverage to help minimize the potential for edge loading and metal debris. Its a good choice for active people due to its large diameter with its large degree of motion decreases dislocation, enhances cup fixation and long-term performance (52).

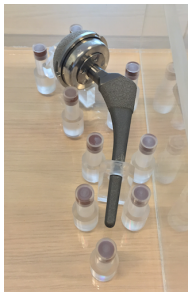

Figure 5.3: Prosthesis 2

The third prosthesis contains the most commonly THA prosthesis configuration currently used at Isala Clinics Zwolle. The stem consists of the similar Titanium Aluminium Vanadium (Ti_6Al_4V) stem (Biomet Warsaw, Ontario) used in middle prosthesis composition. The head of the prosthesis consists of a zirconia toughened alumina ceramic (ZTA) (Biolox® delta, ceramtec Germany). The composition includes SrO, Y_2O_3 and Cr_2O_3 (53). The same cemented ultra-high-molecular-weight-poly-ethylene (UHMWPE) cup (Link Hamburg, Germany) cup as for the left prosthesis composition.

Figure 5.4: Prosthesis 3

Since we want to determine the effect of different prostheses and the use of unilateral and bilateral prostheses we composed six prosthesis compositions. The phantom without the insertion of a prosthesis is used as a references and is referred as Box 1. The first prosthesis in Figure 5.2 is referred as Box 2. A combination of the first and second prostheses is referred as Box 3, where Box 4 contains only the second MoM-prosthesis. Box 5 consists of the second and third prosthesis. Finally, Box 6 contains the most commonly used prosthesis illustrated in Figure 5.4. The entire overview of all box configurations is illustrated further on.

By investigating different metallic composites, influence of various metals on the degree of artefacts can be determined. It is expected that different metallic composites, with different atomic number and atomic weight will interfere with X-rays differently therefore influencing image quality differently. Heavier metals will cause higher attenuation of X-rays resulting in more severe artefacts. Subsequently it is expected that bilateral hip prostheses will cause heavier artefacts relative to unilateral hip prostheses. The distance between the pellets and the prostheses and amount of metal / diameter of the prostheses in the coronal plane is also expected to have an effect on the amount of artefacts. Figure 5.5 provides an overview of the 6 different box configurations.

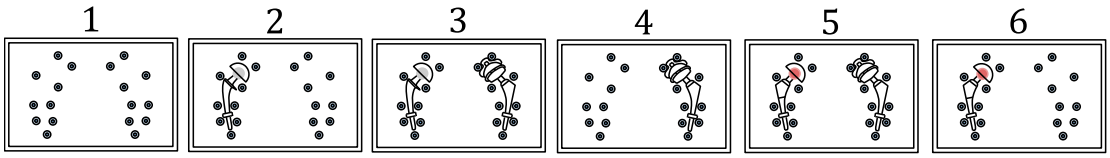

Figure 5.5: All 6 box configurations including three different prostheses.

5.3 Quantitative analyses

We quantify the value of the novel CT-techniques by analysing the pixel intensities in Hounsfield Units (HU), noise levels and contrast-to-noise-ratios (CNRs) within several ROIs. The degree of metal artefacts and the effectiveness in metal artefact reduction will therefore be determined based on analyses on these three image quality parameters.

5.3.1 Hounsfield Units

In CT imaging differences in attenuation are translated to various displayed grey levels or grey shades based on the Hounsfield Unit (HU) scale. The HU scale is a linear transformation of the linear attenuation coefficient measurement into one in which the radiodensity of distilled water (at standard pressure and temperature) is defined as zero HU, while the radiodensity of air at standard pressure (STP) is defined as - 1000 HU (54).

For an object μ, with a linear attenuation coefficient μ_{obj}, the HU value given by Equation 5.1 and 5.2 with μ_{H2O} as the linear attenuation of water. The scale is offset such that water has a HU of 0, therefore giving vacuum a HU of -1000.

$$HU = 1000 \left[\frac{(\mu_{obj} - \mu_{H2O})}{\mu_{H2O}}\right] \tag{5.1}$$

$$HU = 1000 \left(\frac{\mu_{obj}}{\mu_{H2O}}\right) - 1000 \tag{5.2}$$

By adjusting window width and window level, the range of displayed HU can be adjusted. A standard bone window for example consists of a window level of the central HU value of 800 and a overlapping window width of 2000 resulting in a visualization of grey shades between -200 and + 1800. Other values will be displayed black or white.

5.3.2 Noise

Image noise is a measure of statistical fluctuations in the image. Especially because an x-ray tube will not emit the same number of x-rays over a given time period, but rather the number of x-rays will fluctuate around a mean value according to a Poisson distribution.

After attenuation through the patient and detection at the detector the measured data will contain noise, which influences the reconstruction. Noise is measured by calculation the standard deviation of pixels in a region of interest (ROI) of a uniform section. Regarding image noise analyses, we only focus on this standard deviation of pixel values (HU).

5.3.3 SNR and CNR

Signal difference between small target region HU_t and its surrounding background region HU_b is referred as the relative contrast C_r. The CNR is the product of C_r and the signal to noise ratio SNR determined using the noise in the background region of the reconstructed CT image (55). In this study CNR and SNR values are measured by obtaining background and target regions locally for each of the 18 pellets individually.

$$CNR = \frac{HU_t - HU_b}{HU_b} \times \frac{HU_b}{\sigma_{HU_b}} = C_r SNR \quad (5.3)$$

so:

$$SNR = \frac{HU_b}{\sigma_{HU_b}} \; and \; C_r = \frac{HU_t - HU_b}{HU_b} \quad (5.4)$$

In general, the most important image quality parameter is the contrast-to-noise ratio since absolute HU values, contrast between the object and background and noise are taken into account and is determined by the following formula for all individual pellets:

$$CNR_{pellet} = \frac{\mathrm{HU_{pellet}} - \mathrm{HU_{Background\ of\ the\ pellet}}}{\sigma_{\mathrm{Background\ of\ the\ pellet}}} \quad (5.5)$$

5.4 Measurement template

The quantitative analysis is executed using ImageJ version 2.64 and Matlab 2014b. A template is developed and used for each scan in order to enhance the reliability of the measurements. Axial reconstructions were loaded in a Philips Portal Workstation to obtain coronal slices. The coronal slice aligned at the middle of the pellets is stored as a DICOM-file for each of the 108 datasets. A single coronal slice at the minimal slice width of 0.64mm was loaded into Image J where an optimal template of 36 ROIs in total was manually created. This ImageJ ROI template was subsequently loaded into Matlab where a script was developed to create the actual ROIs where the positions of the manually determined ROIs where used to create the final template. This final template consists of 18 ROIs placed in the centre of all hydroxyapatite pellets and 18 ROIs surrounding all pellet ROIs in order to obtain local contrast-to-noise-ratios.

In total two measurement templates are designed, one for FBP and iDose^4 reconstructions and one for IMR reconstructions since this algorithm did not take the table position into account. The size of the pellet ROI is chosen in such a way that the amount of pixels is sufficient enough to obtain a reliable statistical analysis but also small enough to avoid the partial volume effect. The amount of pixels of the CNR ROIs is adapted to the amount of pixels of the pellet ROIs, 168 pixels per ROI. The template is shown in Figure 5.6.

The pellet ROIs have a diameter of 14.7 pixels in diameter. This corresponds to an actual diameter of 6.6mm. Using a diameter of only 6.6 mm of the 10mm is accepted as a safe margin to avoid the partial volume effect since the resolution of CT is approximately 0.45 mm. Average HU values are calculated by measuring the mean pixel intensities within the local ROIs. Noise is calculated by determining the standard deviation of HU values within the local ROIs. Local CNRs are calculated by subtracting the average HU value of the local background ROI (ROI 2) from the average HU value of the pellet and subsequently dividing this by the noise of the local background ROI. An overview of all 18 pellets is given in Figure 5.6, with 9 left pellets (L0-L8) and 9 right pellets (R0-R8).

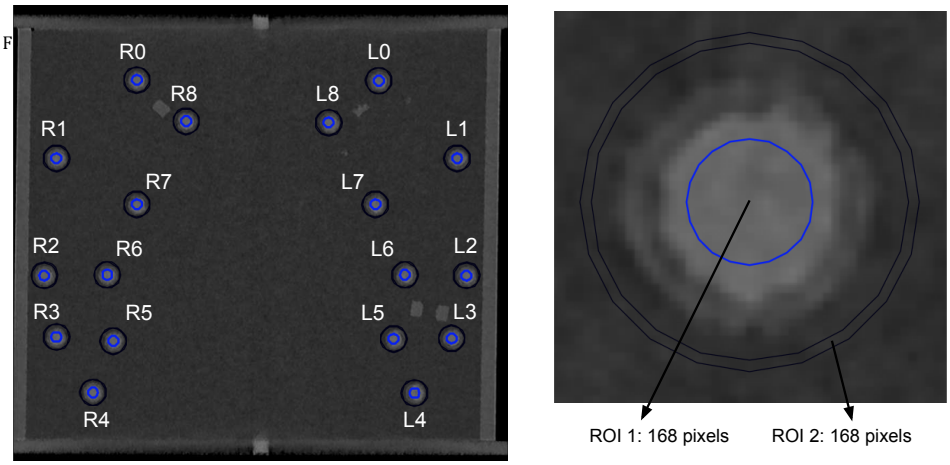

Figure 5.6: ROIs of the 18 pellets. Each pellet has 2 ROIs, the first ROI is located in the centre of the HA pellet and the second pellet is located around the pellets. The amount of pixels is equal for both ROIs.

The coronal slice located in the exact middle of the HA pellets is selected for each reconstruction by manually adjusting the slice position. When loading a dataset into the portal, a similar coronal slice is selected for each different dataset automatically. Manually, the exact location of 197.22 µm is selected and stored as a DICOM-file and was given a specific name. Measurements are performed by loading the relevant coronal slice into Matlab and run a script which was specially developed to enhance the workload and accuracy of this research.

5.5 Data acquisition

The phantom was scanned on a Philips Brilliance iCT 256-slice CT scanner and the IQon Spectral CT scanner stalled in respectively Zwolle and Haifa. All scans were acquired with 64 x 0.625 collimation since this is the maximal Z coverage that can be reached for the IQon. Other static acquisition parameters were adjusted to a clinical hip protocol used in current clinical practice at Zwolle with 0.9 mm slice width, a slice increment of 0.45, pitch of 0.398 and a high resolution. Table 5.1 shows the list of static scan parameters used to compare scan results acquired on the iCT and the IQon.

Table 5.1: Static scan parameters.

Parameter	iCT	IQon
Collimation	64x0.625 mm	64x0.625 mm
Slice thickness	0.9 mm	0.9 mm
Slice increment	0.45 mm	0.45 mm
Number of slices	667	667
Pitch	0.398	0.392
Image matrix	512 x 512	512 x 512
Field of view	330 mm	330 mm
Resolution	High	High
Rotation time	1.0 sec	0.75 sec
Dose modulation	Off	Off
Dose right	Off	Off
Adaptive filter	On	On
Filter	D or Sharp Plus (IMR)	D
Enhancement	0.0	0.0
Zoom	1.0	1.0

Depending on the kind of sub-analysis within this research different acquisition parameters were varied. We used different kVp levels of 100, 120 and 140-kVp and adjusted the mAs in order to represent various $CTDI_{vol}$ dose-levels to investigate the influence of tube voltage and low-dose scanning on image quality parameters. Current optimal tube voltage in hip prosthesis imaging is 140-kVp where the average $CTDI_{vol}$ is approximately 20 mGy.

All acquisitions are obtained consecutively in order to use the same surview and measurement template to acquire the highest reliability. The phantom was filled with water and fixated on the scan table to prevent any movement at a table height of 70. Water-bubbles, present on the prostheses and pellets were removed as good as possible. Silicon foil is placed on top of the box in order to eliminate any remaining air bubbles.

To ensure a reliable and realistic comparison between the iterative reconstruction technique and the model-based iterative reconstruction technique, the noise reduction levels and filters are matched. When imaging large metallic parts using CT a hard or sharp filter is needed in order to increase the contrast between hard and soft materials. Therefore in case of iDose^4 and FBP the hard filter D was used where in case of IMR filter SharpPlus was chosen. Images were reconstructed at a minimal FOV (field-of-view) of 330 mm with an image matrix of 512×512 resulting in a coronal slice width of 0.64 mm. Analysis is performed on these thinnest slices. Using larger image matrixes of 768×768 and 1024x1024 is possible on the iCT scanner but since the largest image matrix regarding Spectral reconstructions on the IQon is 512×512, this is used in order to analyse with a similar spatial resolution.

5.6 Statistical analyses

Statistical analysis is performed using the repeated measures ANOVA, with varying 'between subjects' and 'within subjects' factors since the data is dependent and not normally distributed. The amount of between and within subject factors with corresponding levels depends on the relevant analyses. Since the pellets are repeatedly scanned with different acquisitions parameters, using different prosthesis, different reconstruction techniques at different scanners, this repeated measures approach is advised (56). The 18 different pellets can be seen as subjects. The 6 different box configuration can be seen as a between subjects factor, where type of scan, reconstruction technique or scanner can be seen as a within subjects factor. In each performed statistical test, the between and within factors will be mentioned with corresponding levels. The Eta Squared value refers as an effect sizes and will be taken into account as a measure of the found effect.

Since this repeated measures ANOVA requires a certain amount of subjects, individual pellet analysis cannot be performed using this test. In case of individual pellet analyses, a quantitative descriptive analysis will be performed.

CT-imaging of a hip prosthesis using model-based iterative reconstruction and its influence on metal artefact reduction: a quantitative analysis.

Purpose: To quantify the effect of MBIR combined with orthopaedic metal artefact reduction (O-MAR) in the suppression of metal artefacts using a large Metal-on-Metal prosthesis at different kVp settings and dose levels.

Methods and Materials: A water-filled phantom was used made of PMMA containing a metal-on-metal prosthesis surrounded by 18 hydroxyapatite pellets representing bone. Scans were acquired on the Philips 256-slice iCT scanner using low, normal and high dose (CTDI: 10, 20 and 30 mGy) at 100, 120 and 140-kVp. Images were reconstructed with Filtered Back Projection (FBP), iterative reconstruction (IR, iDose^4 level 4) and MBIR (IMR level 2), with and without the use of O-MAR. Mean Hounsfield Unit, noise [HU] and CNR of all pellets with and without the insertion of a prosthesis were calculated and analysed using a standardized measurement template.

Results: At identical dose-levels, mean CNR of 6.41, 10.09, 25.82 ($p<0.001$) and noise levels [HU] of 50.00, 29.87, and 10.66 ($p<0.001$) were obtained for FBP, IR and MBIR respectively at $CTDI_{vol}$ of receptively 10, 20 and 30 mGy. Even at half-dose CNR is higher and noise is lower with MBIR when compared with FBP and IR at normal and high dose in a clinical setting. For severe metal artefacts O-MAR works best. O-MAR in combination with MBIR, IR and FBP results in an artefact reduction of respectively 63%, 60% and 50% ($p<0.005$).

Conclusions: MBIR combined with O-MAR significantly improves CNR and reduces noise and metal artefacts in the CT- imaging of MoM-prosthesis. O-MAR is most effective at 140-kVp and when combined with MBIR resulting in the greatest HU, noise and CNR corrections towards baseline values. Image quality with MBIR is superior compared to FBP and iDose^4 at all dose levels. MBIR in combination O-MAR allows for significant dose reduction of at least 50% while maintaining sufficient image quality.

6 Results of Part 1: IMR and O-MAR on the iCT

The first part of this graduation research is based on a previous study executed by Boomsma et al. (2015). The performance of the orthopaedic metal artefact reduction algorithm O-MAR is investigated in combination with the iterative reconstruction algorithm iDose^4. The tube voltage, tube current, filter type and different iDose^4 levels were varied. Since the recently introduced reconstruction algorithm IMR is currently available, the additional value of this new algorithm needs to be investigated. Besides expected benefits of IMR only, its capabilities and value when combined with O-MAR is still unknown.

The additional value of model-based iterative reconstruction with and without the use of O-MAR is determined by a quantitative analysis based on a phantom study. Scans were acquired with and without the insertion of a unilateral Metal-on-Metal prosthesis at different kVps and dose levels. All scans were reconstructed with FBP, iDose^4 and IMR with and without O-MAR and analysed with the same measurement template where the phantom without the insertion of a prosthesis served as a reference. Level 4 of iDose^4 and level 2 of IMR are chosen in order to select the middle level of noise suppression for each reconstruction algorithm. Other levels of iDose^4 and IMR are varied in other parts within this research.

In total, nine different acquisition parameters were varied where we used three different kVp levels of 100, 120 and 140-kVp where we choose three different mAs in order to represent $CTDI_{vol}$ dose-levels of 10, 20 and 30 mGy (low-dose, standard-dose and high-dose) summarized in Table 6.1. A $CTDI_{vol}$ of for example 10, 20 and 30 mGy result in effective dose levels of 5.36, 10.72 and 16.08 mSv based on DLPs of 357.3, 714.5 and 1071.9 and a dose conversion factor k of 0.015 for the pelvis.

Table 6.1: Acquisition parameters.

kVp	mAs ($CTDI_{vol}$ 10 mGy)	mAs ($CTDI_{vol}$ 20 mGy)	mAs ($CTDI_{vol}$ 30 mGy)
100	240	480	720
120	144	288	432
140	97	195	292

Box 1 and Box 4 were scanned consecutively varying the nine different acquisition parameters resulting in 18 scans. These 18 scans were all reconstructed with FBP, iDose^4 level 4 and IMR level 2 with and without the use of O-MAR resulting in 108 different reconstructed datasets.

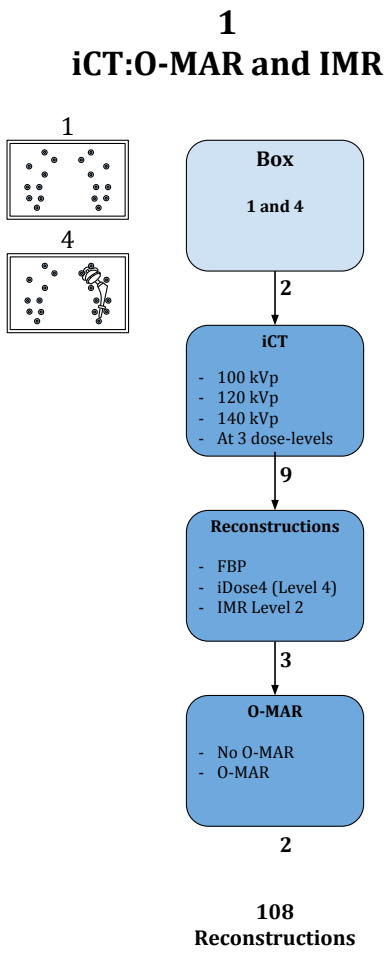

Figure 6.1: Overview of part 1.

Figure 6.2 a, b and c show the middle coronal slice reconstructed with respectively FBP, iDose^4 and IMR. Differences can be observed visually regarding standard image noise where FBP results in very noisy images, especially close to the head of the prosthesis. Images a, b and c shown in Figure 6.2 are acquired at the proposed highest kVp in case of prosthetic imaging of 140-kVp at the conventional $CTDI_{vol}$ of 20 mGy. Figures 6.2 d, e and f illustrate the additional effect of O-MAR.

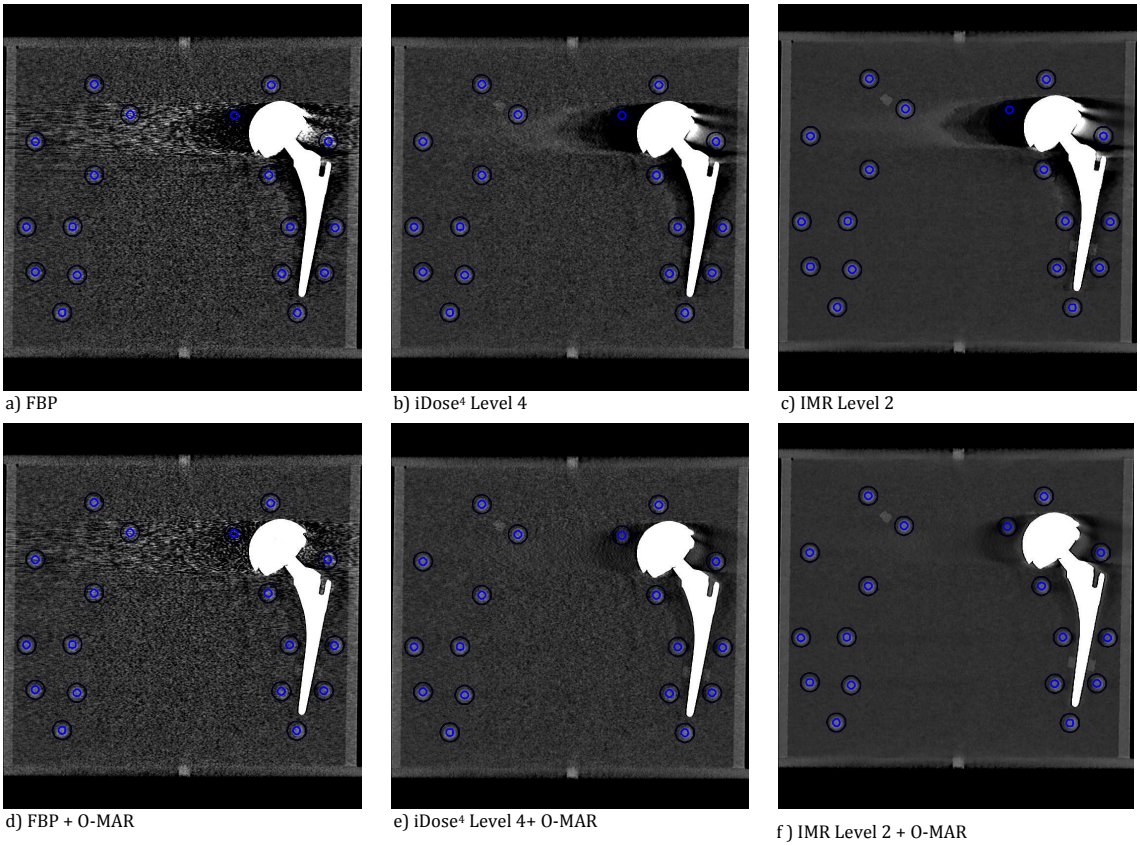

a) FBP | b) iDose^4 Level 4 | c) IMR Level 2

d) FBP + O-MAR | e) iDose^4 Level 4+ O-MAR | f) IMR Level 2 + O-MAR

Figure 6.2: Images reconstructed with FBP a & d, iDose^4 b & e and IMR c & f with and without O-MAR. Subjective image quality is visually substantially better for O-MAR images because of less metal artefacts. IMR reconstructions result in visually clearly superior image quality parameters with less noise relative to FBP and iDose^4 reconstructions.

6.1.1 Relevant pellets

All pellets on the right, R0-R8 surrounding no prosthesis, seem to be little or not affected by the large MoM-prosthesis located on the left side. The most affected pellet is obviously pellet L8 close to the head of the large MoM-prosthesis. Pellet L0, R0, L4 and R4 are not affected by metallic artefacts since these pellets are located outside the scan field of the prosthesis. HU and CNR values remain exactly the same without prostheses, with prostheses and thus also with the use of O-MAR for these pellets. This confirms the claim that O-MAR does not operate in areas unaffected by metallic artefacts.

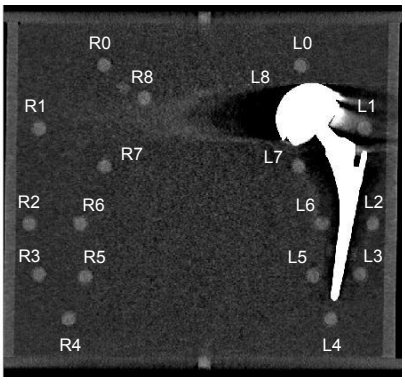

Figure 6.3: All 18 pellet ROIs.

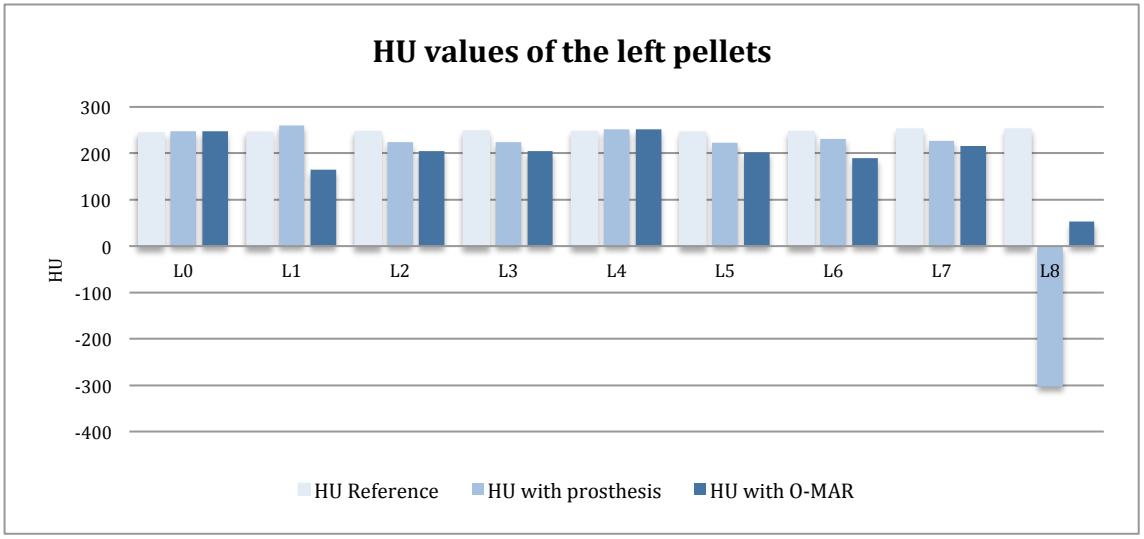

Figure 6.4: HU deviation of all left pellets at 140-kVp CTDI 20. It can clearly be observed that the greatest HU deviation is presented in case of pellet L8, which is directly located to the large head of the MoM-prosthesis.

6.1.2 Hounsfield Units

The average HU values of other pellets are also deviated where HU and CNR values decrease. Figure 6.4 illustrated the HU deviation of the left pellets when inserting the MoM-prosthesis, the corrections made by O-MAR and the reference HU value without the insertion of a prosthesis. As can be seen in Figure 6.4, the effect of metal is most severe for pellet L8 where when averaging for all nine acquisitions an average HU drop of 628 is reached. O-MAR is capable of correcting this distortion to an average HU value of 16.

Figure 6.5 shows the head of the prostheses with the 4 surrounding pellets L0, L1, L7 and L8. Figures 6.5 a, b and c are the reconstructed images obtained with respectively FBP, iDose^4 and IMR. Figures 6.5 d, e and f are reconstructed with O-MAR combined with FBP, iDose^4 and IMR. Pellet L8 is highly influenced by the metal artefacts due to the large metal head and cannot be visualized without O-MAR for all three kinds of reconstruction techniques. O-MAR combined with FBP is not sufficiently capable of reducing the most severe metal artefact as can be seen in Figure 6.5 d. O-MAR is able to suppress the artefact and visualize pellet L8 when combined with iDose^4 and IMR as can be seen in Figure 6.5 e and 6.5 f.

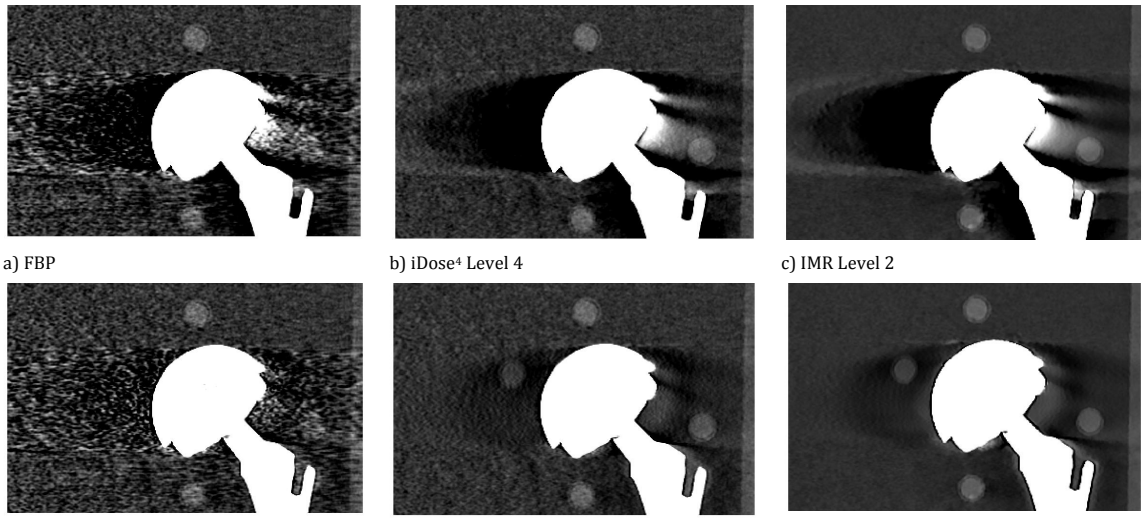

a) FBP b) iDose⁴ Level 4 c) IMR Level 2

d) FBP + O-MAR e) iDose⁴ Level 4 + O-MAR f) IMR Level 2 + O-MAR

Figure 6.5: Pellet L0, L1, L7 and L8 surrounding the head of the prosthesis. Pellet L8 is totally invisible without the use of O-MAR as can be observed in images a, b and c. Using O-MAR, pellet L8 can be visualized only when combined with iDose⁴ and IMR.

Pellet L8 is the only pellet where O-MAR consistently improves HU values towards the baseline due to the heavily decreased average HU value caused by metallic artefacts. We observed that baseline HU of FBP, iDose⁴ and IMR result were respectively 291, 290 and 272 when averaging for all 18 pellets without the insertion of a prosthesis. HU baseline values are significantly lower for IMR relative to FBP and iDose⁴ baseline values ($p<0.001$). When taking these differences into account, O-MAR results in corrections of 50 %, 60% and 63% towards baseline HU in case of the most severe artefacts in L8 for respectively FBP, iDose⁴ and IMR.

6.1.3 Contrast-noise-ratios

Model-based iterative reconstruction improves the contrast-to-noise-ratio (CNR) relative to standard reconstruction and iterative reconstruction. Without insertion of a prosthesis, the average CNR of all 18 pellets for MBIR, IR and FBP are respectively 25.82 ± 2.12, 10.09 ± 1.98 and 6.41 ± 1.76, averaged for all 3 kVp settings and dose-levels. These results are statistically significant ($p<0.001$, with a partial Eta Squared of 0.642 for the within subject factor kVp and $CTDI_{vol}$ setting with 9 levels and 0.997 for the within subject factor reconstruction technique with 3 levels). The CNRs at different kVp and reconstruction techniques improve proportionally with respect to radiation dose.

As expected, noise significantly reduces from low- to high-dose. Noise levels, measured by calculating the standard deviation of pixel intensities within the ROIs, are lower for higher kVps at similar dose-levels. Average noise levels for all 18 ROIs for the 3 kVps and dose-levels are 50.00 ± 14.70, 29.87 ± 6.26 and 10.66 ± 1.40 for respectively standard reconstruction, iterative reconstruction and model-based iterative reconstruction. These results are statistically significant ($p<0.001$, with a partial Eta Squared of 0.818 for the within subject factor kVp and $CTDI_{vol}$ setting with 9 levels and 0.985 for the within subject factor reconstruction technique with 3 levels). Noise tends to decrease at static dose-levels when increasing the kVp. Since the CNR is inversely proportional to noise the also decreasing trend of CNRs at static dose-levels when increasing the kVp, this should be caused by the larger drop in HU values relative to CNR and noise changes.

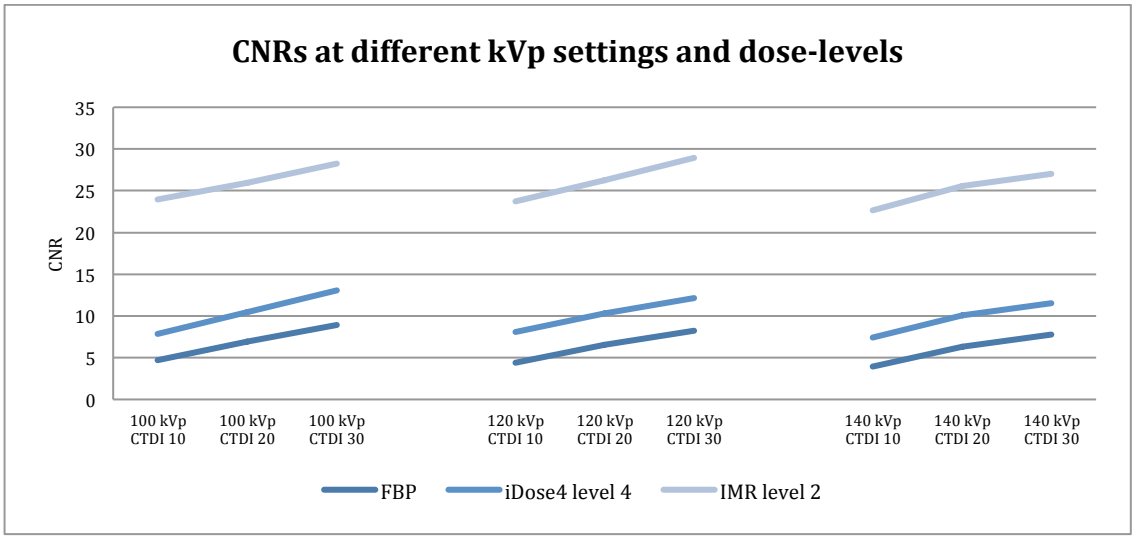

Figure 6.6: Average CNR of all pellets without the insertion of a prosthesis at 100, 120 and 140-kVp using three different dose-levels. CNRs are significantly higher for IMR relative to FBP and iDose⁴ reconstructions. CNRs are higher at high dose for all kVps.

The absolute HU correction is obviously largest for L8 with O-MAR, where HU values of other pellets remain relatively unaffected. Despite the fact that O-MAR does not improve the HU value to the baseline level without prosthesis, CNR values are significantly increased for L8 but also in case of other pellets.

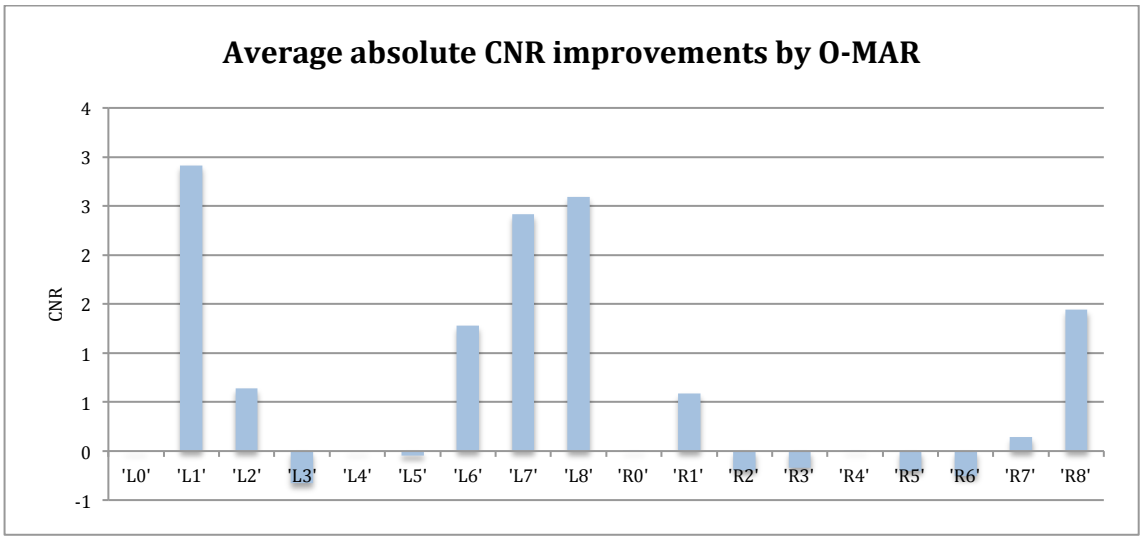

Figure 6.7: Absolute CNR improvements by O-MAR when averaging for all kVps, dose-levels and reconstruction techniques.

Figure 6.7 shows the CNR improvement of pellet L8 by O-MAR for FBP, iDose⁴ and IMR at 140-kVp. CNR values are low (mostly below 1.00) therefore making the distinction between the pellet and the surrounding water almost impossible, as illustrated in Figure 6.5 (a-c). O-MAR results in a CNR improvement in all cases thereby revealing the position of the pellet L8, especially when focussing on iDose⁴ and IMR. O-MAR improves the CNR values of L8 with absolute values of 0.72, 2.28 and 4.78 for respectively FBP, iDose⁴ and IMR.

As can be seen in Figure 6.8, CNR values of L8 without the insertion of a prosthesis show great differences for FBP, iDose^4 and IMR. The large MoM-prosthesis heavily decreases CNRs values for all reconstruction techniques. O-MAR is able to perform the greatest absolute CNR improvement combined with MBIR but returning to baseline CNR values is not possible.

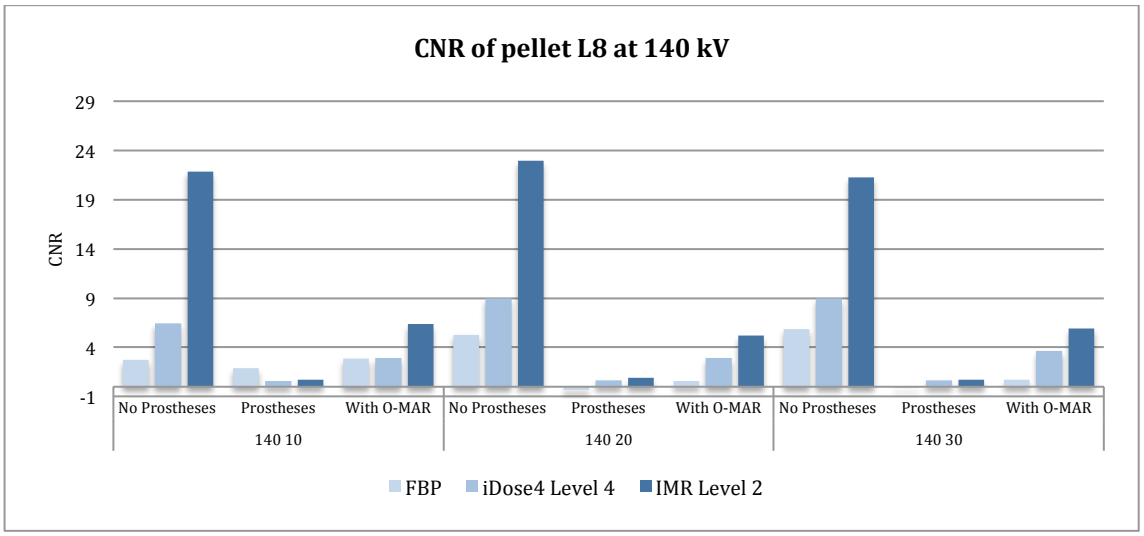

Figure 6.8: CNR values of pellet L8 are illustrated at 140-kVp and different dose-levels. CNRs without the insertion of a prosthesis are high. CNRs decrease substantially for FBP, iDose^4 and IMR with the insertion of a prosthesis. CNRs are increased with the use of O-MAR are illustrated but do not reach reference values.

$CTDI_{vol}$ of 10, 20 and 30 are referred as respectively 'half-dose', 'normal-dose' and 'high-dose'. Figure 6.9 (a-c) show the reconstructed images with high-dose FBP and high-dose iDose^4 versus half-dose IMR with O-MAR. Average noise level and CNR values are significantly higher at a $CDTI_{vol}$ of 10 mGy for IMR relative to $CTDI_{vol}$ of 30 mGy for FBP and iDose^4. With O-MAR, HU values with half dose IMR (42) are higher relative to high-dose FBP (-72) and similar to high-dose iDose^4 (48), especially when taking noise values into account. CNR values with and without O-MAR are significantly higher for half-dose IMR relative to high-dose FBP and iDose^4.

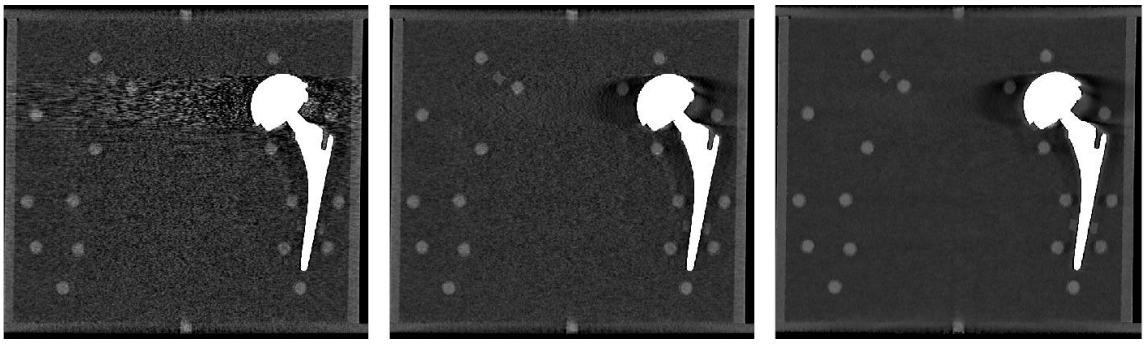

a) b) c)

Figure 6.9: O-MAR images with high-dose FBP (a) and iDose^4(b) versus half-dose IMR(c). In can be observed that the image quality parameters are better for IMR reconstructions at a third of the dose relative to FBP and iDose^4 reconstructions.

When focussing on the CNR of pellet L8, CNR using IMR is substantially higher at a third of the dose relative to FBP and iDose^4 reconstructions. Average CNR of pellet L8 are 6.34, 3.63 and 0.69 for respectively IMR at a $CTDI_{vol}$ of 10, iDose^4 at a $CTDI_{vol}$ of 30 and FBP at a $CTDI_{vol}$ of 30.

6.2 Discussion

Model-based iterative reconstruction (IMR) significantly improves image quality relative to the standard (FBP) and iterative reconstruction technique (iDose^4) at all dose levels and tube voltages. The average noise of all ROIs is lower and CNRs are significantly higher for MBIR, ($p<0.001$). O-MAR is capable of suppressing the most severe metal artefacts regarding mean HU deviations by 50%, 60% and 63% with respectively FBP, iDose^4 and IMR, where O-MAR is most effective when combined with IMR. To our knowledge this is the first and only study that obtained the additional quantitative value of a MAR technique combined with MBIR.

IR improves IQ by reducing image noise and artefacts that result from common irregularities like photon-starvation and beam-hardening (57). MBIR does not involve blending with FBP like the hybrid reconstruction technique iDose^4, which results in significantly better image quality. When averaging for kVps and dose levels, noise levels are 50.00, 29.87 and 10.66 for respectively FBP, iDose^4 and IMR. Average CNR values are 6.41, 10.09 and 25.82 for respectively FBP, iDose^4 and IMR. When observing differences between reconstruction techniques, the evaluated IQ parameters are significantly better with IMR in all cases ($p<0.001$). Average HU values without the insertion of a prosthesis are 291, 290 and 272 for respectively FBP, iDose^4 and IMR and were used as reference HU values. Values are significantly lower for IMR relative to FBP and iDose^4 where average HU values of FBP and iDose^4 are not significantly different. An explanation for the differences in mean HUs can be a different reconstruction system and a different filter type where filter D is used for FBP and iDose^4 and SharpPlus is used for IMR. Both filters enhance edges, but in case of small objects such as pellets it can affect average HU measurements. This effect will be different for both filters due to different levels of edge enhancement.

O-MAR is significantly increasing image quality when imaging a large Metal-on-Metal prosthesis by decreasing noise, improving CNRs and correcting HU towards the baseline. Measurements of the ROIs using the phantom without a prosthesis were considered as reference, as illustrated in Figures 6.2-6.4. O-MAR works best in case of severe artefacts (L8) where absolute HU corrections of 529.68 HU are reached towards its corresponding reference value. When focussing on HU corrections for other pellets besides L8 the effectiveness of O-MAR did not show a similar relation. Pellet L0 and L4 are unaffected by the prostheses in all cases due to the fact that these pellets are located in the axial scan area where no metal artefacts are present. This confirms the statement that O-MAR has no effect on structures that are not affected by metal artefacts. With regard to HU values, O-MAR tends to increase the HU deviation relative to reference values in most cases. This effect can be seen in pellets L1, L2, L3, L5, L6 and L7. In case of pellet L1, this effect can be explained by the large streak artefact, which can be seen in Figure 6.5 where O-MAR reduces the heavily increased HU value due to the streak artefact. Pellet R8 encounters some distortion due to the large head of the MoM-prosthesis.

Without O-MAR, only pellet L8 cannot be visualized which confirms the CNR values below 1.00. The average CNRs of L8 can be improved with O-MAR with standard reconstruction, iterative reconstruction and model-based iterative reconstruction with respectively 0.72, 2.28 and 4.78. Still, the absolute corrections CNRs by O-MAR are small relative to reference CNR values without the use of prosthesis. Despite the fact that reference CNR values are not reached, pellet L8 is revealed in all cases when reconstructed with iDose^4 and IMR with O-MAR. In short, for iDose^4 and IMR the quantitative CNR improvement of L8 by O-MAR large enough to ensure visibility, thereby greatly improving diagnostic possibilities.

When using O-MAR a kVp of 140 is advised. Using 140-kVp not only decreases the impact of beam-hardening but also decreases statistical noise, which should benefit the O-MAR algorithm (40). We do also see the highest effectiveness using 140-kVp relative to 100 and 120-kVp when focussing on the HU and CNR corrections towards reference values. For HU corrections, O-MAR shows an average HU correction for pellet L8 of 62% at 140-kVp, relative to 53% for 100 kVp and 58% for 120-kVp. Absolute CNR improvements of pellet L8 are 2.82, 2.77 and 2.19 for respectively 140-kVp, 120-kVp and 100-kVp. The highest absolute CNR improvement by O-MAR involved pellet L1 instead of L8. The reason for this could be the white streak appearing at the lateral side of the prosthesis crossing the ROI's of pellet L1 due to beam-hardening. This white streak contains high pixel intensities. When O-MAR corrects for metal artefacts, these white streaks disappear thereby lowering the HU value. Despite the fact that O-MAR seems to decrease the visibility of the pellet it clearly improves the appearance of pellet L1. The pellet is clearly easier distinguishable from its background.

Boomsma et al. (2015) investigated the influence and value of O-MAR based on HU deviations varying several scan-parameters (2 different kVps and 3 mAs'), filters (A and B) and reconstruction techniques (FBP and iDose^4) (2). They found that iDose^4 did not influence the effects of O-MAR but that it can result in scanning with a lower dose due to improvements in CNRs, which we can confirm based on our results. They also found that increasing iDose^4 levels did not improve the CNR in the by metal artefact heavily affected regions. Increasing the tube currents did not result in reduced metal artefacts and did thereby not in all cases increase the effectiveness of O-MAR. Increasing tube currents did show a positive effect on HU values and CNR. (2). They found that O-MAR is capable of reducing the most severe artefacts by 32% based on mean HU values, where we found a reduction of HU deviations by O-MAR of 63% using IMR and O-MAR. They also found no improvement in CNRs by O-MAR in the most affected pellets unlike our results. A possible explanation for the observed differences can be the use of a different scanner, the amount of water inside the phantom and the use of different filter type.

Several different metal artefact reduction techniques have shown to be valuable in the suppression of metal artefacts and thereby improving qualitative and quantitative image quality with improved diagnostic confidence as described earlier (6,7,9,58). These studies showed that HU are corrected towards baseline levels thereby improving subjective and objective image quality parameters (8,9). We, on the other hand, did not execute a subjective analysis but performed an extensive quantitative or objective analysis only. The use of a standardized measurement template improved the reliability and reproducibility within our study. Despite clear results for O-MAR, IMR and the combination of both techniques the use of different size, shape and density of pellets would give a clinically more relevant additional value of these techniques in other structures like soft tissue.

MBIR clearly improves spatial resolution, which at the same time greatly reduces noise. This induces a further dose reduction potential, likely more than 50% used in this part. CNR of pellet L8 at a third of the dose relative to FBP and iDose^4 with O-MAR is higher using MBIR and O-MAR for all three kVp. In our study we only used noise reduction level 2 where the use of level 3 will lead to further noise reduction. In following parts of this study we do include IMR levels 1,2 and 3 and investigate the additional value of IMR in CT imaging of metal hip prostheses at various low-dose radiation levels up to 80% dose reduction relative to current clinical practice at Isala Clinics Zwolle.

6.3 Conclusions

MBIR combined with O-MAR significantly improves CNR and reduces noise and metal artefacts in the CT-imaging of MoM-prosthesis. O-MAR is most effective at 140-kVp and when combined with MBIR resulting in the greatest HU, noise and CNR corrections towards baseline values. Image quality with MBIR is superior compared to FBP and iDose^4 at all dose levels. MBIR in combination O-MAR allows for a significant reduction in radiation dose of at least 50% relative to current clinical practice while maintaining sufficient image quality. Further dose reduction capabilities will be investigated in the final part of this graduation research.

Conventional CT-imaging of a metal hip prosthesis on the iCT and IQon CT-scanners; a comparison.

Purpose: To quantify differences in mean HUs, noise and CNRs on the iCT and IQon CT-scanners in conventional polychromatic imaging with and without the insertion of a metal hip prosthesis. We want to determine if we can observe and quantify differences between both scanners due to differences in detectors and filtration.

Methods and Materials: A water-filled phantom was used made of PMMA containing the most commonly used hip prosthesis at Isala Clinics surrounded by 18 hydroxyapatite pellets representing bone. Scans were acquired on a 256-slice iCT scanner and the IQon CT-scanner in conventional mode using three dose-levels (CTDI: 8, 24 and 40 mGy) at 120 and 140-kVp. Images were reconstructed with iterative reconstruction (IR, iDose^4 level 4). Mean Hounsfield Unit, noise [HU] and CNR of all pellets with and without the insertion of a prosthesis were calculated and analyzed using a standardized measurement template.

Results: Without the insertion of a metal hip prosthesis, mean HUs are 270 and 285 for respectively iCT and IQon images ($p<0.001$). Noise [HU] is significantly lower and CNR is higher for iCT images (29.15 versus 34.99 and 9.23 versus 8.30, $p<0.001$). When focusing on average values of the most affected pellet R6 in case of metal artefacts, mean HUs are lowest (113 versus 213), noise [HU] is higher (44.41 versus 31.93) and CNR is lower (2.99 versus 4.05) for IQon acquisitions.

Conclusions: The mage quality parameters mean HU, noise and CNR are statistically different for similar conventional iCT and IQon acquisitions. For unaffected pellets, HU values are higher, noise is higher and CNRs are lower for IQon acquisitions using 120 and 140 kVp tube currents and $CTDI_{vol}$ dose-levels of 8, 24 and 40 mGy. Conventional IQon acquisitions are more affected by metal than conventional iCT acquisitions resulting in greater HU, noise and CNR deviations relative to baseline values of unaffected pellets. These differences can be declared to differences in detector row and filtration since the beam-hardening artefact is much larger at reduced filtration resulting in more severe artefacts on the IQon.

7 Results of Part 2: Conventional iCT versus conventional IQon

In the second part of this research the actual differences in image quality parameters is investigated when using similar scans acquired on the iCT and the IQon scanner in conventional mode. Differences in image quality parameters are expected due to differences in detector row, collimation and filtration. Scans are acquired at tube voltages of 120 and 140-kVp using the most common prosthesis, regarding box configuration 6. Tube currents are adapted to static $CTDI_{vol}$ levels of 40, 24 and 8 mGy.

In order to obtain similar dose levels, tube currents set on the iCT and IQon differ as can be seen in Table 7.1. To improve the Spectral separation between the high and low energy photons in the beam, filtration is reduced on the IQon. This results in lower mAs of approximately 30% on the IQon CT scanner.

Table 7.1: Differences in tube currents between the iCT and IQon.

Tube voltage	$CTDI_{vol}$ (mGy)	Tube current iCT (mAs)	Tube current IQon (mAs)
120-kVp	40	576	444
	24	436	266
	8	115	90
140-kVp	40	390	310
	24	234	186
	8	78	61

Since we were only interested in differences in acquisitions within this part, only reconstructions were made using the 'standard' iDose^4 reconstruction algorithm at level 4. Scans are obtained using the standard acquisition parameters listed in Table 7.1.

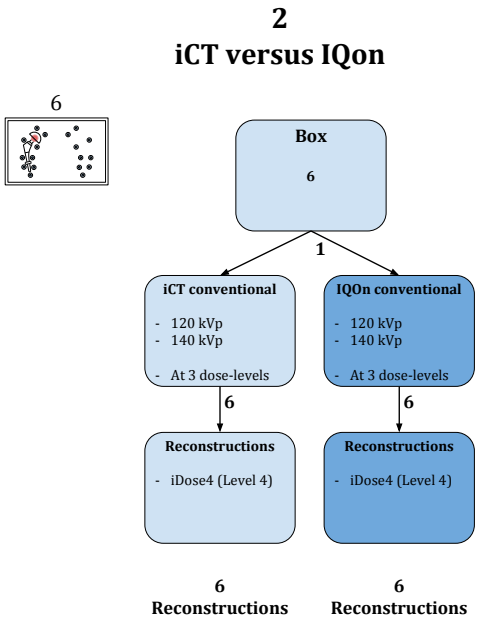

Figure 7.1: Overview of part 2.

Image quality parameters are determined on the iCT and on the IQon in conventional mode. To investigate the influence of using different CT-scanners in metallic hip prosthesis imaging, this analysis is divided into two parts. The first part focuses on differences image quality parameters without the effect of metallic artefacts. The second part focuses on image quality parameters of pellet R6, the pellet which is most affected by metallic artefacts.

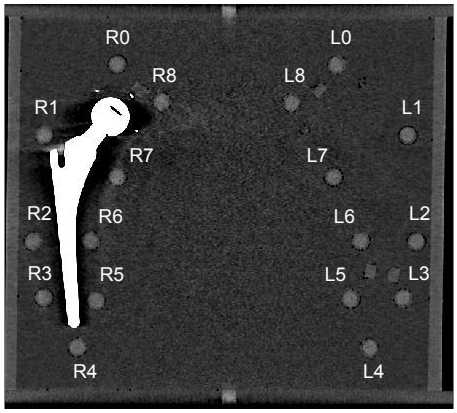

Figure 7.2: Box 6 including all 18 ROIs as in Figure 5.6.

7.1.1 Differences of IQ parameters without metal artefacts

At first, the image quality parameters of unaffected pellets are determined to investigate difference in HU, noise and CNR at similar locations in identical scans without distorting metal artefacts.

Previous investigations conducted in part 1 of this research demonstrated that pellet L0, L4, R0 and R4 are not affected by metallic artefacts due to their position in the phantom. Mean HUs, noise and CNRs are measured by taking the average values of these four unaffected pellets.

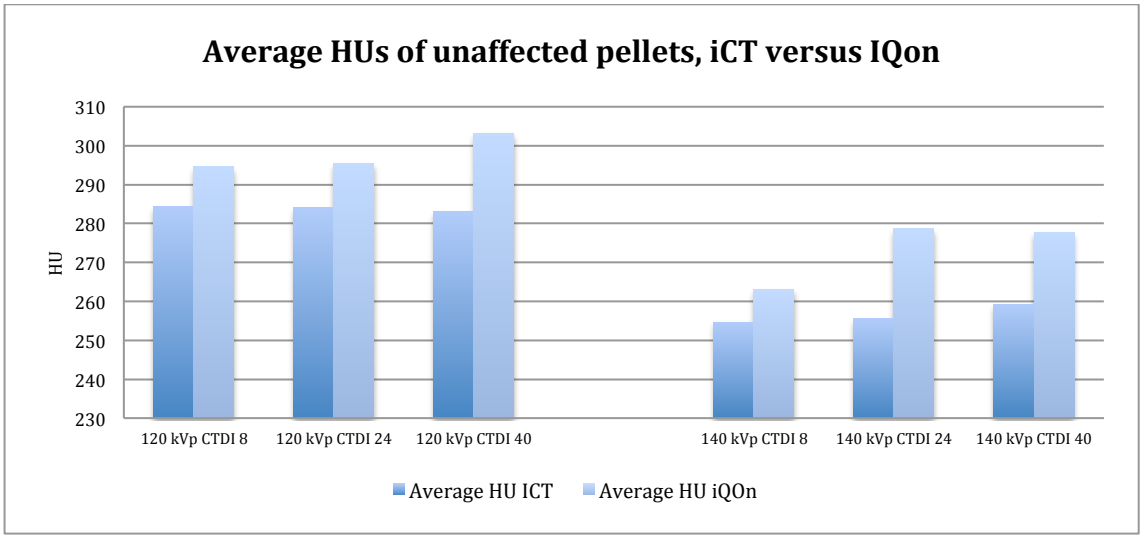

Figure 7.3: Average HU of unaffected pellets at 120 and 140-kVp at three different dose levels; iCT versus IQon. HU values are overall lower for iCT acquisitions with an average difference of 15 HU.

Average HU values of the unaffected pellets are substantially higher for the IQon. There is an average HU difference of approximately 15 HU between both scanners (270 versus 285), when averaging the 120 and 140-kVp results including three dose levels. Differences in HU of this magnitude are difficult to distinguish visually. HUs on the IQon images are higher, where the observed differences are significant ($p<0.001$, with a partial Eta Squared of 0.358 for the within subject factor kVp and $CTDI_{vol}$ setting with 6 levels).

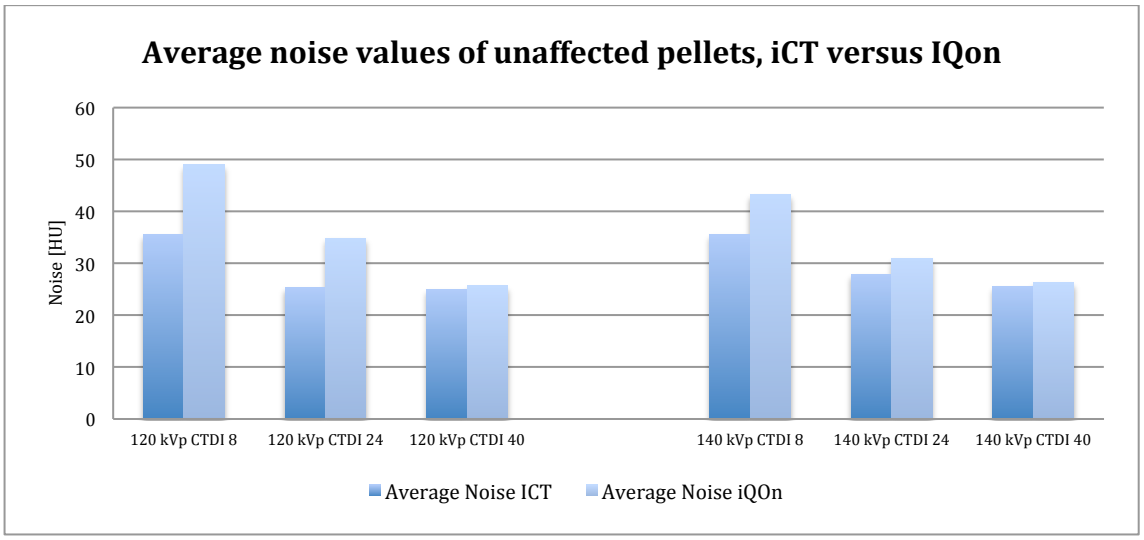

Figure 7.4: Average noise of unaffected pellets at 120 and-140 kVp at three different dose-levels; iCT versus IQon. Noise is significantly lower for iCT reconstructions at both kVp and all three dose-levels.

Noise levels are different between the iCT and IQon. Noise is higher for the IQon images where differences are more distinct at 120-kVp and for low-dose scans where iCT images contain less noise. These differences in noise are clearly visible, especially for the low-dose results at 120-kVp illustrated in Figure 7.4. Noise for iCT images is lower (29.15 versus 34.99 when averaging the six scans) where the observed differences are significant ($p<0.001$, with a partial Eta Squared of 0.948 for the within subject factor kVp and $CTDI_{vol}$ setting with 6 levels and 0.421 for the within subject factor scanners with 2 levels).

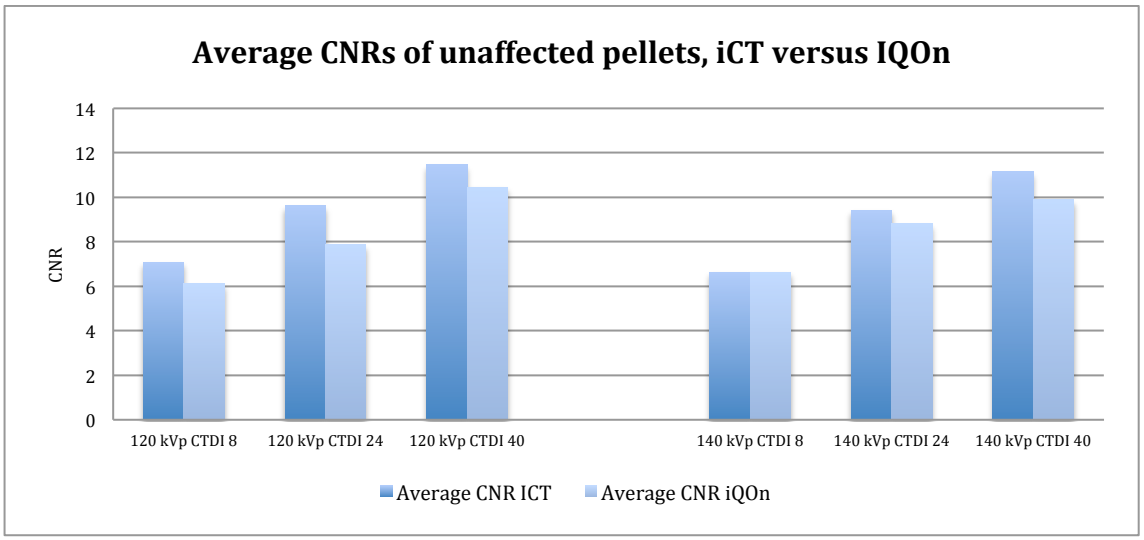

Figure 7.5: Average CNR of unaffected pellets at 120 and 140-kVp at three different dose-levels; iCT versus IQon. CNR is significantly higher for iCT images at both kVps and all three dose-levels.

Average CNR are higher for the iCT images. Despite the fact that HU values on the IQon are higher, the larger difference in noise results in an overall better CNR for iCT images. This can also be observed in Figure 7.6 where the pellets are easier to distinguish relative to the background for the shown iCT images. CNRs for iCT images are higher where the observed differences are significant ($p<0.001$, with a partial Eta Squared of 0.729 for the within subject factor kVp and $CTDI_{vol}$ setting with 6 levels and 0.264 for the within subject factor scanners with 2 levels).

Table 7.2: Overview of image quality parameters iCT versus IQon at 120 and 140-kVp and at three different dose-levels.

	HU iCT	HU IQon	Noise iCT	Noise IQon	CNR iCT	CNR IQon
120-kVp $CTDI_{vol}$ 8	284	295	35.60	49.03	7.09	6.11
120-kVp $CTDI_{vol}$ 24	284	296	25.25	34.82	9.62	7.87
120-kVp $CTDI_{vol}$ 40	283	303	25.02	25.67	11.46	10.47
140-kVp $CTDI_{vol}$ 8	255	263	35.52	43.24	6.64	6.63
140-kVp $CTDI_{vol}$ 24	255	279	27.91	30.97	9.41	8.82
140-kVp $CTDI_{vol}$ 40	259	278	25.61	26.23	11.14	9.89
Average values	270	285	29.15	34.99	9.23	8.30

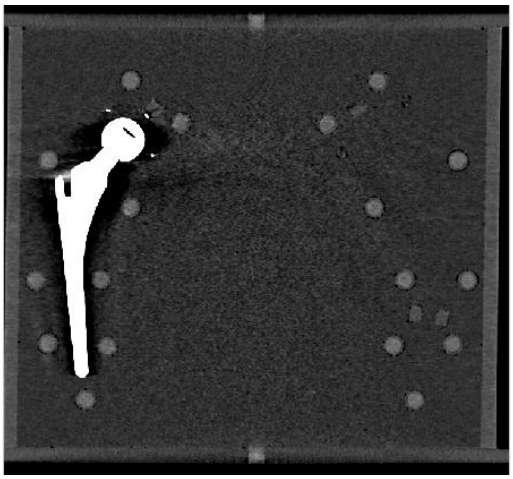

a) iCT, 120-kVp $CTDI_{vol}$ 40 mGy

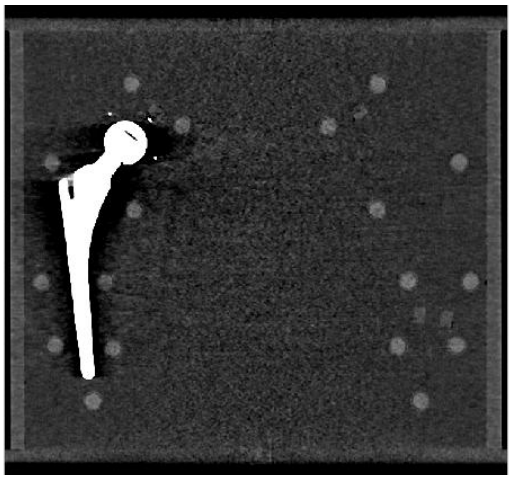

b) IQon, 120-kVp $CTDI_{vol}$ 40 mGy

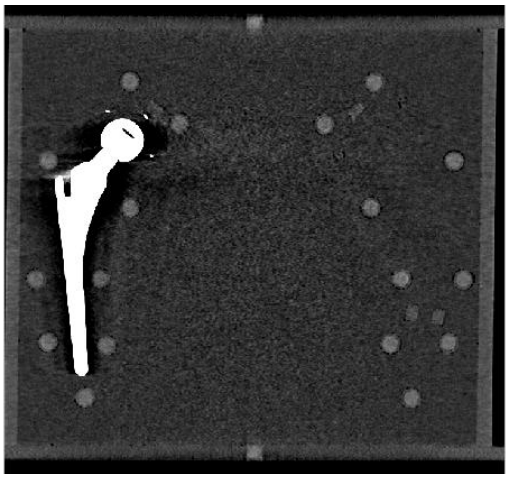

c) iCT, 120-kVp $CTDI_{vol}$24 mGy

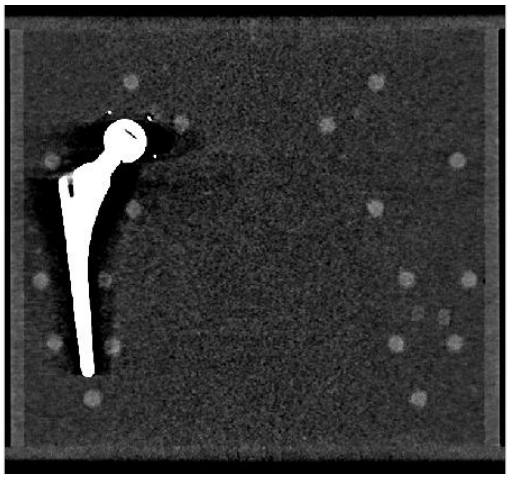

d) IQon, 120-kVp $CTDI_{vol}$ 24 mGy

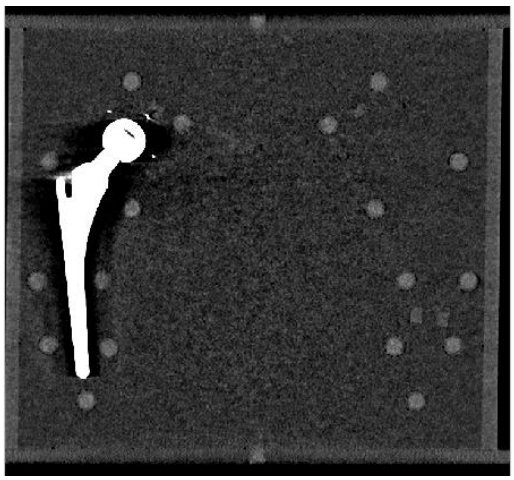

e) iCT, 120-kVp $CTDI_{vol}$ 8 mGy

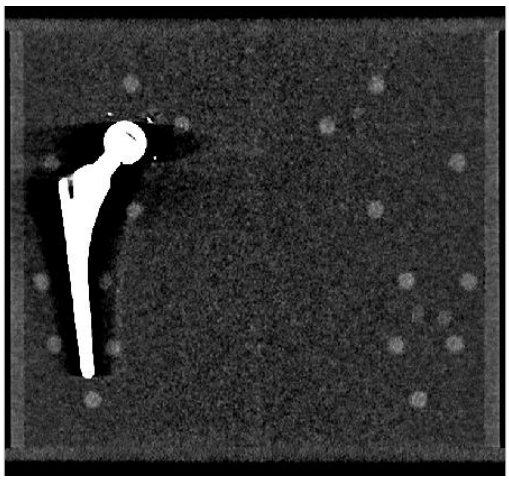

f) IQon, 120-kVp $CTDI_{vol}$ 8 mGy

Figure 7.6: iCT and IQon 120-kVp images at different dose-levels. It can be observed that metallic artefacts are more pronounced in case of IQon acquisitions since dark areas are more apparent, noise is higher and CNR is lower.

7.1.2 Affected pellets

Pellet R6 is most affected by metal artefacts since the largest HU deviation is seen at this pellet, illustrated in Figure 7.7. Although not shown, noise is highest and CNR lowest for this pellet where noise is 18% higher and CNRs are 60% lower relative to unaffected pellets. The sensitivity of both CT scanners for metal artefacts will therefore be investigated by focussing on the most affected pellet R6.

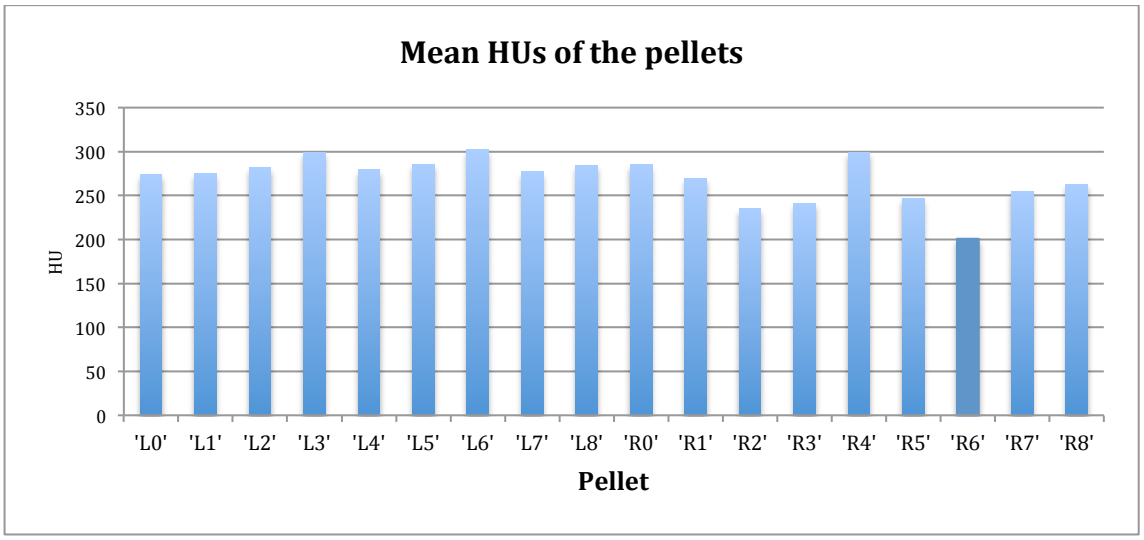

Figure 7.7: Average HU of all 18 pellets at 120-kVp low-dose acquired on the iCT scanner. Despite HU deviations are much smaller in case of this prosthesis, pellet R6 shows the greatest distortion in HU, noise and CNR.

7.1.3 Effects of metal artefacts on the iCT and IQon

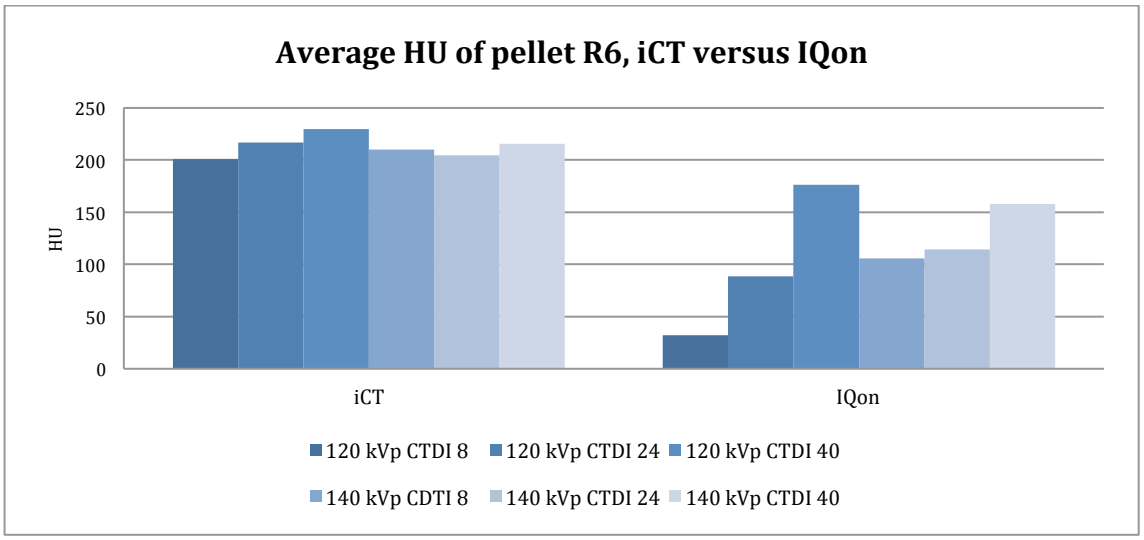

Figure 7.8: Average HU of pellet R6; iCT versus IQon. Metallic composites cause greater HU deviations in case of IQon acquisitions at both kVps and all three dose-levels.

HU distortions relative to HU reference values are greater on the IQon than iCT images. HU distortions relative to unaffected pellets are smallest at high kVp and high dose as expected based on results shown in the previous section.

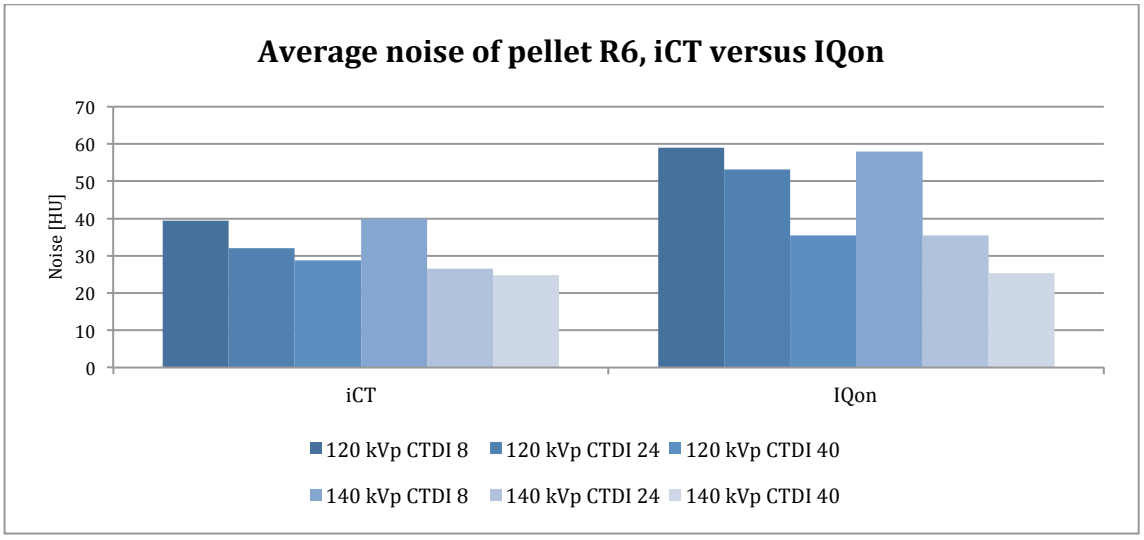

Figure 7.9: Average noise of pellet R6, iCT versus IQon. Noise of the most affected pellet is significantly lower for iCT acquisitions at both kVps and all three dose-levels,

Noise is higher for IQon images for each of the 6 acquisitions. Figure 7.9 confirms the noise trends described earlier where noise levels are lower at high dose and at 140-kVp.

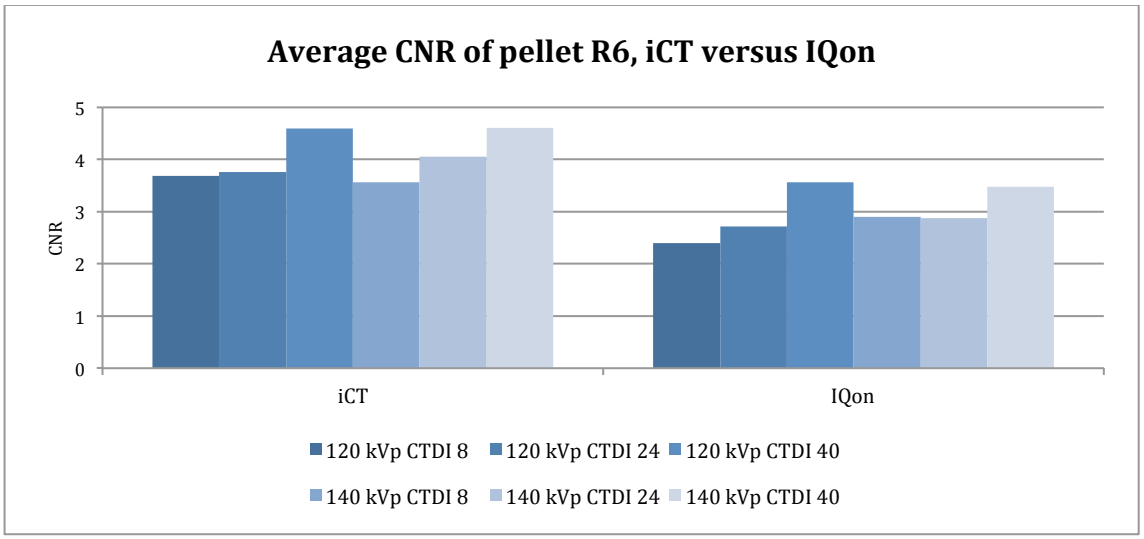

Figure 7.10: Average CNR of pellet R6; iCT versus IQon. Average CNR of the most affected pellets are significantly higher for iCT acquisitions at both kVps and all three dose-levels.

Average CNR values of pellet R6 are higher on the iCT at both tube-voltages and all three dose-levels. The highest CNR values are seen at high kVp and high dose.

7.2 Discussion

Image quality parameters are substantially better on the iCT for unaffected and by metal artefacts affected pellets. Mean HUs are more constant for iCT scans at both tube voltages and all three tube currents. Noise is lower and CNRs are higher for all iCT acquisitions. The effects of metal artefacts caused by the inserted metallic hip prosthesis are greatest on the IQon resulting in lower mean HUs, higher noise levels and lower CNRs. Therefore metal hip prostheses imaging is inferior on the IQon relative to iCT imaging in conventional mode. As far as we know, this is the first and only study that compared and quantified the differences in mean HUs, noise and CNRs with and without the influence of metallic composites on the iCT and IQon CT-scanners.

Without the insertion of a prosthesis, average mean HU values are 270 and 285 for respectively iCT and IQon images ($p<0.001$). Noise is significantly lower and CNR is higher for iCT images (29.15 versus 34.99 and 9.23 versus 8.30, $p<0.001$). When focusing on the most affected pellet R6, HU are lowest (113 versus 213), noise is higher (44.41 versus 31.93) and CNR is lower (2.99 versus 4.05) for IQon acquisitions.

The largest contributor of the observed differences is likely the difference in filtration used on the IQon. The role of tube filtration is to harden the X-ray spectrum by removing the low energy photons. A part of the filtration is reduced in order to enhance the separation between the low and high energies on the IQon. By removing a part of the filtration, the X-ray spectrum becomes much softer with more low energy photons. The low energy ones are much more sensitive to dense structures like metal. The reduced effective energy results in higher mean HUs and noise and reduced CNRs on IQon acquisitions, illustrated in Figures 7.3-7.5. The beam-hardening artefact is much larger at reduced filtration resulting in more severe artefacts on the IQon, as observed in Figures 7.6 and 7.8-7.10. Since the effect of metal artefacts is more severe for IQon acquisitions, it is expected that O-MAR is most effective on this scanner since O-MAR has shown to be most effective in case of severe artefacts.

7.3 Conclusions

Image quality parameters mean HU, noise and CNR are statistically different for similar conventional iCT and IQon acquisitions. For unaffected pellets, HU values are higher, noise is higher and CNRs are lower for IQon acquisitions using 120 and 140 kVp tube currents and $CTDI_{vol}$ dose-levels of 8, 24 and 40 mGy. When focussing on sensitivity for metal artefacts, conventional IQon acquisitions are more sensitive than conventional iCT acquisitions resulting in greater HU, noise and CNR deviations relative to baseline values of unaffected pellets. The observed differences are most pronounced in 120-kVp and low-dose acquisitions. These differences can be declared to differences in tube filtration since the beam-hardening artefact is much larger at reduced filtration resulting in more severe artefacts on the IQon. Conventional IQon imaging is therefore inferior to conventional iCT imaging in the CT-imaging of metallic composites. It is expected that monochromatic imaging at the IQon Spectral CT-scanner at high keVs will result in a reduction of metal artefacts. We will provide insides in the possible additional value of Spectral CT imaging in the following parts.

The effects of virtual monochromatic Spectral CT imaging in the CT-imaging of different prosthetic composites.

Purpose: To determine the effects of monochromatic Spectral CT-imaging of unilateral and bilateral hip prostheses of different metallic composites on mean HU, noise and CNR.

Methods and Materials: A water-filled phantom was used made of PMMA using six different prosthetic configurations with three different prostheses surrounded by 18 hydroxyapatite pellets representing bone. Scans were acquired on a 128-slice IQon Spectral CT scanner using low, normal and high dose (CTDI: 10, 20 and 30 mGy) at 120 and 140-kVp. Images were reconstructed with iterative reconstruction (IR, iDose^4 level 4) and analyzed at monochromatic energies from the range of 40 keV to 200 keV. Mean Hounsfield Unit, noise [HU] and CNR of all pellets with and without the insertion of several prostheses were calculated and analyzed using a standardized measurement template.

Results: Virtual monochromatic imaging at various energy levels over the full spectrum from 40 to 200 keV results in great variations in mean HUs and CNRs. Noise [HU] remains relatively constant over the entire keV spectrum. In low keV monochromatic images HU and CNR are high and these values decrease exponentially with increasing keV. HU values of unaffected HA pellets are similar at kVp equivalent keVs of 70 and 74 keV for respectively 120 and 140-kVp polychromatic results. 200 keV imaging is optimal in case of metal artefact reduction based on a full descriptive analysis of all six box configurations at 120 and 140-kVp.

Conclusions: Based on HU, noise and CNR trends obtained from 40-200 keV monochromatic images, a separation into four categories of metal artefacts can be made (no, mild, moderate and severe artefacts). Virtual monochromatic imaging results in a reduction of beam-hardening and streak artefacts in mild and moderate artefacts by decreasing deviations in HUs, noise and CNRs bringing these values back towards baseline values of unaffected pellets. The effectiveness of high keV monochromatic imaging in the reduction of metal artefacts strongly depends on the metallic alloy, the use of bilateral of unilateral prostheses and the distance and location of the pellets relative to the inserted prostheses.

8 Results of Part 3: Monochromatic Spectral CT imaging

To determine the effect of monochromatic CT-imaging on metal artefacts and image quality parameters we focussed on all 6 box configurations at standard dose of 20 mGy at 120 and 140-kVp reconstructed with iDose^4 level 4. Virtual monochromatic images where generated and analysed across the entire spectrum from a minimal keV of 40 till the maximal keV of 200 to determine optimal monochromatic energies in the CT-imaging of metal hip prostheses.

It is relevant to compare the image quality parameters HU accuracy, noise and CNR using monochromatic imaging and relate them to polychromatic imaging results, especially when executing a quantitative analysis. By taking all box configurations into account, the effect of different metallic alloys and bilateral hip prostheses can be evaluated. The entire keV-spectrum is analysed to determine the effect of monochromatic imaging and to select optimal keV-levels regarding metal artefact reduction, which will be used in further research. High keV monochromatic imaging is expected to reduce beam-hardening and scatter effect therefore reducing metal artefacts and improving image quality parameters.

Findings of this descriptive analysis will be used in order to investigate the effect of Spectral CT at different dose-levels and reconstruction algorithms in part 4.

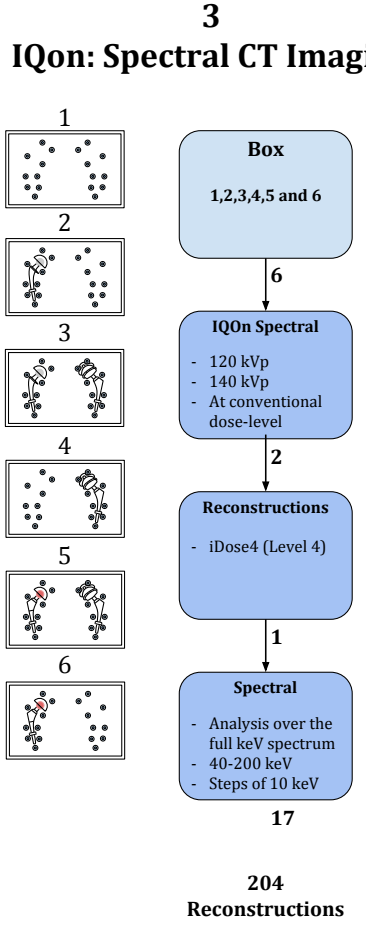

Figure 8.1: Overview of part 3.

First, the effect of monochromatic imaging on image quality parameters is evaluated without the insertion of a metal hip prosthesis. Extrapolation to low and high keV-levels heavily affects image quality parameters as Figure 8.2 illustrates. HUs and CNRs values are very high at 40 keV. It can be observed that extrapolation to higher keV results in a reduction in HUs and CNRs.

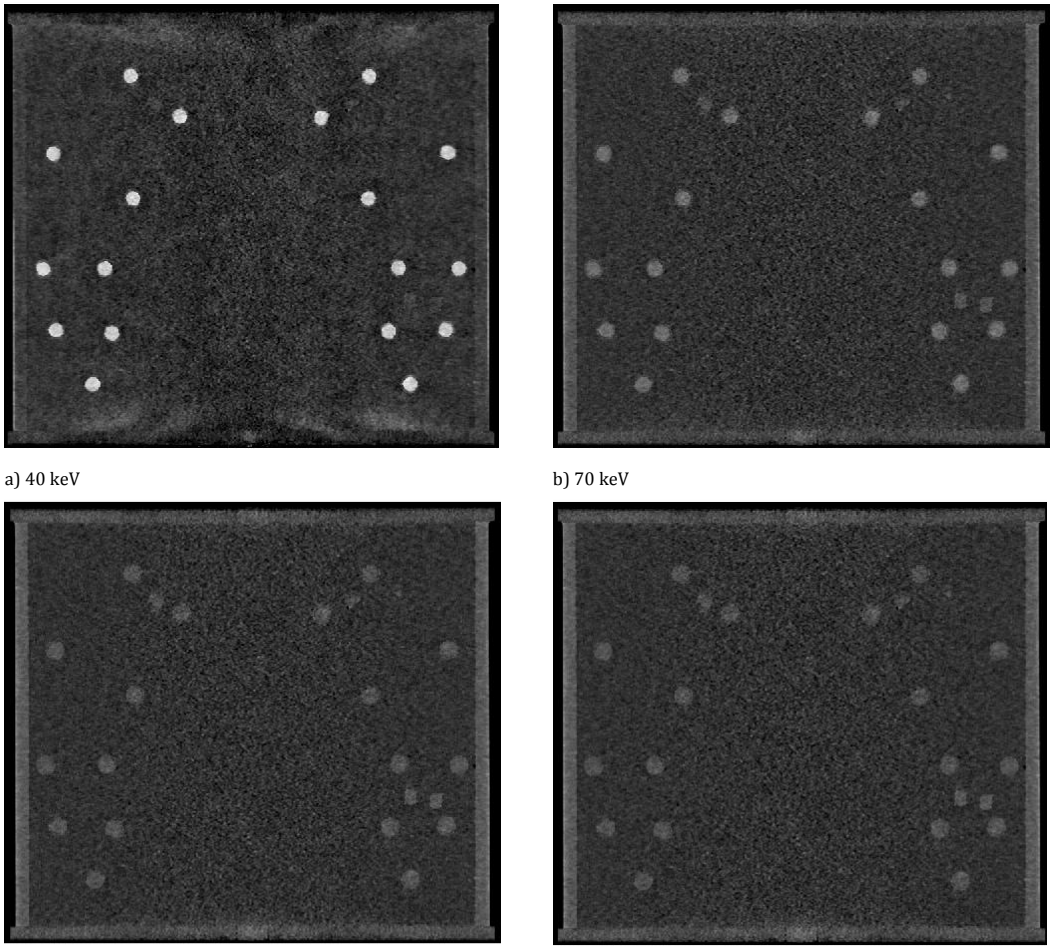

a) 40 keV

b) 70 keV

c) 140 keV

d) 200 keV

Figure 8.2: Spectral results of Box 1. Monochromatic imaging at a very low keV of 40 results in very high CNR. Extrapolating to the monochromatic keV of 200 results in a loss in contrast.

8.1 Average HU, noise and CNR trends without the insertion of a prosthesis

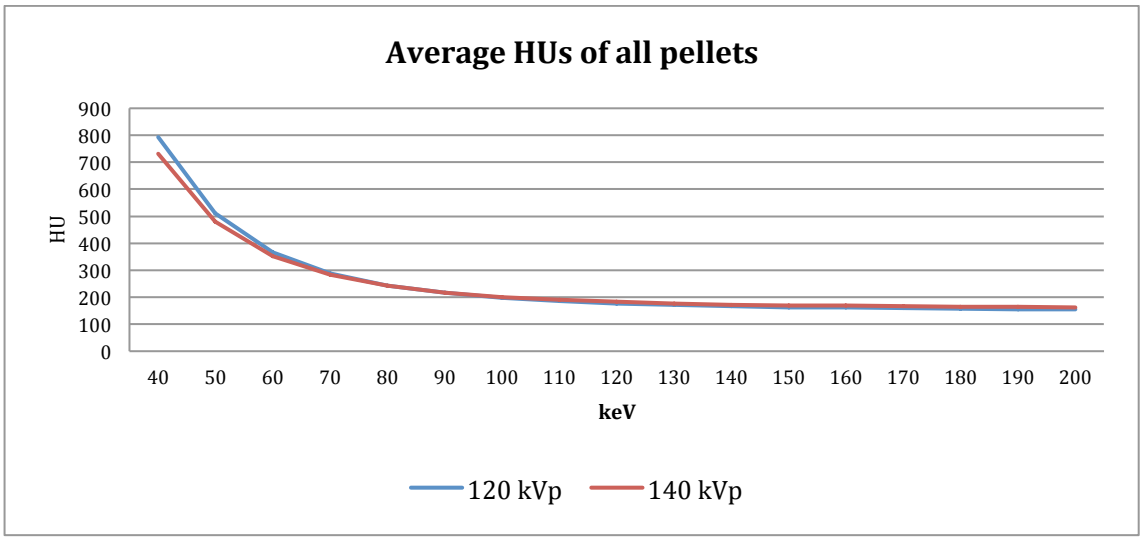

Figure 8.3: Average HU trends without the insertion of a prosthesis. HU values are very high at low keV and decrease exponentially when extrapolating to higher keVs. At around 70 keV, conventional HU values are observed.

Average HU values are high (700-800 HU) at low keV relative to reference HU values measured in conventional mode. Monochromatic keVs of 70 and 74 keV are the effective energies of polychromatic spectrums of respectively 120 and 140 kVp. At these 'kVp equivalent keVs' of 70 and 74 mean HU values are similar to polychromatic results with values around 250-300 HU. Extrapolation to high keV-levels results in a HU decrease to approximately 160 HU. Average HU values are higher for 120-kVp results at low keVs. At higher keV, starting from approximately 80 keV, HU values at 140-kVp are slightly higher but differences are negligible.

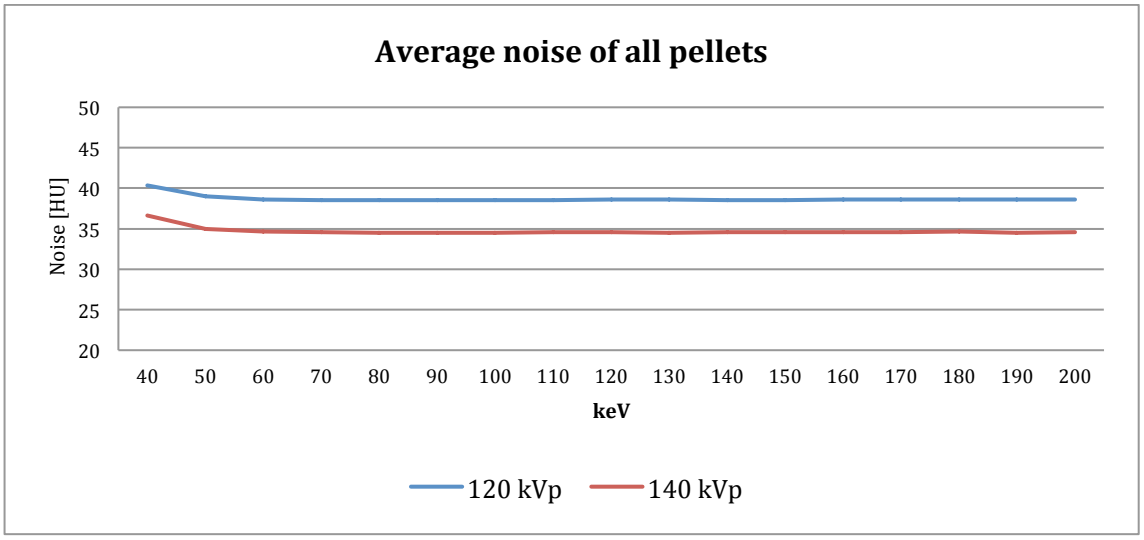

Figure 8.4: Average noise trends without the insertion of a prosthesis. Noise is constant when extrapolating to high keVs. Only a small increase in noise is observed at the monochromatic keV of 40.

Noise is higher for 120-kVp results compared to 140-kVp results at the same $CTDI_{vol}$, which confirms results obtained earlier regarding conventional images in part 1. Noise is slightly higher at low keV-levels but remains constant from approximately 60 keV up to the maximum keV of 200.

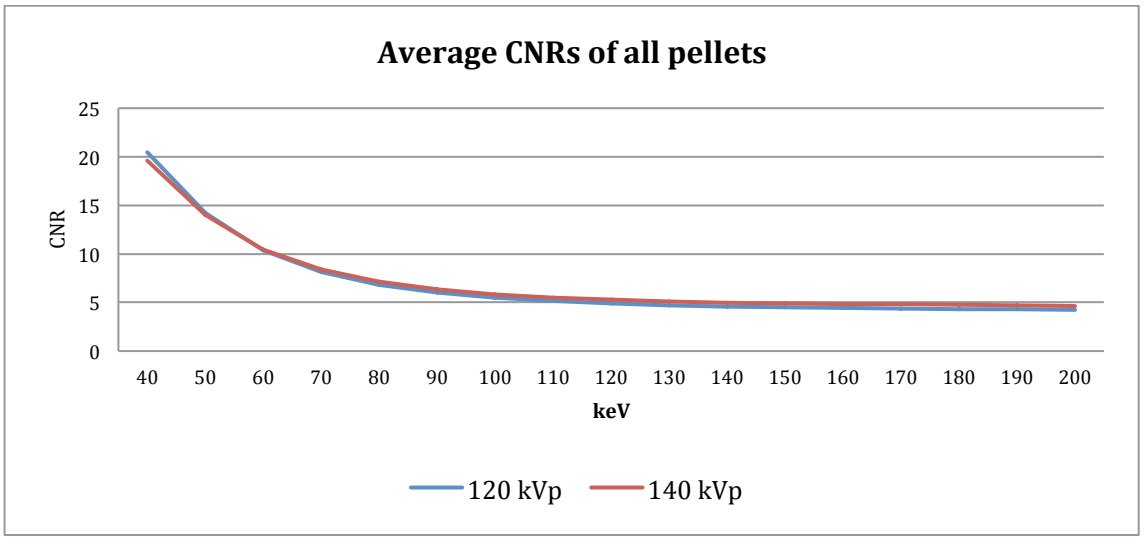

Figure 8.5: Average CNR trends without the insertion of a prosthesis. CNRs are high at low keV and decreases exponentially when extrapolating to high keVs.

CNR decreases exponentially when extrapolating to higher keV-levels. At a keV of 40, CNR values are about 250% higher due to a high contrast of the pellets relative to the background. At low keV till approximately 55 keV, 120-kVp results show higher CNR. Although differences in CNR can be observed between 120 and 140-kVp results, differences are very small.

Extrapolation to high keVs results in a CNR decrease of almost 50% relative to CNR values at the kVp equivalent keVs of 70 and 74. Since 140-kVp imaging is advised in case of metal involved imaging, a full spectrum analysis of 140-kVp results only will be shown within this part.

8.2 Spectral analysis with the insertion of bilateral prostheses (Box 3)

A full Spectrum analysis was performed for all box configurations involving metal prostheses from 40 to 200 keV regarding HU, noise and CNR trends for all pellets. Only the results of the bilateral prostheses configuration of box 3 will be shown in detail here. Results of the performed Spectral analysis on other box configurations are displayed in appendix A.

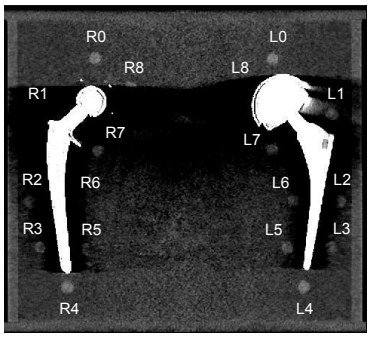

Figure 8.6: Box 3 including all 18 ROIs.

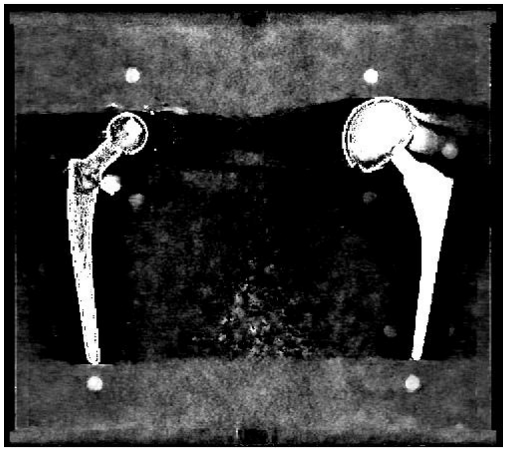

a) 40 keV

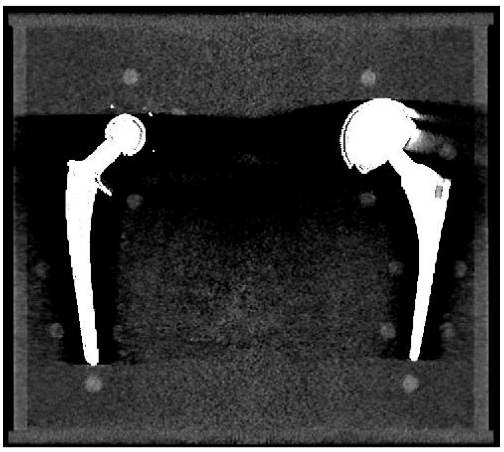

b) 70 keV

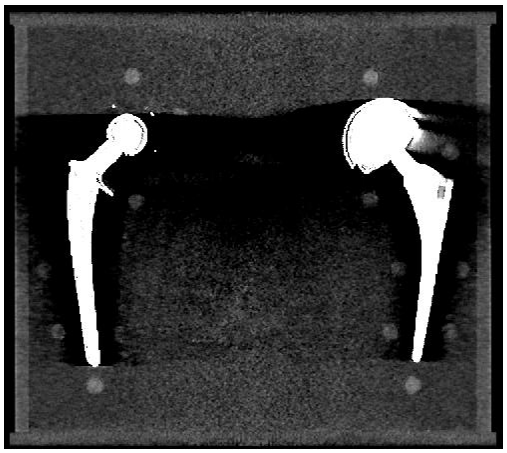

c) 140 keV

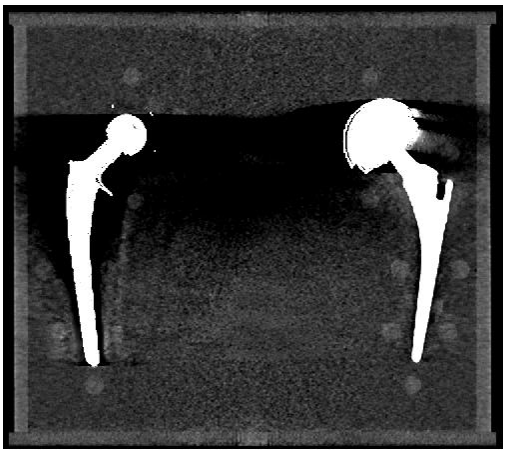

d) 200 keV

Figure 8.7: Monochromatic images at 40, 70, 140 and 200 keV. Metal artefacts are much more pronounced at low keV imaging. Extrapolating to higher keVs results in MAR. The effectiveness of high monochromatic keV imaging is clearly dependent on the kind of prosthesis and location of the pellets.

8.2.1 Analysis of the left pellets

HU values

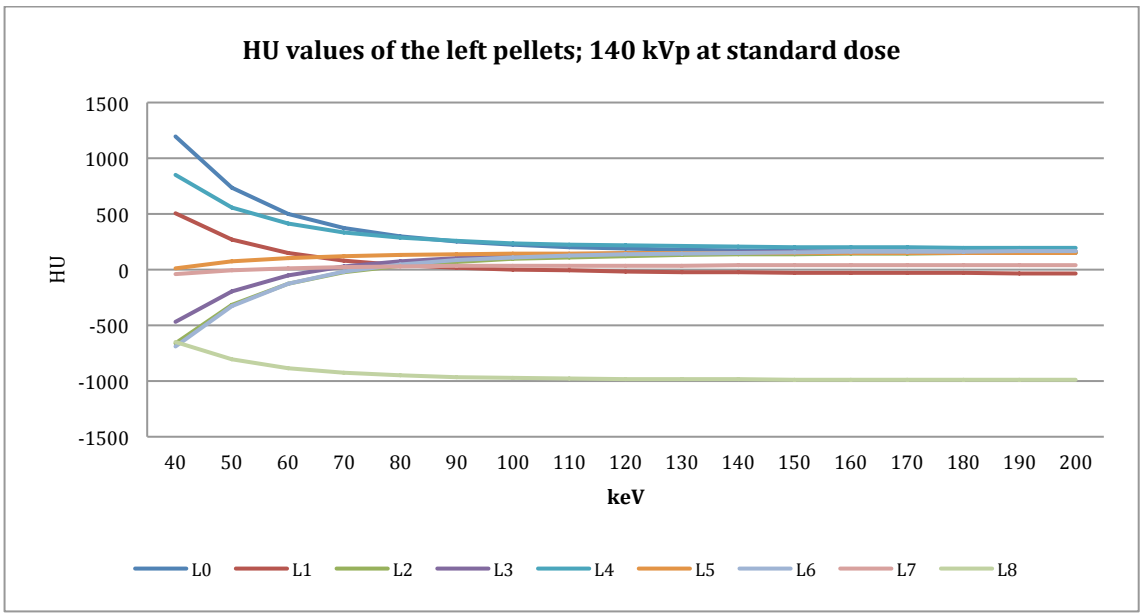

Figure 8.8: Average HU trends of the left pellets where different kind of pellets show various trends. HU value of pellet L8 is very low and decreases when extrapolating to high keVs.

Pellet L8 is severely affected by metal artefacts. The pellet remains invisible when extrapolating to higher keVs. HU of pellet L8 is low and decreases with increasing keV as unaffected pellets like L0 and L4 and R1. L4 is not totally unaffected as can be seen at very low keVs. HU values of pellet L2, L3 and L6 increase with increasing keV. HU values of pellet L5 and L7 are affected and remain more or less constant over the full keV spectrum. HU values of pellet L1 are lowered and decrease further with increasing keV.

Noise analysis

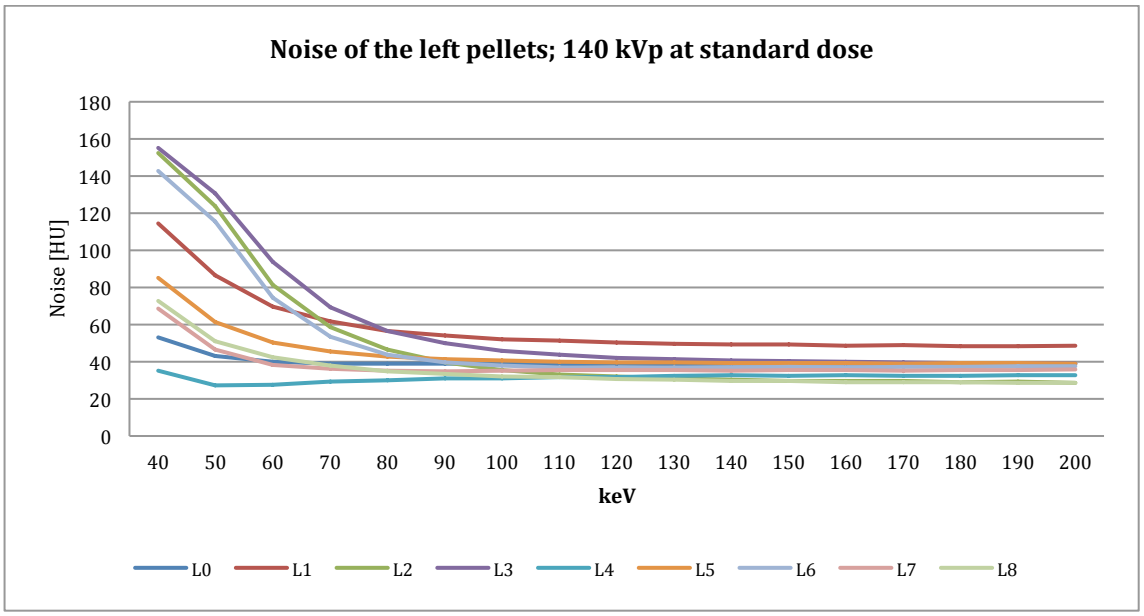

Figure 8.9: Average noise trends of the left pellets. Noise decreases when extrapolating to high keVs for all observed pellets.

Noise of all pellets decreases and remains relatively constant from approximately 80 keV and further. Noise levels are initially highest for pellets L2, L3, L6 and L1.

CNR values

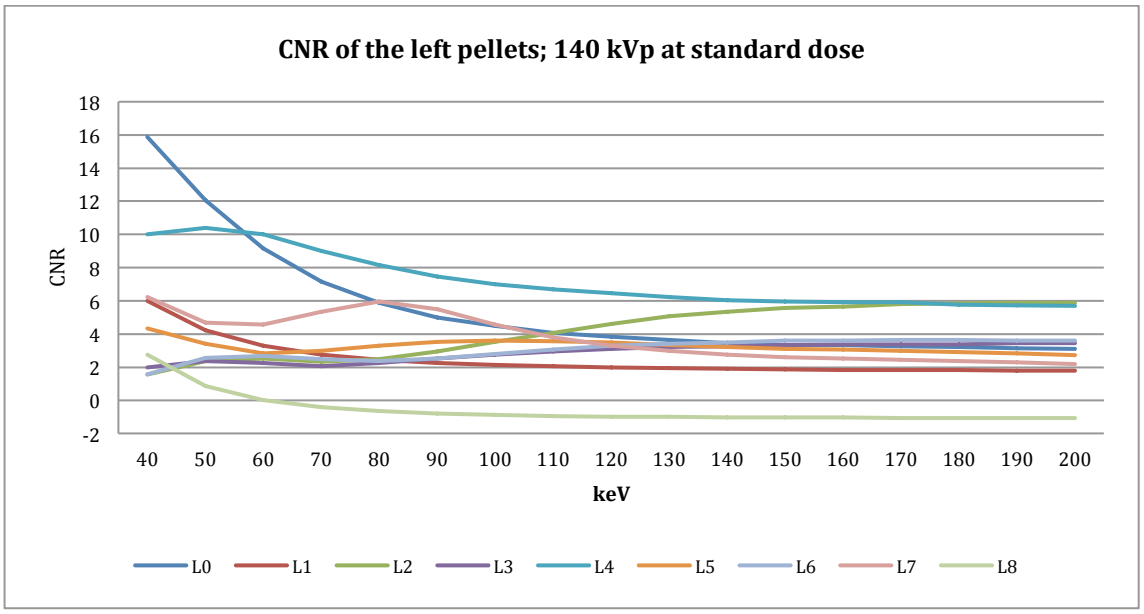

Figure 8.10: Average CNR trends of the left pellets. The pellets show different trends when extrapolating to high keVs. CNR of pellet L8 is low and even turns below zero when extrapolating to high keVs.

Pellets L2, L3 and L6 show a slight increase in CNR with increasing keV. CNR values decrease with increasing keV for pellet L0, L4, L1 and L8. CNR of pellet L8 is mostly distorted and decreases even further at higher keVs. Pellet L7 and L5 show a variable effect over the entire spectrum.

8.2.2 Analysis of the right pellets

HU values

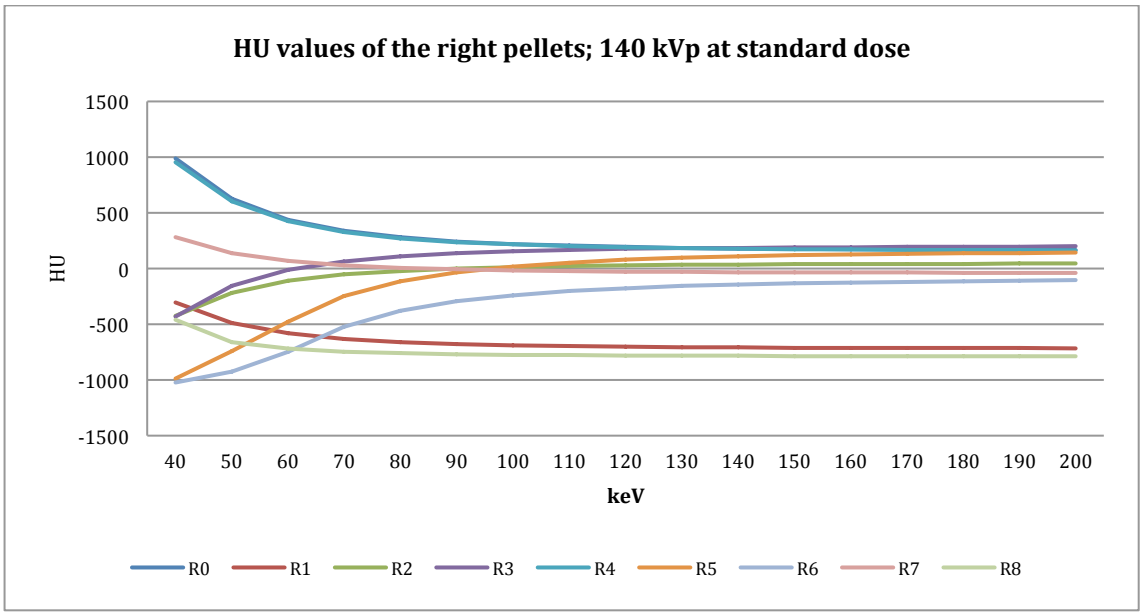

Figure 8.11: Average HU trends of the right pellets. Pellet R0 and R4 show no distortions in HU. Interesting increasing HU trends are observed for R2, R3, R5 and R6 when extrapolating to high keV. Pellet R1 and R8 show severe distortions.

Pellet R0 and R4 are unaffected by metal artefacts and HU values show the earlier described decreasing trend in case of no inserted prosthesis. Pellets R5 and R6 show a substantial positive effect when extrapolating to higher keV where HU and CNR increase to a certain steady state from around 140 / 150 keV. HU values of R5 and R6 increase with increasing keV, where R6 does not reach HU values of unaffected pellets Pellet R2 and R3 show a slight increase in HU values with increasing keVs, where pellet R1 and R7 show a slight decrease of HU values. Pellet R1 and R8 show heavily decrease HU values, which decrease even further when extrapolating to high keVs.

Noise

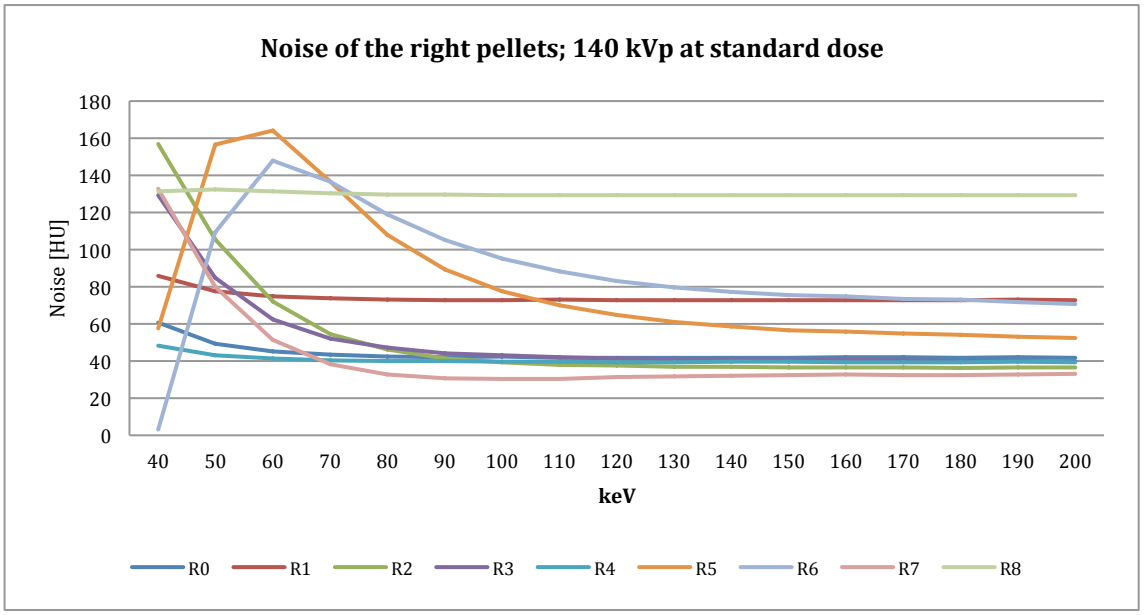

Figure 8.12: Average noise trends of the right pellets. CNR of the unaffected pellets R0 and R4 remain constantly low. Pellet R5 and R6 show an interesting noise trend when extrapolating to high keV where initially an increase is observed followed by an exponential decrease.

Average noise of pellets R0 and R4 are low and remain relatively constant as expected. Pellet R5 an R6 show an interesting trend where initially an increase in noise is observed followed by an exponential decrease from approximately 60 keV till 200 keV. Noise level of pellet R8 is very high and remains high. Also noise of pellet R1 is high and remains constant over the entire keV spectrum.

CNR values

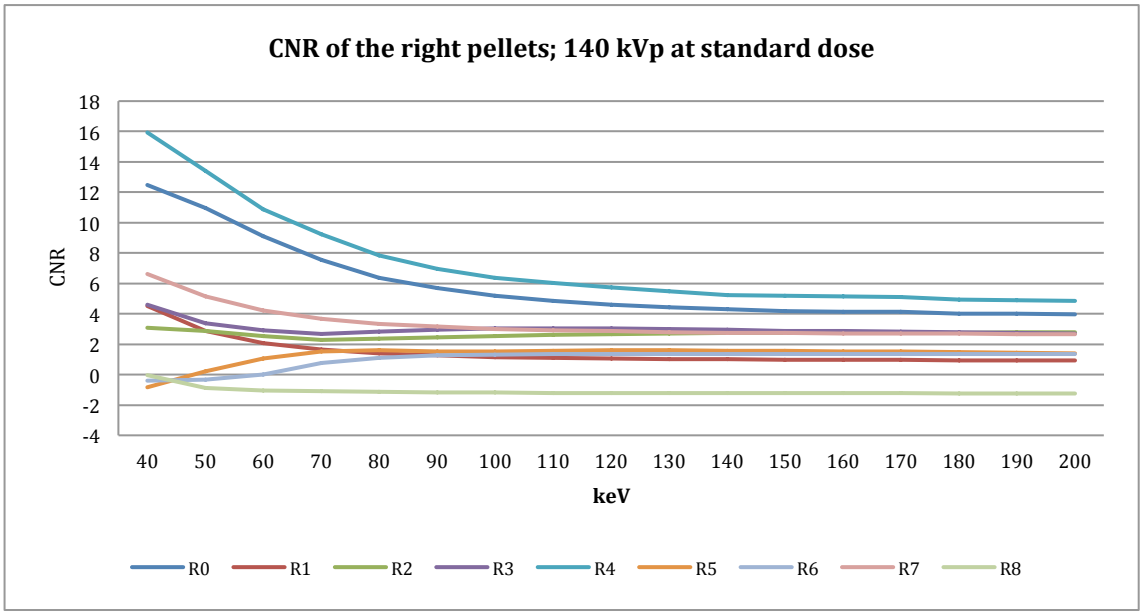

Figure 8.13: Average CNR trends of the right pellets. CNR of R5, R6 and R8 are very low. CNR of R5 and R6 increase when extrapolating to high keV where the CNR of R8 further decreases.

A decrease in CNR with increasing keV is observed for pellet R0 and R4 where the CNR of pellet R0 is slightly lower than for R4. CNR values of all the other pellets decrease with increasing keV apart from pellet R5 and R6. These pellets show a slight increase in CNR with increasing keV.

8.3 Trends in monochromatic Spectral CT imaging

Differences in the effectiveness of monochromatic Spectral CT imaging are observed when focusing on metal hip prostheses imaging. Six different boxes where analysed with three different prostheses. The data of all boxes was combined to categorize the degree of artefact severity. A separation can be made based on cut-off values in 70 and 74 keV images. This separation in different categories is expected to depend on the kind of metal, the thickness of the metal and the distance of the pellet to the prostheses. Based on the full keV-spectrum analysis of all pellets and all box configurations conducted from 140-kVp standard dose results we have composed sketches of HU, noise and CNR trends in the monochromatic CT imaging of metal hip prostheses. The composed sketches are illustrated in Figures 8.14, 8.15 and 8.16.

In general, a categorization into four grades of metal artefacts is made with matching trends in HU, noise and CNR.

No artefacts	HU and CNR decrease with increasing keV. Noise is relatively constant from low to high keV.
Mild artefacts	HU decreases with increasing keV till baseline HU of unaffected pellets. CNR remain relatively constant with increasing keV and will reach baseline levels of unaffected pellets. Noise reduces exponentially.
Moderate artefacts	HU and CNR increase with increasing keV but will not reach baseline levels of unaffected pellets. Noise is initially very low and increases greatly up to around 60 keV. From 60 keV noise exponentially decreases.
Severe artefacts	HU values are low/negative and decrease even further with increasing keV. CNR values are also very low/negative and decrease slightly with increasing keV. Noise is very high and remains high through the entire keV spectrum.

HU trend

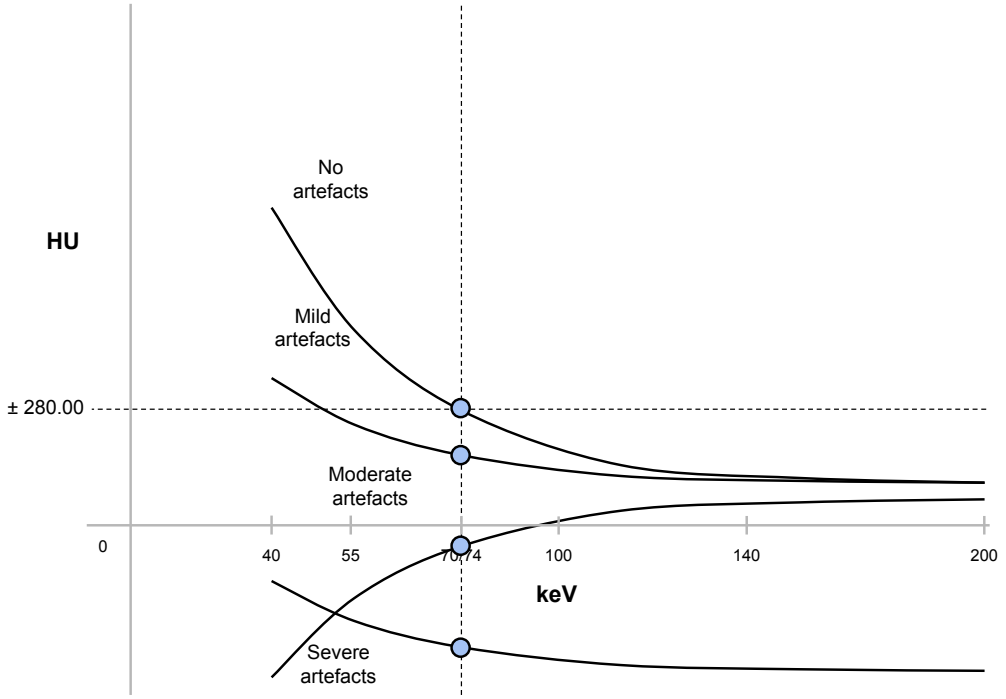

Figure 8.14: HU trends in monochromatic CT-imaging divided into four categories. Categorization can be made by evaluating values at the kVp equivalent keV of 70 and 74 keV for respectively 120 and 140-kVp acquisitions.

Noise trend

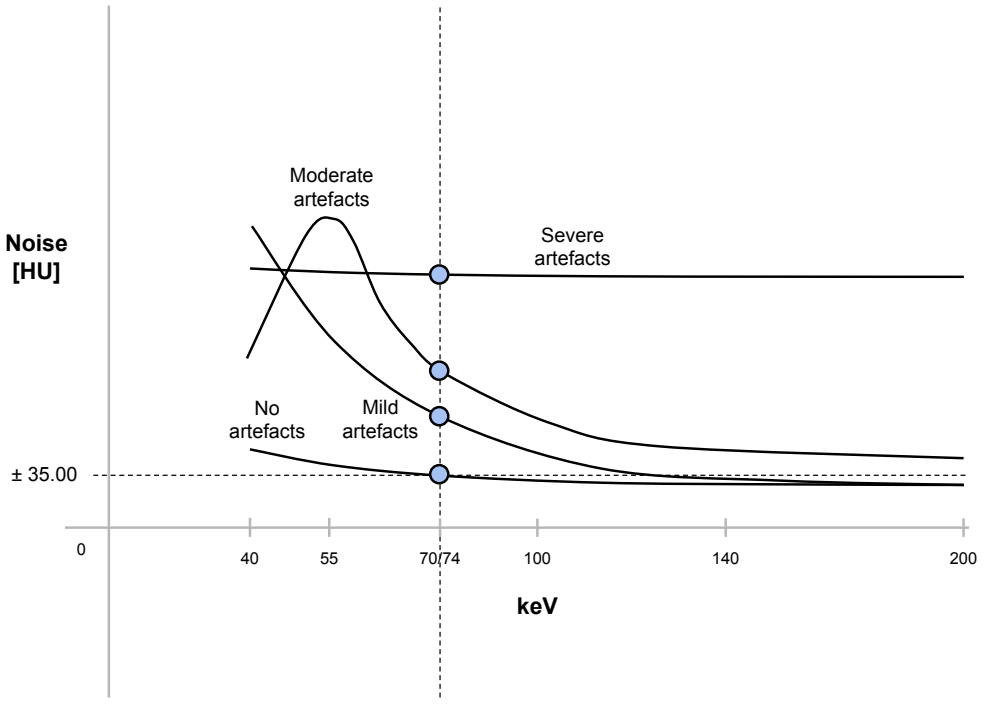

Figure 8.15: Noise trends in monochromatic CT-imaging divided into four categories Categorization can be made by evaluating values at the kVp equivalent keV of 70 and 74 keV for respectively 120 and 140 kVp acquisitions.

CNR trend

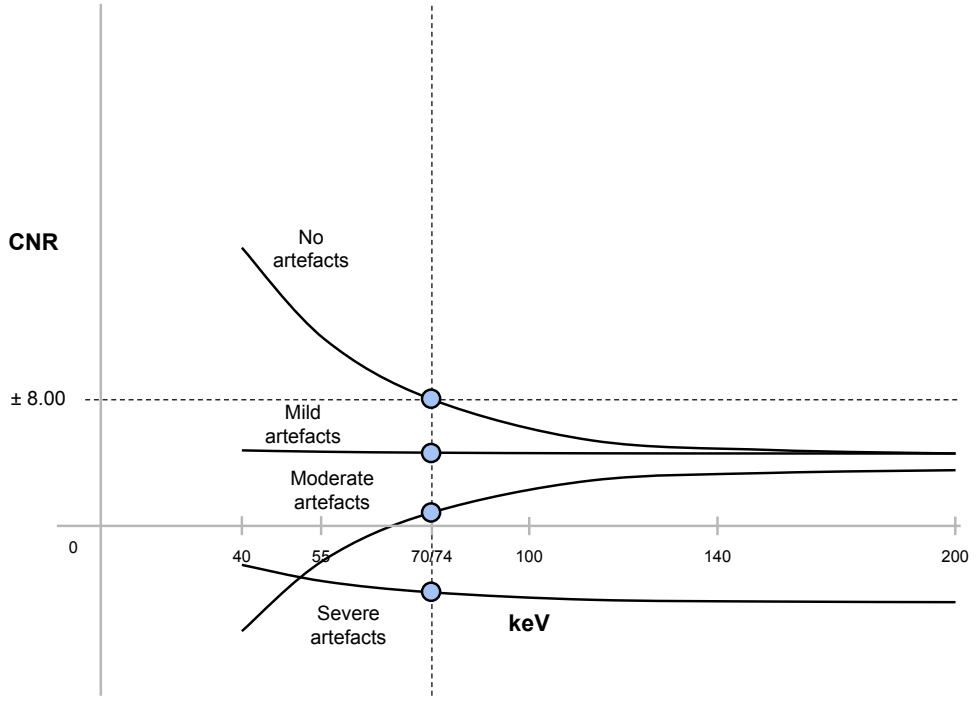

Figure 8.16: CNR trends in monochromatic CT-imaging divided into four categories. Categorization can be made by evaluating values at the kVp equivalent keV of 70 and 74 keV for respectively 120 and 140 kVp acquisitions.

8.4 Discussion

Monochromatic imaging results in large overall decrease in mean HU and CNR over the full range from 40 to 200 keV. The results show high HU values at low keV resulting in a high contrast and high CNR values. Mean HUs decrease exponentially as with CNRs. CNRs mainly decrease due to a loss in contrast since the noise component only shows a slight decrease from 40 till 60 keV and remains constant starting from 60 keV up to 200 keV.

Metal artefacts are a mixture of beam-hardening, photon starvation and scatter. Monochromatic Spectral CT imaging reduces metal artefacts by reducing the beam-hardening component. The photon starvation component, which is enhanced by metals with higher atomic weight, cannot be corrected for using high keV monochromatic extrapolation. Therefore MAR results are substantially better in case of the titanium-aluminium-vanadium alloy with a lower atomic weight. The aim of this part was to obtain HU, noise and CNR trends with and without the insertion of a metal prosthesis. Based on cut-off values at affective energies of 70 and 74 keV a categorization between no, mild, moderate and severe artefacts can be made. Like several similar studies on monochromatic CT imaging, we found that monochromatic imaging at keVs higher than the effective energies of 70 and 74 keV from 120 and 140 kVp polychromatic CT images reduces the degree of metal artefacts substantially (11–13,24). Increasing the monochromatic keV reduces the degree of metal artefacts but subsequently decreases overall contrast in the images.

The Spectral iterative reconstruction contains a dedicated de-noising algorithm which takes the nature of the noise in the Spectral decomposition into account to de-noise the photoelectric and Compton images (47). Without this algorithm it is expected that the noise heavily increases at low and high keV. The consequence of these high noise values would result in a suboptimal result at very high keV regarding metal artefact reduction. With this algorithm hardly no differences in noise are observed between 140 keV and 200 keV. The constant noise level of unaffected pellets over the entire keV spectrum confirms the effectiveness of the de-noising algorithm.

The noise trend observed in case of moderate artefacts stands out, illustrated in Figure 8.15. Initially, noise values are low and increase rapidly up to a keV of about 60. Then from about 60 keV noise decreases exponentially. It seems that at very low monochromatic keVs, no or little information is present due to the influence of metal artefacts resulting in large dark areas. The degree in metal artefact will be greater at low energies since low energy photons are more attenuated by metal. Noise increases due to the appearing information by the reduction of metal artefacts therefore increasing the variation of values within the ROIs. From about 60 keV, the monochromatic approach results in a further reduction of the beam-hardening component thereby also reducing noise.

Unaffected and severely affected pellets behave similar with increasing keV when focussing on mean HU and CNR trends. They both show decreasing HU and CNR with increasing keV where severely affected pellets show this behaviour at very low/negative starting points. The effectiveness of monochromatic imaging in MAR depends on the metallic alloy. The cobalt-chrome-molybdenum alloy prosthesis in case of Box 2 and 3 causes severe metal artefacts, as expected due to higher atomic numbers. When extrapolating to higher keV no or little MAR is observed. Only at the bottom of the stem some metal artefact reduction can be observed. The

titanium-aluminium-vanadium allow present in the stem of the MoM-prosthesis results in less severe artefacts. When extrapolating to higher keV, hardly no metal artefacts are observed despite the loss in contrast of the pellets. No or hardly no MAR is observed at the cobalt-chrome-molybdenum head of the MoM-prosthesis. The prosthesis used in box 6 with the same titanium-aluminium-vanadium stem, a UHMWPE cup and ceramic head show the least artefacts relative to the other configurations.

Box configuration 3 shows the most severe artefacts due to several reasons. It contains 2 prostheses resulting in more severe artefacts relative to unilateral prosthesis configurations. The metallic composite of the entire right prosthesis and the head of the MoM-prostheses consist of a cobalt-chrome-molybdenum alloy with a higher attenuation relative to the titanium-aluminium-vanadium alloy and ceramic composites.

The 120-kVp results will be evaluated additionally in the next part where we also focussed on the effect of Spectral CT imaging regarding different dose-levels and kVp settings. It is expected that 140-kVp results are superior to 120-kVp results due to a higher energy of the photons therefore encounter less attenuation by the metallic composites.

8.5 Conclusions

Virtual monochromatic imaging at various energy levels over the full spectrum from 40 to 200 keV results in decrease in mean HUs and CNRs. Noise remains relatively constant over the entire keV spectrum. Initially, in 40 keV monochromatic images mean HUs and CNRs are high and show a substantial exponential decay. HU values of unaffected HA pellets are similar at kVp equivalent keVs of approximately 70 and 74 keV for respectively 120 and 140-kVp polychromatic results. 200 keV imaging is optimal in case of metal artefact reduction based on the analysis of all 6 box configurations at 120 and 140-kVp. The degree of metal artefacts decreases up to 200 keV results but overall image contrast is reduced at these high keVs. High-keV monochromatic imaging results in a reduction of beam hardening and streak-artefacts by increasing distorted HUs and CNRs and bringing these values back towards baseline values of unaffected pellets. Based on mean HU, noise and CNR trends obtained from 40-200 keV monochromatic images, a separation into no, mild, moderate and severe artefacts can be made illustrated in Figures 8.14-16. The effectiveness of high keV monochromatic imaging in the reduction of metal artefacts strongly depends on the metallic alloy, the use of bilateral or unilateral prostheses and the distance and location of the pellets relative to the inserted prostheses. In the next part we will focus on value of monochromatic Spectral CT imaging in a quantitative way.

The effectiveness in metal artefact reduction (MAR) on a Spectral CT-scanner using an orthopaedic metal artefact reduction algorithm and high-keV monochromatic CT-imaging; a quantitative analysis.

Purpose: To quantify the effectiveness in MAR on deviated mean HUs, noise and CNRs using O-MAR and high keV monochromatic imaging in the CT-imaging of metal hip prostheses.

Methods and Materials: A water-filled phantom was used made of PMMA using unilateral and bilateral hip prostheses surrounded by 18 hydroxyapatite pellets representing bone. Scans were acquired on a 128-slice dual-layer detector IQon Spectral CT scanner using low, normal and high dose (CTDI: 10, 20 and 30 mGy) at 120 and 140-kVp. Conventional images were reconstructed using iterative reconstruction (IR, iDose^4 level 4) with and without the use of O-MAR. Monochromatic images were reconstructed with iterative reconstruction (IR, iDose^4 level 4) and analyzed at monochromatic energies of 55, 70 or 74, 100, 140 and 200 keV. Conventional images with and without the use of O-MAR will be compared to corresponding monochromatic 70 or 74 keV and 200 keV images to quantify the rate of MAR at various kVps and mAs'. Mean Hounsfield Unit, noise [HU] and CNR of all pellets with and without the insertion of several prostheses were calculated and analyzed using a standardized measurement template.

Results: Image quality parameters are superior for conventional IQon images relative to Spectral monochromatic kVp equivalent images at similar kVp and dose levels. Noise [HU] is lower ($p<0.05$) and CNRs are higher ($p<0.001$) for conventional polychromatic IQon images. CT numbers are accurate for 120 and 140-kVp at monochromatic keVs of respectively 70 and 74. Metal artefacts have a greater impact in Spectral CT imaging at the kVp equivalent keV of 70 and 74 keV relative to conventional IQon images. Mean HUs are lower, noise [HU] is higher and CNRs are lower for Spectral images for mild, moderate and severe artefacts. O-MAR is more effective in correcting deviated HUs, noise and CNRs compared to the high-keV monochromatic imaging at 100, 140 and 200 keV.

Conclusions: Virtual monochromatic images provides acceptable image quality to conventional 120 and 140-kVp images at similar $CTDI_{vol}$. However, noise [HU] is lower and CNRs are higher for conventional polychromatic IQon results. Virtual monochromatic imaging has the potential to reduce beam-hardening and streak-artefacts. Virtual high-keV monochromatic imaging itself is most effective in case of moderate artefacts. O-MAR is superior in MAR since absolute corrections towards reference HUs, noise and CNRs are greater for all categories of artefacts. Additionally, O-MAR has no effect on mean HU, noise [HU] and CNR in the absence metal artefacts where 200 keV monochromatic imaging results in a loss in contrast and consequently in CNR in unaffected regions. Virtual high-keV monochromatic imaging can only correct for beam-hardening and not for metal artefacts caused by photon-starvation, unlike O-MAR.

9 Results of Part 4:
High keV monochromatic Spectral CT-imaging versus conventional CT-imaging in MAR on the IQon

In the fourth part we want to determine the single additional value of monochromatic Spectral CT imaging versus conventional imaging in the reduction of metal artefacts. All scans are acquired on the same IQon scanner so no differences are present in filtration, detector raw or collimation. To quantify the effects of Spectral CT imaging in MAR, results are matched to conventional scans with and without the use of the available orthopaedic metal artefact reduction algorithm O-MAR.

To evaluate the image quality of virtual monochromatic images obtained from dual-energy scans, two questions need to be answered. One question is how well the beam-hardening artefact can be corrected for and how accurate the CT numbers can be at various monochromatic keVs. The other question is how the quality of virtual monochromatic images is related to conventional single-energy CT images acquired with polychromatic x-ray beams and the same radiation dose.

We focussed on three box configurations for further analysis. The worst-case scenario box configuration 3 contains bilateral prostheses causing the most severe metal artefacts. The second box configuration chosen for analysis is the most commonly used prosthesis used in box configuration 6, which cause the least metal artefacts as shown in the previous part. Box configuration 1 without the insertion of a prosthesis serves as a reference.

Scans of these three box configurations are obtained at 120 and 140-kVp at three different $CTDI_{vol}$ dose-levels of 10, 20 and 30 mGy. Scans are reconstructed with iDose^4 level 4. Conventional scans are additionally reconstructed using the O-MAR algorithm. No additional scanning was needed since Spectral analysis only requires a Spectral reconstruction.

This part is divided into three parts to fully quantify the additional value of Spectral CT imaging and relate these results to conventional images with and without the use of O-MAR.

1) A quantitative analysis at different kVp and dose levels without the insertion of a prosthesis.

2) A quantitative analysis of high-keV monochromatic CT imaging versus polychromatic CT imaging and O-MAR with respect to metal artefact reduction in bilateral hip prostheses.

3) A quantitative analysis of high-keV monochromatic CT imaging versus polychromatic CT imaging and O-MAR with respect to metal artefact reduction in the most common unilateral hip prostheses.

To investigate the value of Spectral CT imaging for different kVps, different dose-levels and different prostheses a compromise in keV selection is made due to the otherwise excessive amount of data. In order to analyse the entire relevant spectrum, 5 monochromatic keVs are taken into account based on the kVp equivalent keV levels for 120 and 140-kVp. Monochromatic images analysed at the kVp equivalent keV can be compared with polychromatic conventional image. The kVp equivalent keV for 120 and 140-kVp are respectively 70 and 74 keV and are obtained by varying the energy of monochromatic images and relate HU values to HU values in the conventional polychromatic images.

Since Spectral CT imaging has shown to be most valuable at high keV in MAR, three high keV levels of 100, 140 and 200 keV and one low keV of 55 keV level are selected.

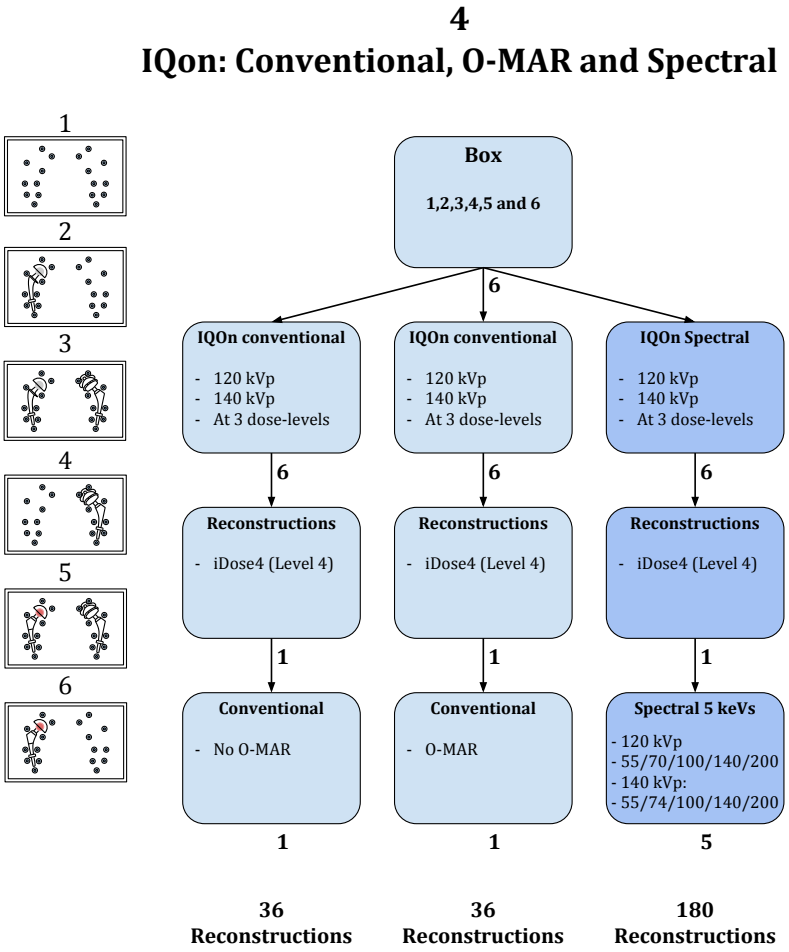

Figure 9.1: Overview of part 4.

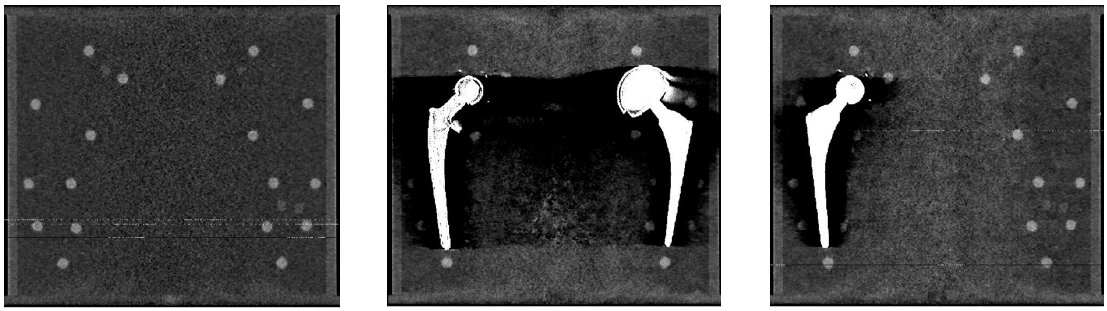

a) Box 1, 55 keV b) Box 3, 55 keV c) Box 6, 55 keV

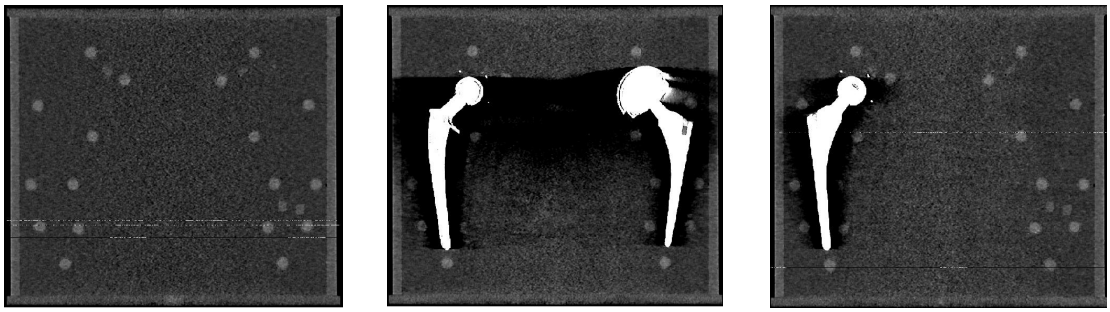

d) Box 1, 74 keV e) Box 3, 74 keV f) Box 6, 74 keV

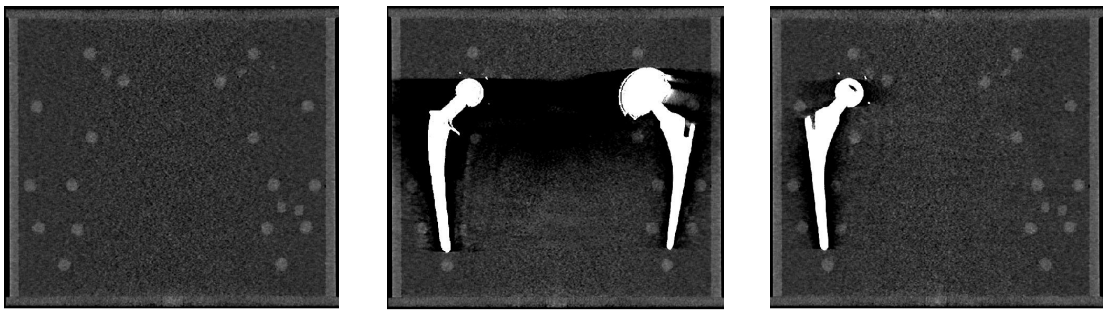

g) Box 1, 100 keV h) Box 3, 100 keV i) Box 6, 100 keV

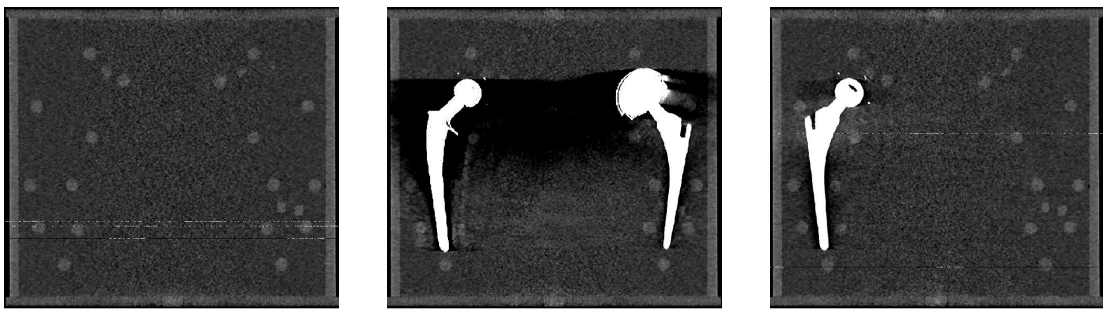

j) Box 1, 140 keV k) Box 3, 140 keV l), Box 6, 140 keV

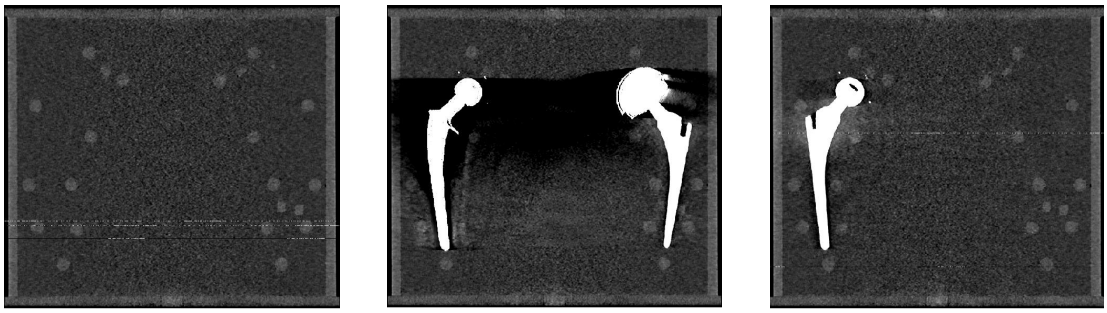

m), Box 1, 200 keV n), Box 3, 200 keV o), Box 6, 200 keV

Figure 9.2 (a-o): Monochromatic images of box 1, 3 and 6 at 40, 74, 100, 140 and 200 keV. Extrapolating to high keV results in a loss in contrast and a reduction of metal artefacts. MAR using high keV monochromatic imaging is more effective for box configuration 6.

9.1 A quantitative analysis at different kVp and dose levels without the insertion of a prosthesis.

Average HU values

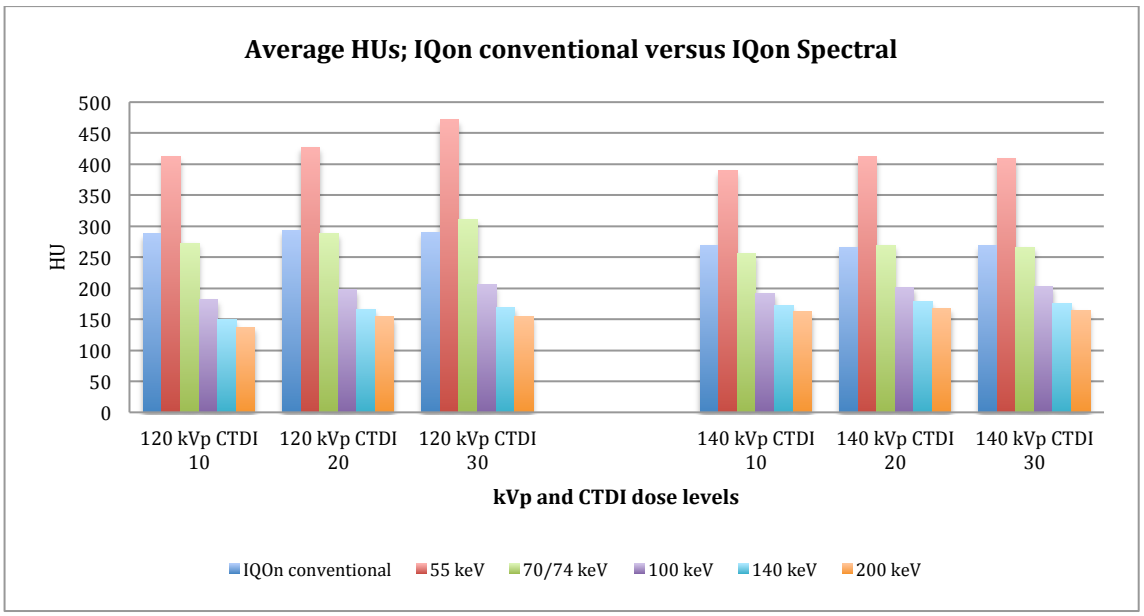

Figure 9.3: Average HU values; IQon concentional versus spectral. Average HU values are quite similar to the kVp equivalent keV of 70 and 74 for respectively 120 and 140-kVp acquisitions. 55 keV imaging results in higher HU values where high keV imaging results in lower HU values.

Average HU values on the IQon in conventional are similar to the kVp equivalent keV, with no significant differences, since we conducted the kVp equivalent keV level based on similarities in HU values.

HU trends in the Spectral results confirm earlier observations where low keV images result in substantial higher HU values. When increasing the keV, HU values decrease exponentially. Monochromatic imaging at 200 keV results in an average decrease in HU values of 49% (142) and 38% (100) relative to the HU values at 70 and 74 keV for respectively 120 and 140-kVp acquisitions.

Average noise

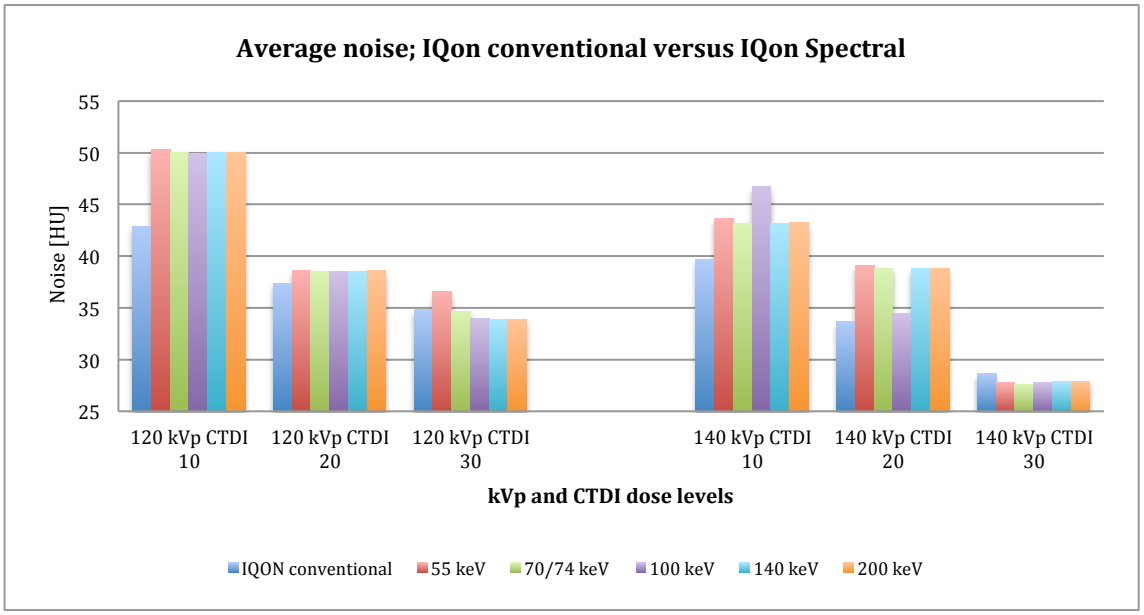

Figure 9.4: Average noise; IQon conventional versus spectral. Noise is generally higher for Spectral results.

Average noise levels decrease with increased radiation dose as expected. Also noise at 140-kVp is lower for each dose level in conventional mode relative to 120-kVp. Average noise in the spectral analysis behaves as expected where noise levels are slightly higher at low keV and show little variation up to high keVs. This confirms the slight exponentially decreasing behaviour of spectral noise earlier described in the previous section. It can be observed that differences between keV levels are negligibly small, especially for higher keVs.

Average noise in the conventional images is slightly lower at $CTDI_{vol}$ dose levels of 10 mGy and 20 mGy. At 30 mGy, noise levels show different behaviour at 120 and 140-kVp for varying keV selections. The 100 keV images at 140-kVp at a dose of 10 and 20 mGy contained no artefact as can be seen in Figure 9.2, where the 55, 74, 140 and 200 keV images contained artefacts. This can explain the unexpected differences in noise levels between the 5 different keVs.

Noise for conventional polychromatic IQon images is lower where the observed differences are significant ($p<0.001$, with a partial Eta Squared of 0.607 for the within subject factor kVp and $CTDI_{vol}$ setting with 6 levels and 0.514 for the within subject factor scanners with 3 levels).

Average CNR values

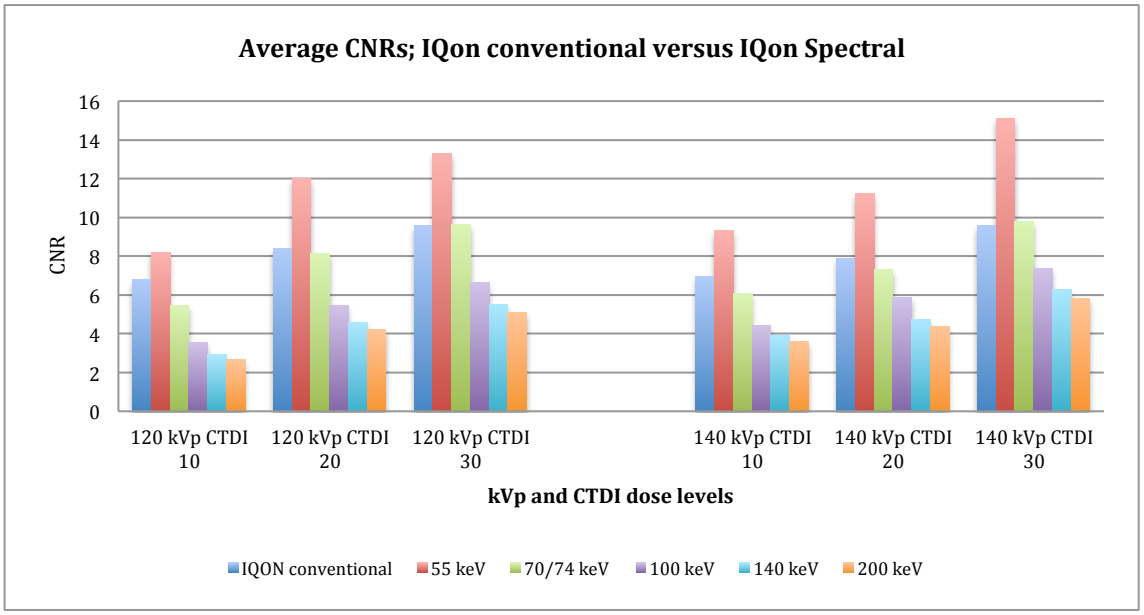

Figure 9.5: Average CNR values; IQon conventional versus Spectral images.

Trends in average CNR values confirm earlier observations since CNR improve at higher $CTDI_{vol}$ and decrease with increasing keV. Little differences are observed in average CNR between conventional results and corresponding kVp equivalent keV analysis of 70 and 74 keV for respectively 120 and 140-kVp results.

Monochromatic imaging at 200 keV results in an average decrease in CNR values of 49% (3.76) and 40% (3.19) relative to the CNR values at 70 and 74 keV for respectively 120 and 140-kVp acquisitions.

CNR for conventional polychromatic IQon images is higher where the observed differences are significant ($p<0.001$, with a partial Eta Squared of 0.667 for the within subject factor kVp and $CTDI_{vol}$ setting with 6 levels and 0.684 for the within subject factor scan technique with 2 levels).

9.2 A quantitative analysis: high keV monochromatic CT imaging versus O-MAR in the reduction of metal artefacts in bilateral hip prostheses.

The effect of O-MAR and monochromatic Spectral CT imaging in metal hip prostheses imaging is subsequently divided into 4 categories as described earlier: the effect on no artefacts, mild artefacts, moderate artefacts and severe artefacts. Categorization took place by analysing HU, noise and CNR based on O-MAR and Spectral results at 140-kVp at standard dose. A comparative analysis is given for box configuration 3 and 6 in order to take the worst-case bilateral prostheses configuration and the most commonly used prosthesis into account.

No artefacts	L0, L4, R0 and R4
Mild artefacts	L1, L2, L3, L5, L6, L7, R2, R3 and R7.
Moderate artefacts	R5 and R6
Severe artefacts	L8, R1 and R8

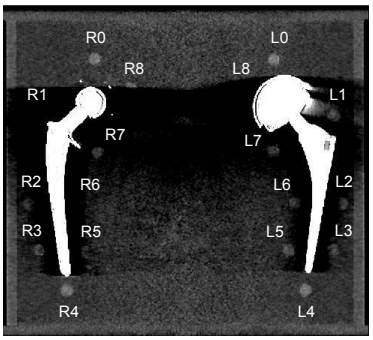

Figure 9.6 Box 3 including all 18 ROIs.

The rate of MAR is evaluated for both polychromatic conventional CT-imaging and monochromatic CT-imaging. In all cases the conventional images and O-MAR images are compared to the corresponding monochromatic 70 or 74 keV images and the extrapolated monochromatic 200 keV images. The extrapolated energy of 200 keV is chosen as the optimal monochromatic keV in MAR based on the earlier described trends. From the range of 140 keV till 200 keV HU values show a minimal decrease where noise decreases and CNR still increases up to 200 keV.

Average HU values

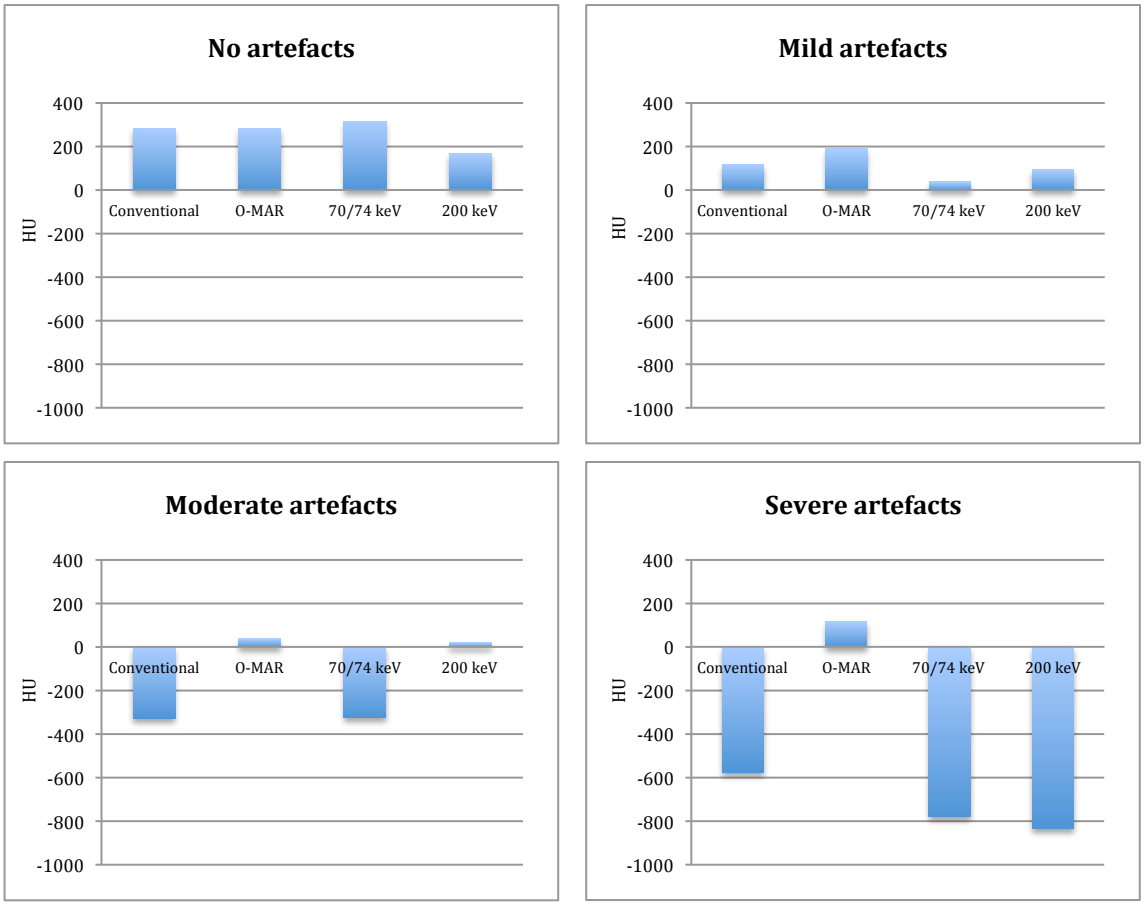

Figure 9.7: Effects of O-MAR and 200 keV imaging divided into four categories. O-MAR has no effect on unaffected pellets and is most effective in case of severe artefacts resulting in the greatest HU increase. Spectral MAR is most optimal in case of moderate artefacts.

Average HU values of the unaffected pellets L0, L4, R0 and R4 show expected trends at clearly higher HU levels. The exact same 5 pellets which showed the greatest deviation relative to reference values stand out in the Spectral results. Pellets L8, R1, R5, R6 and R8 show very low HU values at low keV energies. A seperation can be made between severe artefacts (pellet R1, L8 and R8) and moderate artefacts (pellet R5 and R6). Average HU values of the severy distorted pellets are lower in the Spectral results relative to the conventional images.

O-MAR greatly improves HU distortions towards reference values for pellets that heavily affected by metal artefacts. Pellets which are most affected are L8, R1, R5, R6 and R8. O-MAR lifts the HU of pellet R8 most towards reference values. O-MAR is capable of increasing all these very low HU values greatly. When increasing keV levels, no such trend can be observed. The decreasing HU trend of severely affected pellets in the Spectral results is similar to the trend of unaffected pellets as described earlier, only at a lowere baseline HU.

The average HU values of R5 and R6 are similar for the conventional results and the corresponding equivalent keV of 74. Extrapolation to higher keV improves HU values greatly where HU values of R5 return to reference values of unaffected pellets. HU values of pellet R6 are initially lower and do not reach reference values.

Average noise

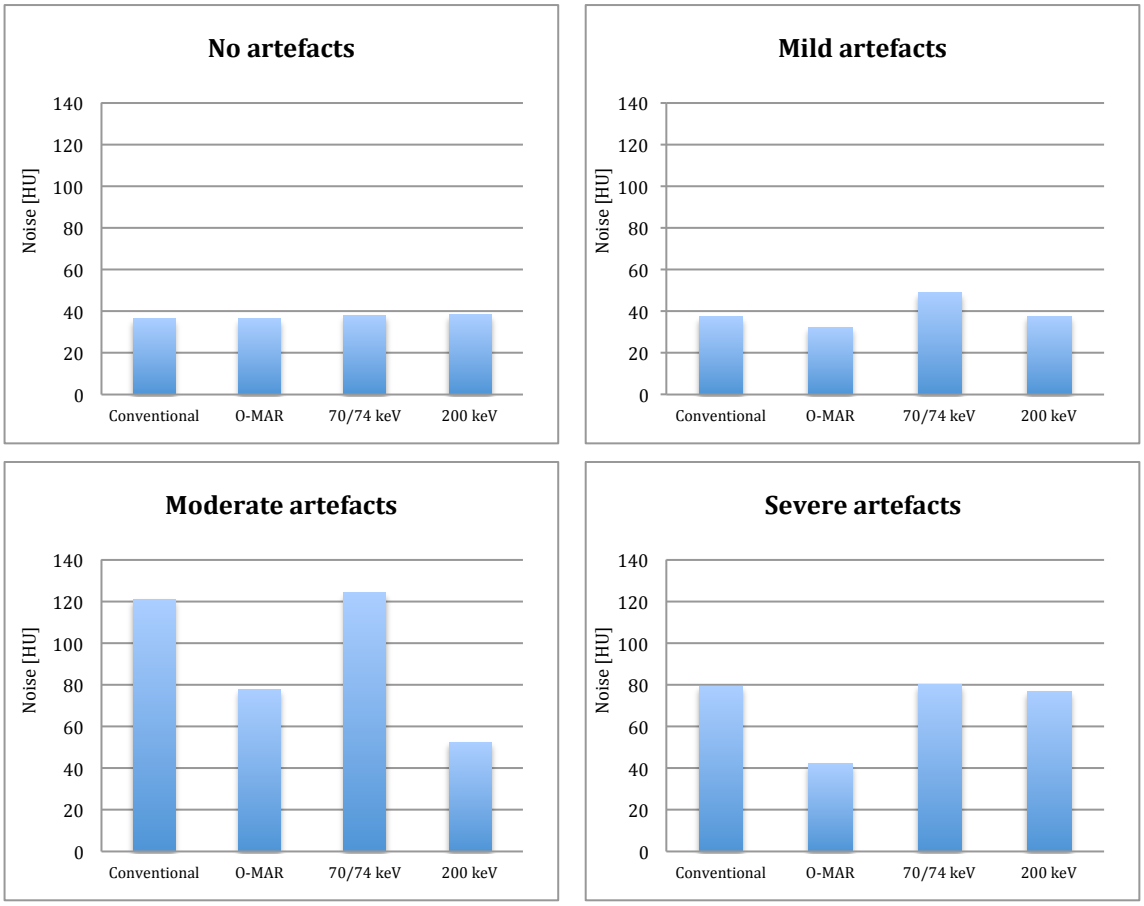

Figure 9.8: Effect of O-MAR and 200 keV imaging divided into four categories. Noise heavily increases in case of metal artefacts in the conventional and Spectral results. Both O-MAR and 200 keV results show a decrease in noise.

Noise of unaffected pellets is slightly higher for Spectral images. O-MAR images and 200 keV images show no substantial difference relative to corresponding conventional and 70 or 74 images. Noise reduction is greatest for moderate and severe artefacts regarding O-MAR. Monochromatic extrapolation reduces noise greatly for moderate artefacts. In case of severe artefacts, monochromatic imaging does not result in a substantial reduction of noise like is observed with O-MAR.

Average CNR values

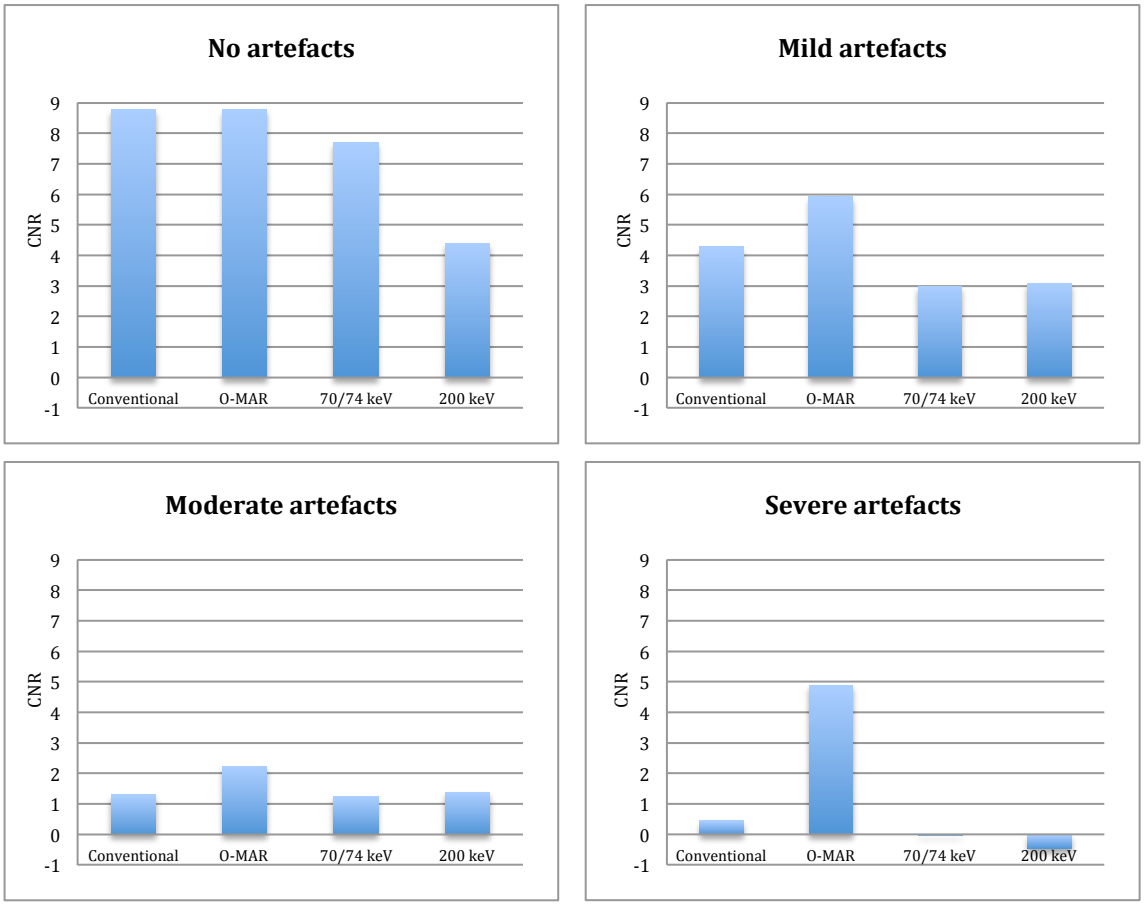

Figure 9.9: Effect of O-MAR and 200 keV imaging divided into four categories. CNR decreases with increasing rate of metal artefacts, as expected. CNR of conventional IQon images are higher in all cases. O-MAR is most effective in increasing CNRs.

CNR values of L0, L4, R0 and R4 are highest with the insertion of the prostheses. As with HU values, O-MAR does not have an effect on pellets that are unnaffected by metal artefacts. O-MAR has most effect on severe artefacts where a great increase is observed.

CNR values of all monochromatic images are lower relative to conventional and O-MAR images. Monochromatic extrapolation to 200 keV has a slightly possitive effect in case of mild and moderate artefacts. Severely distorted pellets based on HU values show very low CNR values. These CNR values are low and decrease further with increasing keV.

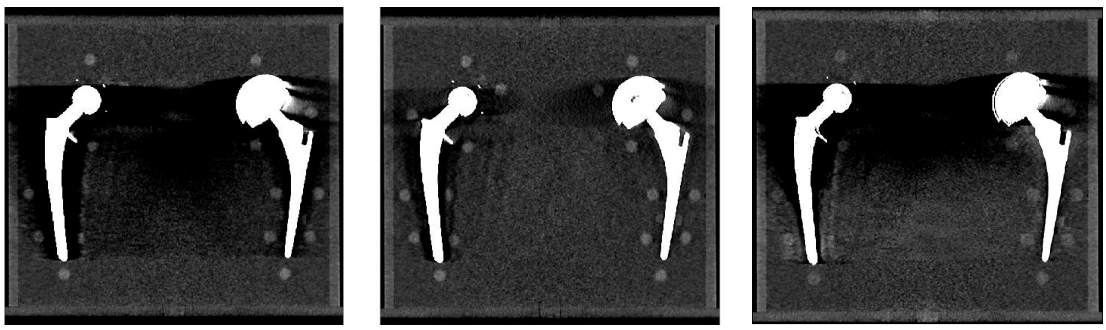

a) Conventional b) O-MAR c) Monochromatic image at 200 keV

Figure 9.10: Conventional images versus O-MAR and 200 keV imaging. O-MAR is superior in the reduction of metal artefacts as can be observed. CNRs in O-MAR images are much higher relative to 200 keV monochromatic images.

9.2.1 A quantitative analysis: high keV monochromatic CT imaging versus O-MAR in the reduction of metal artefacts in the most common unilateral hip prostheses.

A similar separation in categories can be made relative to box configuration 3. Only pellet R5 and R6 stand out due to large deviations in HU values. HU values are really low at low keV, especially relative to the conventional image. All HU of the pellets at the right side are substantially lower at the 74 keV relative to the left side, as expected. No severe artefacts can be observed based on the full spectrum analysis displayed in appendix A.

No artefacts	R0, R4 and all the left pellets
Mild artefacts	Pellet R1, R2, R3, R7 and R8
Moderate artefacts	R5 and R6
Severe artefacts	-

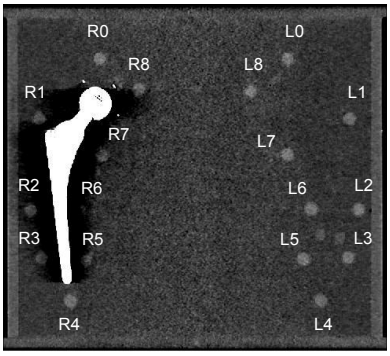

Figure 9.11: Box 6 including all 18 ROIs.

Average HU values

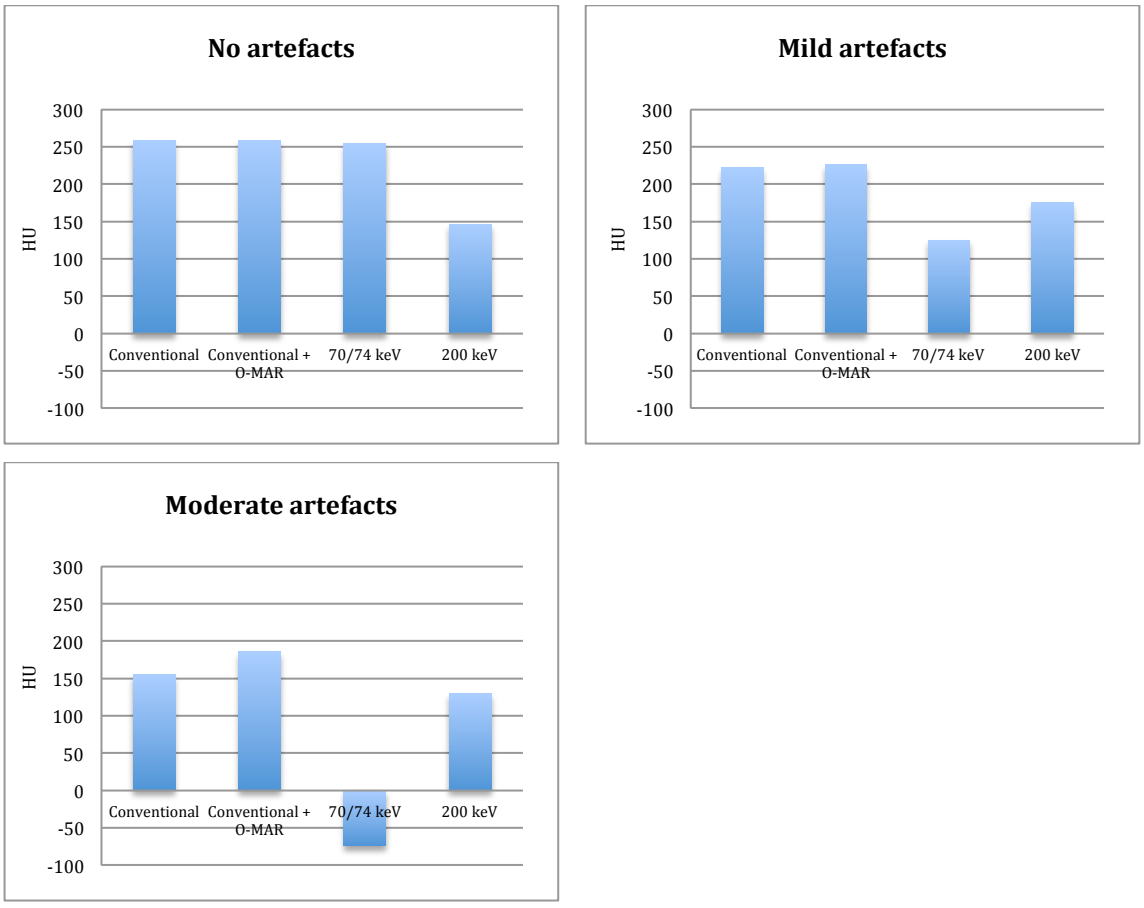

Figure 9.12: Effect of O-MAR and 200 keV imaging divided into four categories. HU values decrease with increasing rate of artefacts. HU values in the conventional images are higher in all cases. The greatest increase in HU is observed in moderate artefacts at the 200 keV monochromatic image.

Distortions of HU values using this prosthesis are smaller relative to all other prostheses. HU values do not reach negative values in each of the three dose levels for 120 and 140-kVp in case of conventional IQon images. Pellet R5 and R6 can be categorized as a moderate artefact. There are no severe artefacts present using this prosthesis configuration. Increase in HU values is greatest for pellets R5 and R6 for O-MAR and 200 keV images.

In general, distortions in the Spectral images are substantially larger based on HU values as can be observed in Figures 9.12 (a,b and c). Since O-MAR is most beneficial in case of severe artefacts, absolute improvements of O-MAR are little in case of this prosthesis configuration. Monochromatic imaging at 200 keV greatly increases HU values in case of moderate artefacts.

Average noise

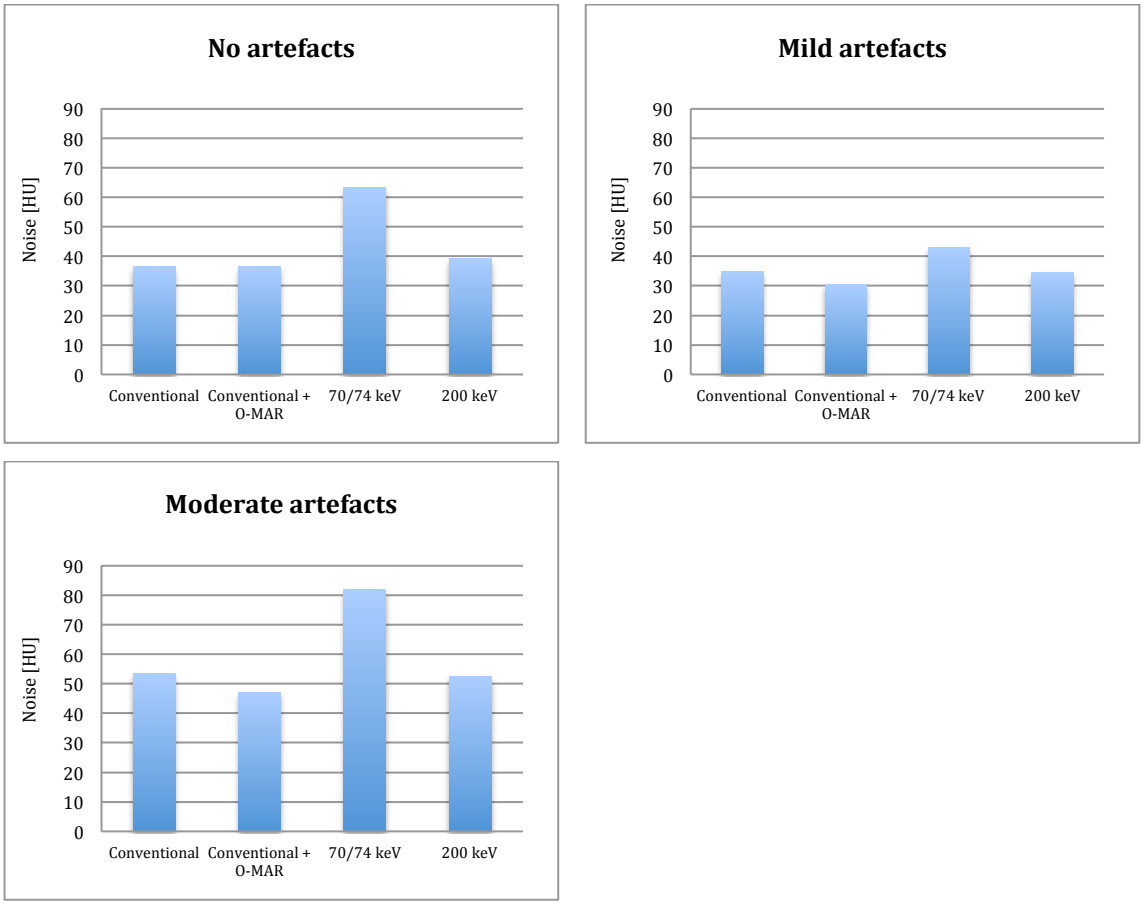

Figure 9.13: Effect of O-MAR and 200 keV imaging divided into four categories. Noise increases with an increase in artefact rate. Noise is higher in case of Spectral imaging in all cases. The greatest decrease in noise is observed in case of 200 keV monochromatic imaging.

Noise is substantially higher for Spectral results at 70 or 74 and 200 keV. As with HU distortions, O-MAR has most effect on heavier artefacts. O-MAR does show a decrease in noise in case of mild and moderate artefacts.

Noise reduction in case of monochromatic imaging at 200 keV is greatest for moderate artefacts as can be observed in Figure 9.13.

Average CNR values

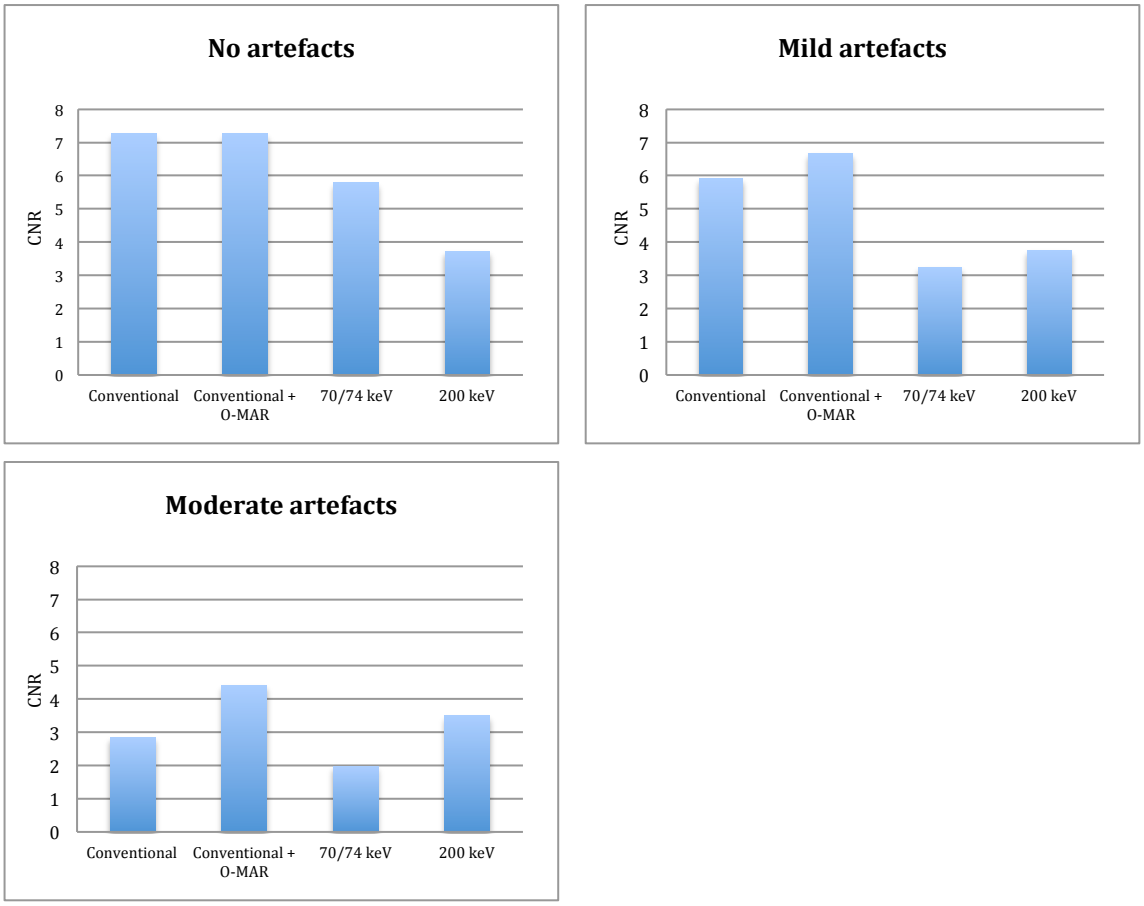

Figure 9.14: Effect of O-MAR and 200 keV imaging divided into four categories. CNRs decrease with increasing rate of metal artefact as expected. CNRs are higher for conventional and O-MAR images relative to the 70 or 74 keV and 200 keV images in all cases.

CNR values of R5 and R6 are lowest as with HU. O-MAR results in the greatest CNR improvement on these two pellets as expected but it also improves CNRs of mild artefacts.

The CNR of L0, L4, R0 and R4 decrease at higher keVs as described earlier. Only the CNR of pellet mild and moderate artefacts improve with extrapolation to higher keVs where the greatest improvement is observed in case of moderate artefacts.

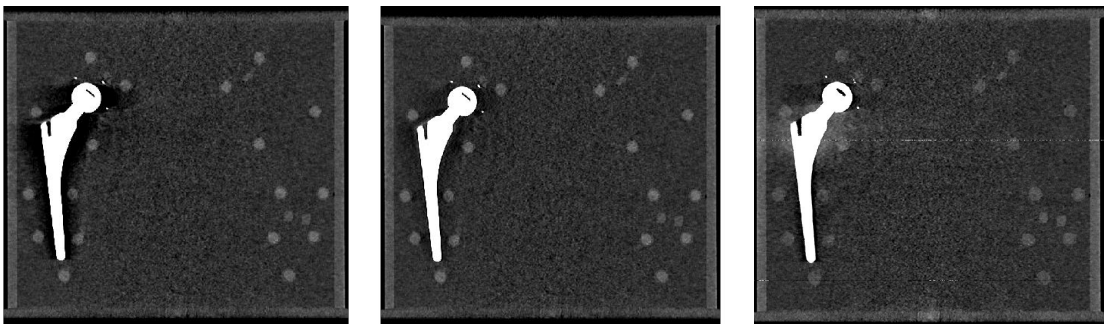

a) Conventional b) O-MAR c) Monochromatic image at 200 keV

Figure 9.15: Conventional versus O-MAR and 200 keV imaging. Also in case of this prosthesis, the use of O-MAR is superior in MAR.

Table 9.1: Absolute effect of O-MAR and 200 keV Spectral imaging on HU, noise and CNR for mild, moderate and severe artefacts.

	Artefact	Box 3 Effect by O-MAR	Box 3 Effect by Spectral	Box 6 Effect by O-MAR	Box 6 Effect by Spectral
HU	Mild	101	172	12	195
	Moderate	522	371	30	372
	Severe	665	-53	-	-
Noise [HU]	Mild	-8.18	-9.94	-5.64	-2.92
	Moderate	-45.77	-43.33	-7.11	-26.47
	Severe	-31.34	-1.37	-	-
CNR	Mild	1.63	2.98	1.10	3.64
	Moderate	1.20	3.18	1.96	4.37
	Severe	3.90	2.48	-	-

Table 9.1 shows the effects of O-MAR and 200 keV Spectral imaging on HU, noise and CNR for respectively mild, moderate and severe artefacts. When focusing on HU increase to reference values of unaffected pellets and CNR increase, O-MAR works best for severe artefacts. In case of noise decrease, O-MAR works best for moderate artefacts. The effectiveness of MAR using Spectral imaging at 200 keV is highest for moderate artefacts.

9.2.2 Effect of O-MAR and high keV monochromatic imaging at different kVp and dose-levels

In earlier parts we found that O-MAR is most effective at 140-kVp and high dose, and in case of severe artefacts. In that case the greatest HU increase, noise decrease and CNR increase is acquired. Spectral CT imaging is most effective in case of mild and moderate artefacts. The effectiveness of MAR using Spectral CT with regard to kVp and dose-levels has not been determined yet.

In order to investigate the additional value of monochromatic CT imaging at 200 keV at various kVp and dose-levels, absolute HU and CNR improvements are determined for moderate artefacts. Figure 9.16 and 9.17 show the effectiveness of O-MAR and 200 keV imaging at the IQon for pellet R6 from box configuration 3.

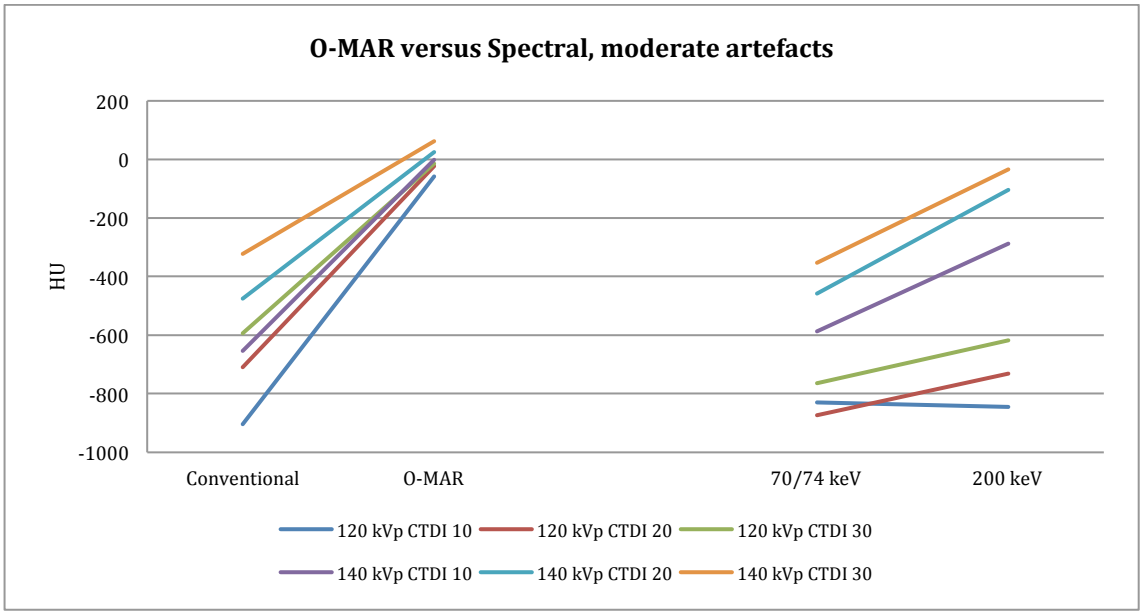

Figure 9.16: This graph shows the absolute increase in HU of O-MAR and 200 keV monochromatic imaging on HU at 120 and 140-kVp and three different $CTDI_{vol}$.

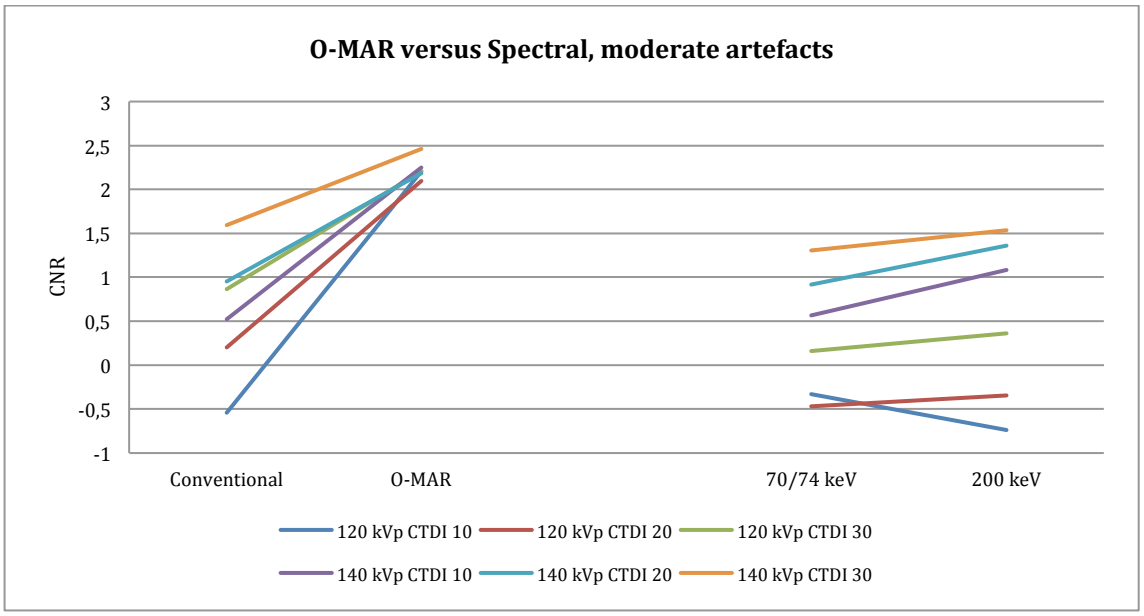

Figure 9.17: This graph shows the absolute increase in HU of O-MAR and 200 keV monochromatic imaging on CNR at 120 and 140-kVp at three different $CTDI_{vol}$.

In case of moderate artefacts concerning pellet R6, high dose imaging seems to be superior since HU and CNR are highest in case of a dose-level of 30 mGy. The average CNR of the pellets is generally higher for 140-kVp results relative to 120-kVp, in case of the Spectral results. However Spectral results at 200 keV show substantial improvement in HU and CNR values, conventional imaging with the use of O-MAR remains superior.

For the Spectral results, imaging at 120-kVp with a $CTDI_{vol}$ of 10 mGy results in the lowest HU and CNR values. Spectral extrapolation from 70 to 200 keV even results in a decrease of HU and CNR values.

9.3 Discussion

Image quality parameters are best for conventional IQon images relative to Spectral monochromatic kVp equivalent images at similar kVp and dose levels. Noise is lower ($p<0.05$) and CNRs are higher ($p<0.001$) for conventional polychromatic IQon images. CT numbers are accurate for 120 and 140-kVp at monochromatic keV of respectively 70 and 74. Metal artefacts have a greater impact in Spectral CT imaging at the kVp equivalent keV of 70 and 74 keV relative to conventional IQon images since polychromatic images also contain higher energy photons. Mean HUs are lower, noise is higher and CNRs are lower for Spectral images for mild, moderate and severe artefacts.

O-MAR is most effective in case of severe artefacts with greatest HU increase, noise decrease and CNR increase. The effectiveness of O-MAR is optimal at 140-kVp and high dose. Monochromatic images at 200 keV reduce metal artefacts significantly for mild and moderate artefacts. Spectral CT imaging itself is most effective for moderate artefacts. Despite the overall decreasing contrast when extrapolating to high keVs, mean HUs and CNRs do show an increase in case of moderate artefacts as can be seen in Figures 9.7, 9.9, 9.12 and 9.14. In case of severe artefacts, 200 keV imaging is not beneficial with regards to HU, noise and CNR of these pellets since even a further downgrade in image quality parameters is observed.

Categorisation of artefact grade took place using Spectral images based on HU, noise and CNR values at the optimal 140-kVp and standard dose, as mentioned earlier in section 8.3. The trends earlier described in the previous section were used to obtain a separation into four categories. It has to be noted that the influence of metal artefacts will be different at 120-kVp and at high and low-dose resulting in different categorizations for these acquisitions. For example, more pellets will be categorized as severe artefacts in case of 120-kVp imaging at a $CTDI_{vol}$ of 10 mGy.

Spectral MAR is more beneficial at higher dose-levels since corrections towards reference values are greater. The dose dependent effectiveness depends on the degree of artefacts. Spectral corrections are greater at 140-kVp and high dose for moderate artefacts. The effect of high monochromatic keV imaging on CNR is more optimal at 140-kVp for pellets with mild, moderate artefacts and unaffected pellets. However, an increase from 120 to 140-kVp has hardly any effect for severe artefacts. Similar studies conducted by Goodsitt et al. (2011) and Yu et al. (2012) showed a reduction in beam-hardening effect and streak artefacts using Dual-Source CT and kVp-switching CT (10,11). To our knowledge no other similar work using Dual-Layer Spectral CT imaging in the quantification of MAR has been performed yet. Unlike Raupach et al. (2010) and Bamberg et al. (2012) that found optimal monochromatic energies between 95 and 150 keV, we propose a monochromatic energy of 200 keV since CNR of affected pellets still increases till these high keVs (12,13). Imaging at such high keVs will result in images with a reduced overall contrast. Nevertheless, the use of an adjustable 'magic glass' facilitates an additional keV-window. By using this window it is possible to only visualize the relevant metal artefact regions at high keVs so it is not needed to visualize the entire image at these high keVs.

The effectiveness of O-MAR and 200 keV monochromatic imaging both depend on the kind of metal alloy and the location and distance of the pellets relative to the prostheses. The heavier cobalt-chrome-molybdenum alloy results in more severe artefacts with larger influence of photon starvation and beam-hardening. Despite Spectral CT imaging is capable of reducing the beam-hardening element, still a substantial metal artefact will

be present due to the great impact of photon starvation. The largest and most important difference between O-MAR and 200 keV monochromatic imaging is that O-MAR does not have an influence on unaffected areas. HU, noise and CNR remain constant where 200 keV monochromatic imaging leads to a great HU reduction, CNR and an overall lower contrast.

As far as we know, this is the first and only study that compared and quantified the effectiveness of O-MAR and high keV monochromatic Spectral CT imaging in the reduction of metal artefacts. Based on our findings we found that Spectral CT is capable of substantially reducing beam-hardening artefacts and streak artefacts, but only at high monochromatic energies illustrated in figure 9.2. Photon-starvation cannot be corrected for using high keV monochromatic imaging, since no metal artefact reduction is observed in case of severe artefacts. Since photon starvation is most present at low-dose and low kVp imaging, we advise 140-kVp and high dose imaging for most effective MAR when using Spectral CT. We also found that O-MAR, on the other hand, is capable of reducing the effects of photon-starvation since the most severe artefacts are substantially corrected for.

9.4 Conclusions

Virtual monochromatic images can provide acceptable image quality to conventional 120 and 140-kVp images at similar $CTDI_{vol}$. However, noise is lower and CNRs are higher for conventional polychromatic IQon results. Metal artefacts have a greater impact on the kVp equivalent monochromatic resulting in greater HU, noise and CNR deviations relative to baseline values compared to polychromatic results. Virtual monochromatic imaging has the potential to reduce beam-hardening and streak-artefacts. Virtual high-keV monochromatic imaging itself is most effective in case of moderate artefacts. O-MAR is superior in MAR since absolute corrections towards reference HU, noise and CNR values are greater the most severe artefacts. Additionally, O-MAR has no effect on HU, noise and CNR in the absence metal artefacts where 200 keV monochromatic imaging results in a loss in contrast and consequently in CNRs in unaffected regions. Virtual high-keV monochromatic imaging can only correct for beam-hardening and streak artefacts and not for metal artefacts caused by photon-starvation, unlike O-MAR.

Quantifying minimal acceptable dose-levels in the CT-imaging of a metal hip prosthesis using recent innovative CT-techniques IMR, O-MAR and high keV monochromatic Spectral CT-imaging.

Purpose: To quantify the value of the IMR, O-MAR and high keV monochromatic imaging in the CT-imaging of a metal hip prosthesis focusing on image quality parameters at 80% dose reduction. We wanted to quantify CT number accuracy at ultra-low dose and which combination of innovative CT-techniques is superior in the ultra-low dose imaging of the most commonly used hip prosthesis.

Methods and Materials: A water-filled phantom was used made of PMMA using the most commonly used hip prosthesis configuration used at Isala surrounded by 18 hydroxyapatite pellets representing bone. Scans were acquired on a 128-slice IQon scanner and a 256-slice iCT scanner from high to ultra-low-dose (CTDI's: 40, 32, 24, 16, 8 and 4 mGy) at 120 and 140-kVp. Conventional iCT images were reconstructed using FBP, iterative reconstruction (IR, iDose^4 level 2, 4 and 6) and model-based iterative reconstruction (IMR, level 1,2 and 3) with and without the use of O-MAR. Polychromatic and monochromatic images were reconstructed with FBP and iterative reconstruction (IR, iDose^4 level 2, 4 and 6). Polychromatic results were reconstructed with and without the use of O-MAR where monochromatic images were analyzed at monochromatic energies 70 or 74 keV and 200 keV. Mean Hounsfield Unit, noise [HU] and CNR of all pellets with and without the insertion of several prostheses were calculated and analyzed using a standardized measurement template.

Results: IMR is capable of maintaining acceptable noise levels even at ultra-low dose. Mean HUs and CNRs of unaffected pellets remain acceptable at a dose of 4 mGy in all iCT acquisitions. Fluctuations in mean HUs and CNRs from high to low dose imaging are greater on IQon acquisitions, especially for monochromatic results. At the ultra low dose of 4 mGy IMR level 1, 2 and 3 show respectively 83%, 89% and 95% lower values in noise relative to standard FBP reconstructions while maintaining acceptable HU values. In case of imaging metal prosthesis, iCT acquisitions are least sensitive to metal artefacts based on deviations in HU, noise and CNR values relative to IQon acquisitions. Subsequently, monochromatic imaging is most sensitive to metal artefacts at equivalent effective energies.

Conclusions: In current clinical practice at Isala Clinics Zwolle, an average $CTDI_{vol}$ of 20 mGy in radiation dose is used. Thus, based on the analysed HU, noise and CNR results of this phantom study, we can conclude that with the use of IMR and O-MAR acceptable image quality parameters are maintained at a reduction in radiation dose of 80 % relative to standard reconstructions techniques in the CT-imaging of metal hip prostheses. However, an extensive clinical study is essential, since the actual possibilities in dose-reduction cannot be determined based on this phantom study only.

10 Results of Part 5:
State of the art imaging techniques at ultra-low-dose

In the final part of this research a comparison is made of all state-of-the-art techniques used within this study. All CT techniques are pushed to their limits where image quality parameters are determined from high to ultra-low-dose using the most commonly used prosthesis.

Scans are obtained on the iCT and IQon scanner at 120 and 140-kVp. Tube currents were chosen in order to obtain $CTDI_{vol}$ of 40, 32, 24, 16, 8 and 4 mGy for both tube voltages. iCT acquisitions were reconstructed with FBP, iDose^4 levels 2, 4 and 6 and IMR levels 1, 2 and 3. Conventional scans on the IQon were reconstructed with FBP and iDose^4 levels 2, 4 and 6 since IMR reconstructions are not available on this newest system yet. All iCT and conventional IQon reconstructions are reconstructed with and without the use of the orthopaedic metal artefact algorithm O-MAR. Spectral results were reconstructed with FBP and iDose^4 levels 2, 4 and 6 and analysed at the kVp equivalent keVs of 70 or 74 keV and 200 keV.

Image quality parameters are measured at each different dose-level using different acquisitions and reconstruction techniques. For each combination of technique the minimal acceptable dose level is investigated based on clinical acceptable HU, noise and CNR values.

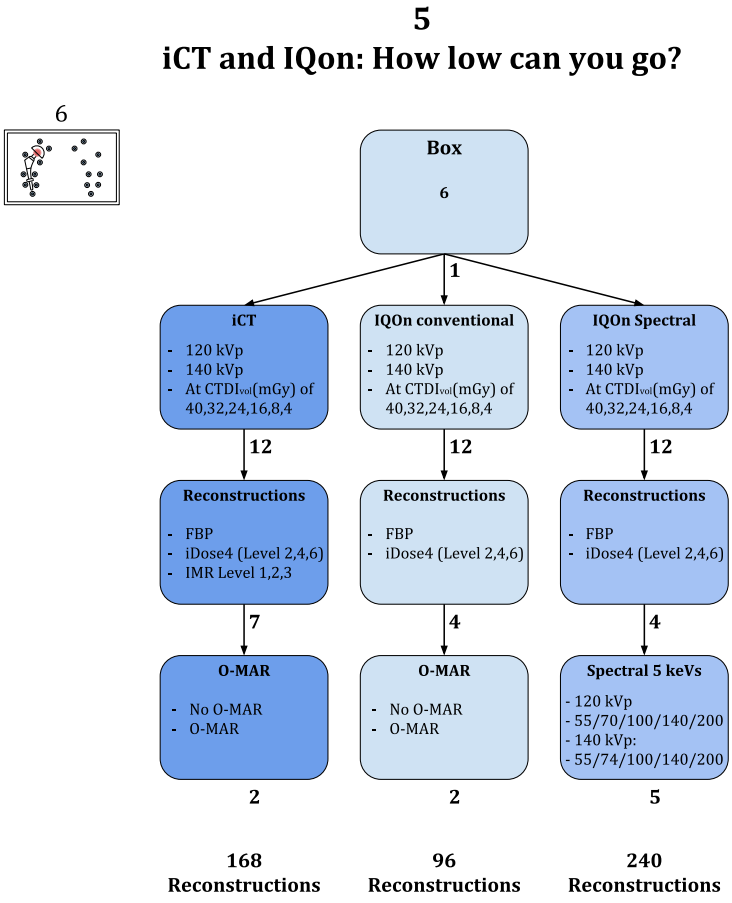

Figure 10.1: Overview of part 5.

10.1 The influence of ultra-low-dose scanning on HU and CNR

To investigate the possibilities in dose reduction using the described innovative CT-techniques, acceptable image quality parameters need to be stated. HU values of unaffected pellets need to remain reliable and constant at all dose-levels. The influence of dose-reduction on mean HU stability is therefore investigated.

10.1.1 Average HU of unaffected pellets at ultra-low-dose

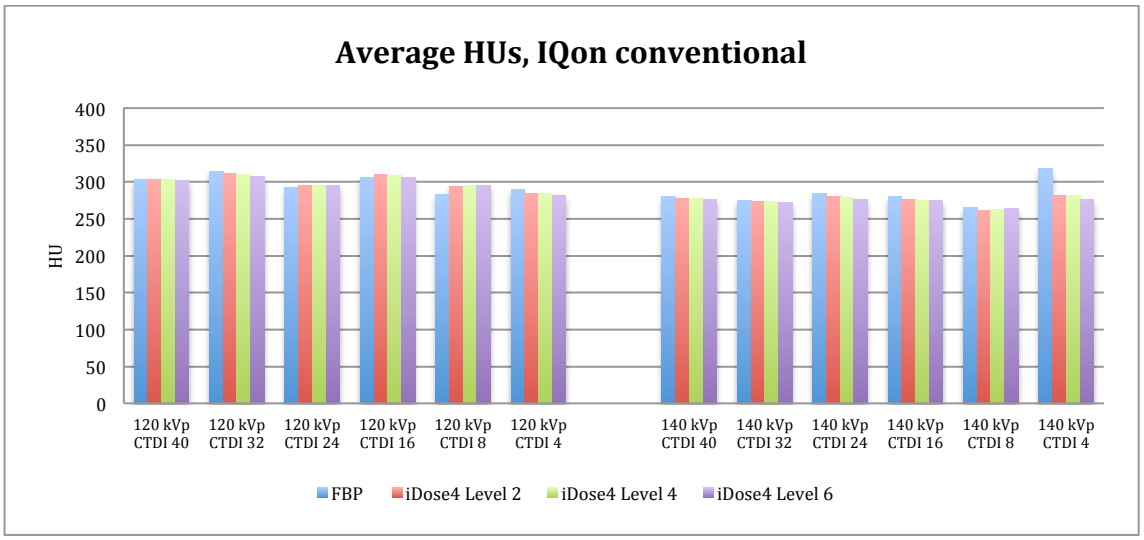

Figure 10.2: Average HU values in conventional IQon images for FBP and iDose4 (levels 2, 4 and 6) at dose-levels of 40, 32, 24, 16, 8 and 4 mGy.

When observing HU values in the 120-kVp conventional IQon images we see a slight overall decreasing trend. 140-kVp results show stable HU values from high to low-dose. HU values are slightly higher for 120-kVp results relative to 140-kVp results for all $CTDI_{vol}$.

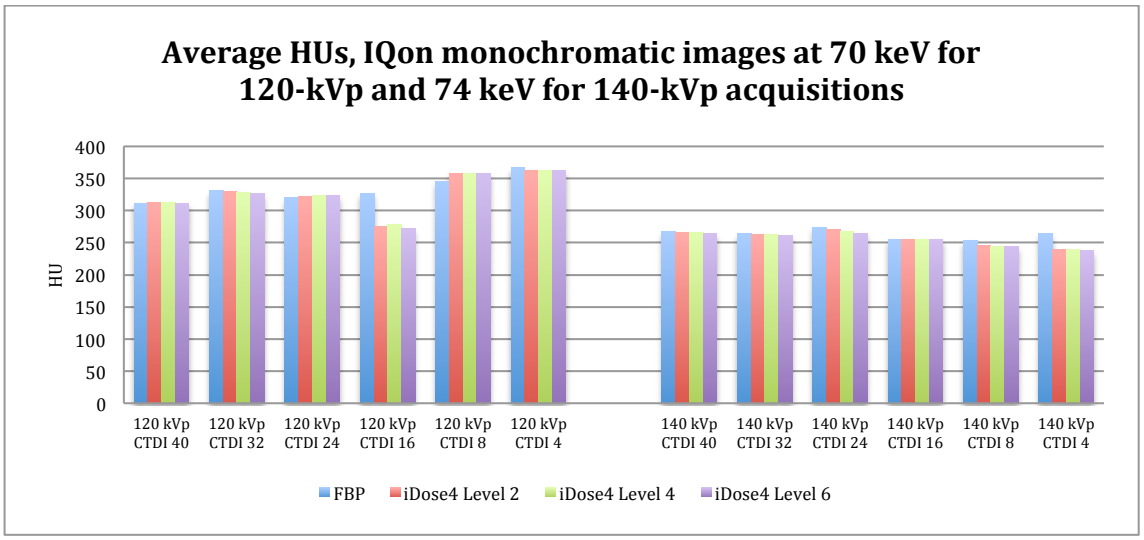

Figure 10.3: Average HUs in 70 or 74 keV monochromatic images for FBP and iDose4 (levels 2, 4 and 6) at dose-levels of 40, 32, 24, 16, 8 and 4 mGy.

Large fluctuations in HU values are observed for 70 keV monochromatic images between high and low-dose images. Mean HUs are stable for 140-kVp results. Greatest fluctuations in mean HUs are observed for 120-kVp results where low-dose images with a $CTDI_{vol}$ of 8 and 4 mGy show HU values greater than 350 HU.

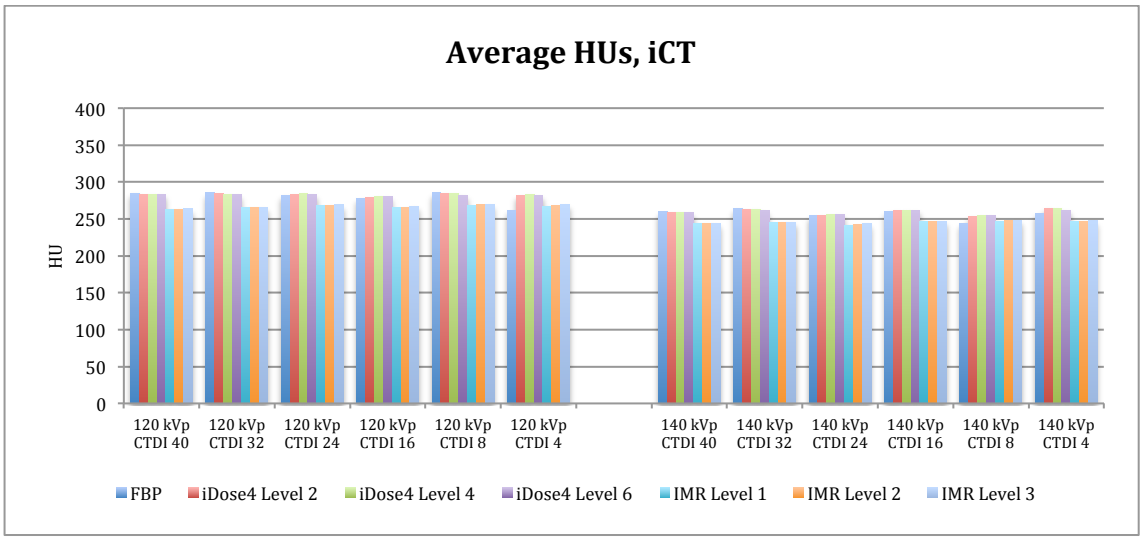

Figure 10.4: Average HUs for iCT images for FBP, iDose4 (levels 2, 4 and 6) and IMR (levels 1, 2 and 3) at dose-levels of 40, 32, 24, 16, 8 and 4 mGy.

HU values are significantly lower for IMR reconstructions relative to FBP and iDose^4 reconstructions as observed earlier in part 2. HU values remain extremely stable for 120 and 140-kVp results from 40 till 4 mGy.

10.1.2 Average CNR of unaffected pellets at ultra-low-dose

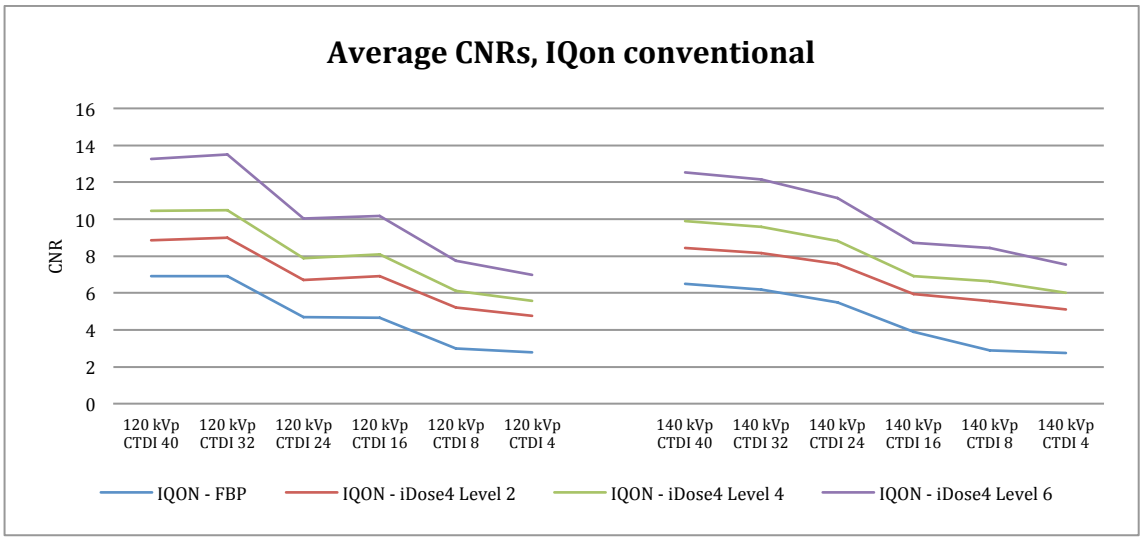

Figure 10.5: Average CNRs in conventional IQon images for FBP and iDose4 (levels 2, 4 and 6) at dose-levels of 40, 32, 24, 16, 8 and 4 mGy.

CNRs are clearly higher for all iDose^4 levels relative to FBP reconstructions as expected. The increasing CNRs for iDose^4 levels 2, 4 and 6 are also greatly shown. When decreasing tube currents a decrease in CNR is observed.

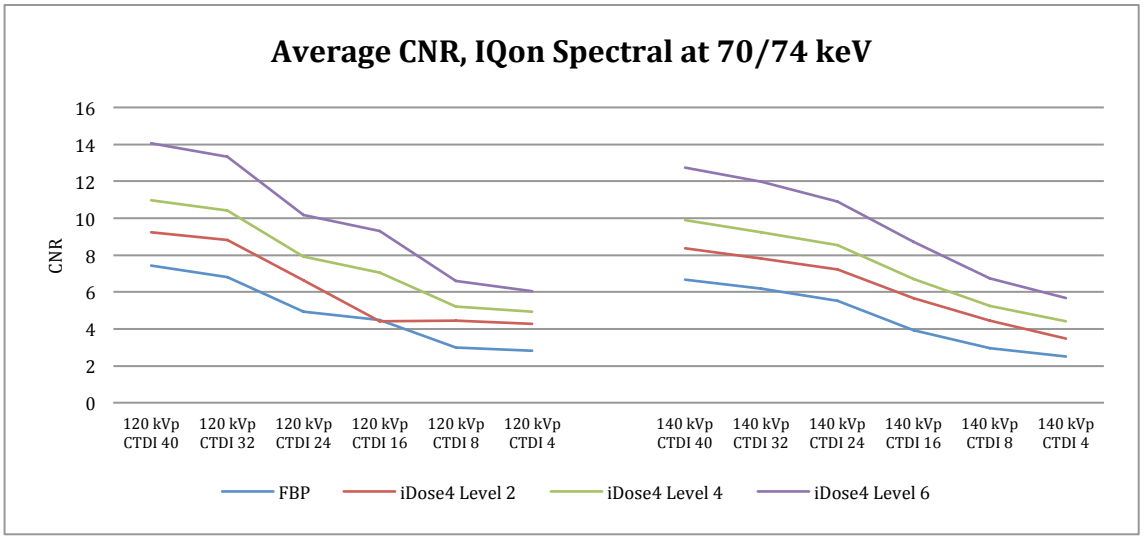

Figure 10.6: Average CNRs in 70 or 74 keV monochromatic images for FBP and iDose4 (levels 2, 4 and 6) at dose-levels of 40, 32, 24, 16 8 and 4 mGy.

The same trends as for conventional CNRs are observed for 70 and 74 keV monochromatic images where CNRs of iDose^4 are superior to those resulting from FBP reconstructions. It can be observed that CNRs at high dose are similar to conventional CNRs at high dose-levels.

When analysing low-dose results, CNR in conventional images are superior relative to the kVp equivalent images at 70 and 74 keV. Therefore dose-reduction possibilities seem to be superior in case of conventional polychromatic CT images based on CNRs.

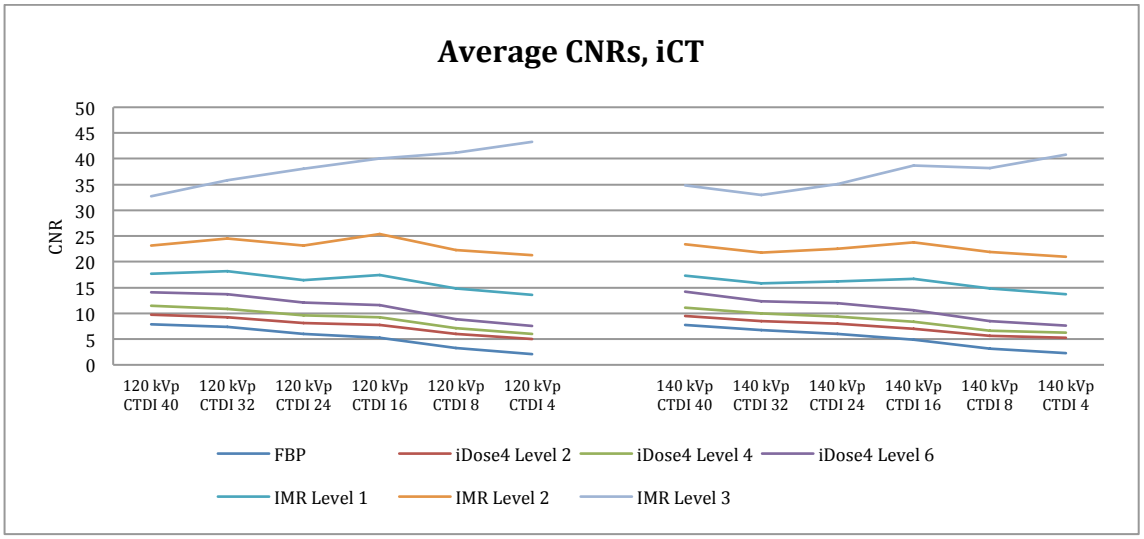

Figure 10.7: Average CNRs in iCT images for FBP, iDose4 (levels 2, 4 and 6) and IMR (levels 1, 2 and 3) at dose-levels of 40, 32, 24, 16, 8 and 4 mGy.

CNRs in conventional iCT images are higher for FBP and iDose^4 (levels 2, 4 and 6) relative to conventional IQon images and monochromatic IQon images at the keV of 70 or 74. Decreasing trends for FBP, iDose^4 (levels 2, 4 and 6) are observed when decreasing radiation dose from 40 to 4 mGy.

Also in case of CNRs obtained unaffected pellets in images reconstructed with IMR level 1, a decreasing trend in CNR is observed when decreasing radiation dose. In case of IMR level 2 results, a constant CNR level is maintained till approximately 16 mGy as can be observed in Figure 10.7. CNRs at 8 and 4 mGy are slightly lower. CNR trends in IMR level 3 reconstructions differ from all other earlier observed CNR trends when decreasing radiation dose. An increase in CNR is observed when decreasing radiation dose where CNRs of over 40 are reached. At both 120 and 140 kVp, this increasing CNR trend is observed.

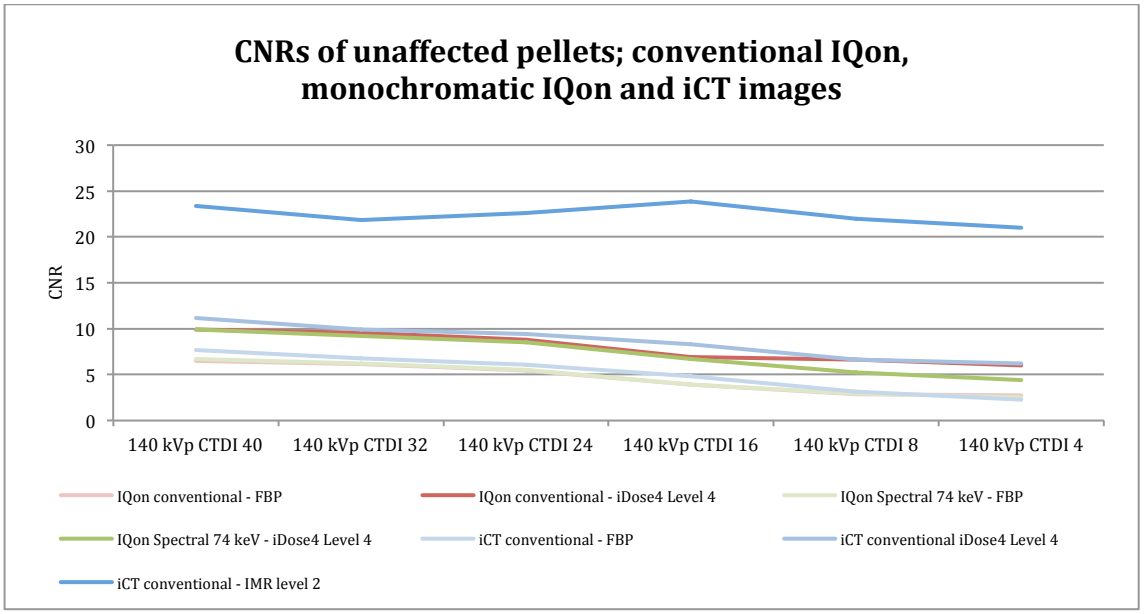

Figure 10.8: Average CNRs of unaffected pellets. Results are shown for conventional IQon acquisitions, monochromatic IQon acquisitions at 74 keV and conventional iCT acquisitions at 140 kVp.

Figure 10.8 illustrates the average CNRs of unaffected pellets for conventional IQon acuisitions, monochromatic IQon acquisitions at 74 keV and conventional iCT acquisitions at 140 kVp. CNRs of unaffected pellets in iCT images reconstructed with IMR level 2 are clearly higher.

Based on the results shown in Figure 10.7 and 10.8, a more detailed analysis in noise is required. When focusing on FBP and iDose^4 reconstruction techniques, we see an increase in noise when lowering the radiation dose, as expected. Only in case of IMR, only a slight increase in noise is observed where IMR level 3 reconstructions shows an almost steady course from high to low-dose.

Differences in noise between the different reconstruction techniques are strongly dependent on radiation dose. Initially at 140-kVp and 40 mGy, noise for IMR level 1, 2 and 3 is respectively 60%, 72% and 84 % lower relative to FBP where at 4 mGy noise is 83%, 89% and 95 % lower relative to FBP for respectively IMR level 1, 2 and 3.

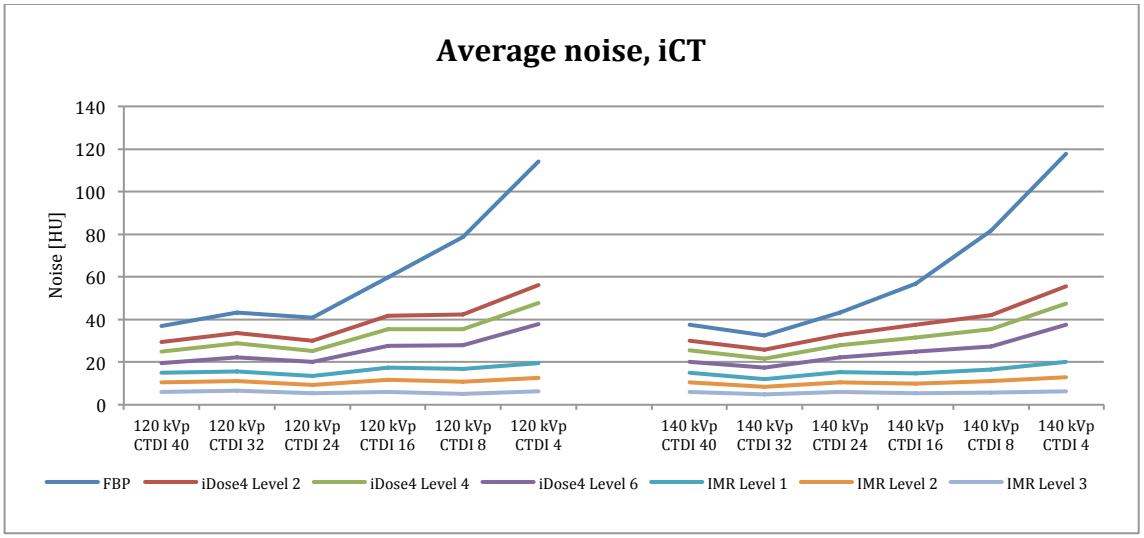

Figure 10.9: Average noise in iCT images reconstructed with FBP, iDose4 (levels 2, 4 and 6) and IMR (levels 1, 2 and 3).

10.2 HU values of the most affected pellets using all optimal combination of techniques

As stated earlier, monochromatic IQon images at 70 or 74 keV show greater HU deviations in case of the most affected pellet R6 relative to conventional polychromatic IQon images at 120 and 140-kVp. Additionally, conventional IQon images show greater HU deviations in case of the most affected pellet R6 relative to conventional iCT images at 120 and 140-kVp. It can therefore be concluded that the rate or impact of metal artefacts increases for respectively conventional iCT, conventional IQon and monochromatic IQon images.

Figure 10.10 shows the HUs of pellet R6 using the three techniques with additional MAR approaches and optimal reconstruction techniques from high to low-dose at 140-kVp. At a $CTDI_{vol}$ of 4 mGy HUs of pellet R6 are clearly lower for optimal conventional O-MAR IQon images and 200 keV results, relative to optimal conventional iCT O-MAR results.

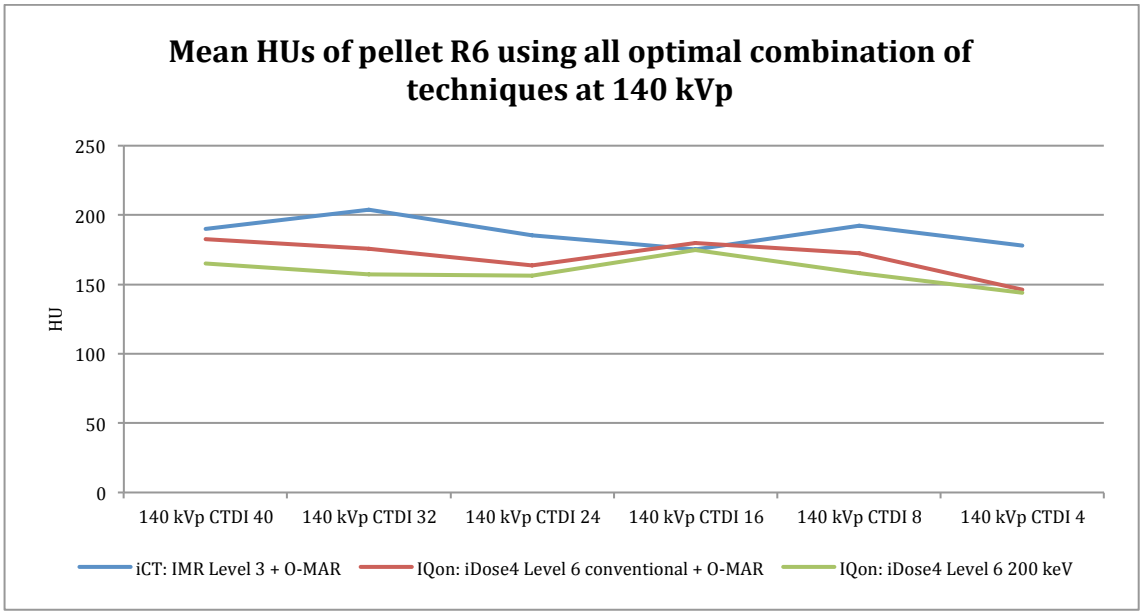

Figure 10.10: HU values of the most affected pellet using all optimal combinations of CT-techniques from high to ultra-low-dose.

Graphs of HUs of R6 from iCT and IQon images with and without the use of O-MAR and monochromatic IQon images at 70 or 74 and 200 keV for 120 and 140-kVp and for all dose levels are shown in appendix B.

10.3 CNR values of the most affected pellet using all optimal combination of techniques

Tables 10.1, 10.2, and 10.3 show the CNR of the most affected pellet R6. Table 10.1 shows the CNR of iCT acquisitions with and without the use of O-MAR for FBP, iDose^4 (levels 2, 4 and 6) and IMR (levels 1, 2 and 3) reconstructions. Table 10.2 shows the CNR of conventional IQon acquisitions with and without the use of O-MAR for FBP and iDose^4 (levels 2, 4 and 6) reconstructions. Table 10.3 shows the CNR of monochromatic IQon images at 70 of 74 keV and 200 keV for FBP and iDose^4 (levels 2, 4 and 6) reconstructions.

Table 10.1: Average CNR values of pellet R6 in iCT images with and without the use of O-MAR.

mGy	FBP		iDose^4 Level 2		iDose^4 Level 4		iDose^4 Level 6		IMR Level 1		IMR Level 2		IMR Level 3	
	Con	MAR	Con	MAR	Con	MAR	Con	MAR	Con	MAR	Con	MAR	Con	MAR
40	3.98	4.93	4.44	6.12	4.61	6.79	4.90	7.75	7.22	9.76	7.74	11.85	8.13	14.73
32	3.96	4.79	4.42	6.05	4.61	6.68	4.86	7.62	6.84	11.42	7.15	13.82	7.22	15.97
24	3.02	3.28	3.89	5.79	4.05	6.58	4.31	7.59	6.09	9.92	6.29	13.00	6.52	17.73
16	3.21	3.50	3.77	5.16	3.98	5.92	4.31	7.04	5.95	9.89	6.24	13.51	6.52	19.23
8	2.53	2.38	3.46	5.04	3.57	5.64	3.80	6.57	4.72	9.81	5.01	13.79	5.27	20.30
4	2.07	1.87	2.87	4.53	2.89	5.09	3.01	5.92	3.32	10.21	3.39	14.06	3.44	19.84

Table 10.2: Average CNR values of pellet R6 in conventional IQon images with and without the use of O-MAR.

mGy	FBP		iDose^4 Level 2		iDose^4 Level 4		iDose^4 Level 6	
	Con	MAR	Con	MAR	Con	MAR	Con	MAR
40	3.13	3.67	3.40	5.00	3.47	5.54	3.71	6.31
32	2.45	2.38	2.94	3.99	3.13	4.56	3.36	5.39
24	2.44	2.82	2.73	4.70	2.88	5.32	3.10	6.28
16	2.68	2.86	2.95	4.62	3.02	5.16	3.15	5.97
8	2.31	2.19	2.90	4.39	2.90	4.93	2.93	5.64
4	3.47	3.22	2.43	4.26	2.41	4.78	2.39	5.30

Table 10.3: Average CNR values of pellet R6 in monochromatic images at 70 or 74 and 200 keV.

mGy	FBP		iDose^4 Level 2		iDose^4 Level 4		iDose^4 Level 6	
	74 keV	200 keV	74 keV	200 keV	74 keV	200 keV	74 keV	200 keV
40	2.94	3.10	3.07	4.04	3.18	4.47	3.31	5.13
32	2.38	1.45	2.58	2.16	2.66	2.40	2.80	2.78
24	2.50	2.17	2.52	3.29	2.62	3.95	2.77	4.98
16	2.70	1.97	2.76	3.27	2.82	3.84	2.87	4.57
8	2.11	1.16	2.59	2.56	2.59	2.99	2.59	3.64
4	3.08	2.79	2.35	2.82	2.33	3.19	2.31	3.67

Clear differences are observed in CNRs of pellet R6 using the iCT, conventional IQon and monochromatic IQon images. In general, CNRs on conventional iCT acquisitions are higher relative to conventional IQon acquisitions. Subsequently, CNRs on conventional IQon acquisitions are higher than for monochromatic IQon acquisitions. These differences are observed with and without the use of MAR approaches.

CNRs in images obtained on the iCT and reconstructed with IMR are substantially higher for all IMR levels relative to CNRs obtained in conventional and monochromatic IQon images reconstructed with FBP and iDose^4 levels 2, 4 and 6. Graphs of CNRs of R6 from iCT and IQon images with and without the use of O-MAR and monochromatic IQon images at 70 or 74 and 200 keV at 120 and 140-kVp and for all dose levels are displayed in appendix B.

Figure 10.11 shows the CNRs of pellet R6 using the three techniques with additional MAR approaches and optimal reconstruction techniques from high to low-dose at 140-kVp. At a $CTDI_{vol}$ of 4 mGy CNRs of pellet R6 of 3.67, 5.30 and 19.84 are reached for respectively optimal IQon 200 keV results, optimal conventional IQon O-MAR results and optimal conventional iCT O-MAR results.

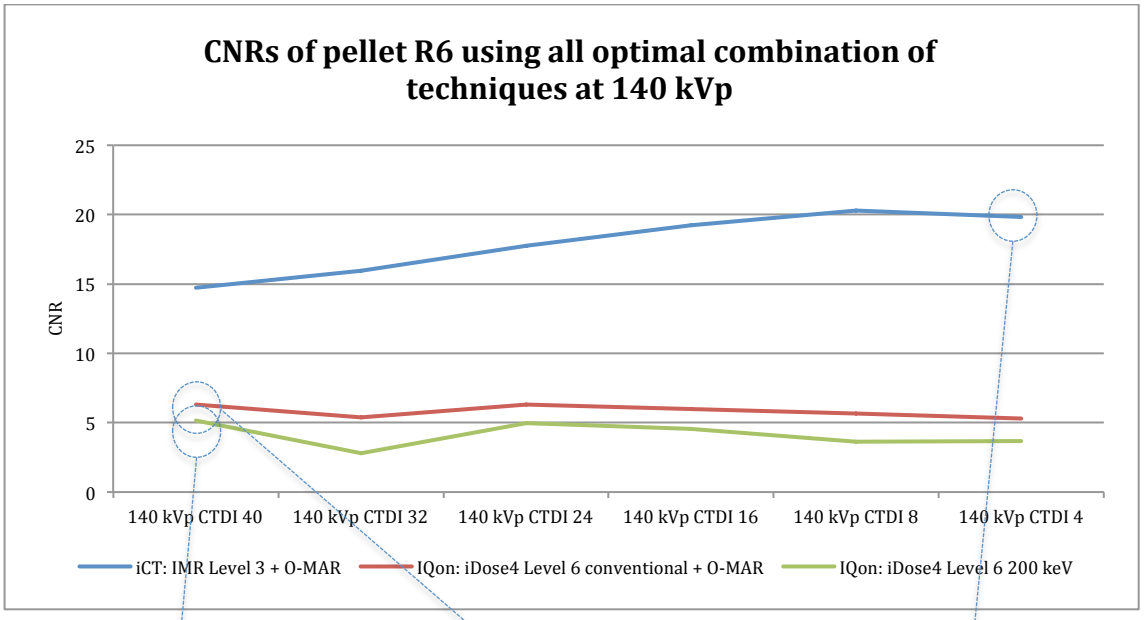

Figure 10.11: CNR values of the most affected pellet using all optimal combinations of CT-techniques from high to ultra-low-dose.

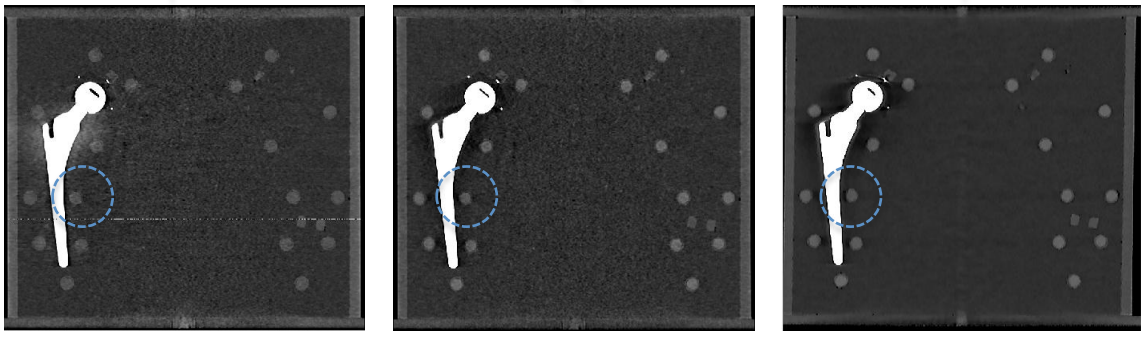

a) b) c)

Figure 10.12: Images at 140 kVp at a dose level of c) 40 mGy (monochromatic IQon results), b) 40 mGy (conventional IQon results) and c) 4 mGy (iCT results) using all techniques in an optimal setting.

10.4 Discussion

Finally, we investigated the capabilities of the earlier introduced techniques in the CT imaging of the most commonly used metal hip prosthesis up to a dose reduction of 80% relative to current clinical practice. The value of IMR, O-MAR and high keV monochromatic imaging is quantified at 120 and 140 kVp and $CTDI_{vol}$ dose-levels of 40, 32, 24, 16, 8 and 4 mGy. A $CTDI_{vol}$ of approximately 20 mGy is used in current clinical practice at Isala Clinics Zwolle.

CT number accuracy is an essential element within this study since we focus on the quantitative additional value of innovative technique. We observed constant mean HU values of unaffected pellets at 120 and 140-kVp for all dose-levels on conventional iCT acquisitions using FBP, iDose^4 (levels 2, 4 and 6) and IMR (levels 1, 2 and 3). In similar conventional IQon acquisitions we observed constant HU values for high and normal dose-levels, where at lower dose HU deviations are greater, illustrated in Figure 10.2. Mean HU values of monochromatic images are higher in case of 120-kVp results compared to 140-kVp results. Virtual monochromatic imaging is most sensitive to dose-reductions based on HU accuracy with varying mean HUs between 280-360 HU in the 120-kVp results when decreasing radiation dose from 40 to 4 mGy, illustrated in Figure 10.3.

CNRs of unaffected pellets decrease in iCT, conventional IQon and monochromatic IQon results for FBP and iDose^4 reconstructions when reducing radiation dose. CNRs are generally highest for iCT acquisitions and conventional IQon acquisitions show higher CNRs than monochromatic acquisitions. CNRs in images reconstructed with IMR are substantially higher relative to FBP and iDose^4 reconstructions.

CNR trends in images reconstructed with IMR stand out. With IMR level 1, CNRs decrease with decreasing radiation dose. IMR level 2 reconstructions results in relatively constant CNR values over the entire dose-level spectrum from 40 to 4 mGy. In case of IMR level 3, an unexpected trend is observed since a decrease in radiation dose leads to an increase in CNR with a maximum of 40. A possible explanation for the observed IMR trends illustrated in Figure 10.9 can be its effectiveness in noise suppression. IMR can be used in three different levels of noise reduction where level 3 applies the greatest noise reduction. Since noise increases linearly with decreasing radiation dose, noise is highest at a $CTDI_{vol}$ of 4 mGy. IMR level 3 is best capable of dealing with noise levels resulting in virtually noise-free images. A side effect of this magnitude of noise suppression in low-dose images is the increasing smoothening effects. Another possible side effect of noise suppression is the poor spatial resolution, an image quality parameter we did not investigated. However Löve et al. found that IMR clearly improves spatial resolution while at the same time greatly reducing noise (38).

The magnitude of artefacts in case of this prosthesis is substantially lower relative to other prosthetic composites used in the other studies. However, when imaging at 120-kVp artefacts become much more apparent relative to 140-kVp, especially at low-dose. As observed in previous parts, IQon acquisitions are more sensitive to metal artefacts relative to iCT acquisitions since deviations in mean HUs, noise and CNRs are greater relative to baseline values. Especially kVp equivalent monochromatic images show great distortions, which are most pronounced at 120-kVp and low-dose as expected. This can clearly be observed in Tables 10.1-3, Figure 10.11 and the Figures 14.24-14.35 in appendix B. Based on previous results, O-MAR has shown to be most effective in MAR resulting in the greatest corrections of HU, noise and CNR towards baseline values. O-MAR is superior in MAR at both 120 and 140-kVp and all dose-levels.

Based on the analysed HU and CNR values at 40, 32, 24, 16, 8 and 4 mGy we conclude that ultra-low-dose imaging at 4 mGy still results in acceptable image quality parameters using iCT acquisitions with IMR reconstructions and O-MAR. Also in case of the most affected pellet R6 reconstructed with IMR reconstructions and O-MAR results in acceptable images at a $CTDI_{vol}$ of 4 mGy relative to both polychromatic and monochromatic IQon results at 40 mGy illustrated in Figure 10.11.

Previous work focused on the additional value of MBIR relative to standard reconstruction techniques showed promising results. Several recent studies showed that model-based iterative reconstruction techniques are able to reduce image noise up to 75%-88% and radiation dose up to 75%-92% (5,18–21). At the ultra-low-dose of 4 mGy using IMR level 1, 2 and 3 we found respectively 83%, 89% and 95% lower values in noise relative to standard FBP reconstructions. When observing 120 and 140-kVp results for all dose-levels, IMR reconstructions result in at least 60% noise reduction and 47% CNR improvement in case of IMR level 1, and up to 83% noise reduction and 73% CNR improvement in case of IMR level 3 relative to FBP reconstructions.

10.5 Conclusions

IMR is capable of maintaining acceptable noise levels and CNRs even at a dose reduction of 80% relative to current clinical practice. HU and CNR values of unaffected pellets remain acceptable even at a dose of 4 mGy in all iCT acquisitions. Impact on HU accuracy and CNR at low-dose imaging is greater on IQon acquisitions, especially for monochromatic results. At the ultra-low-dose of 4 mGy IMR level 1, 2 and 3 show respectively 83%, 89% and 95% lower values in noise relative to standard FBP reconstructions while maintaining acceptable HU values. In case of imaging metal prosthesis, iCT acquisitions are least sensitive to metal artefacts based on deviations in HU, noise and CNR values relative to IQon acquisitions. Subsequently, monochromatic imaging is most sensitive to metal artefacts. In current clinical practice at Isala Clinics Zwolle, an average $CTDI_{vol}$ of 20 mGy in radiation dose is used. Thus, based on the analysed HU, noise and CNR results of this phantom study, we can conclude that with the use of IMR level 1,2 or 3 and O-MAR acceptable image quality parameters are maintained at a reduction in radiation dose of 80% relative to current clinical practice in the CT-imaging of metal hip prostheses. However, an extensive clinical study is essential, since the actual capabilities in dose-reduction cannot be determined based on this phantom study only.

11 Overall conclusions

In general, the degree of metallic artefacts strongly depends on the thickness, size and density of the prosthesis and CT parameters including tube voltage and tube current. Differences in degree of metal artefacts and capabilities in metal artefact reduction are observed using different scanners, reconstruction techniques and MAR approaches of Philips. In this research project we have been able to address a comparison between polychromatic iCT imaging, polychromatic IQon imaging and monochromatic Spectral IQon imaging. It was not possible to determine the value of combining all state-of-the-art techniques in MAR since IMR and O-MAR cannot be used in combination with monochromatic Spectral CT yet. Thus we have been able to evaluate the intrinsic beneficial effect of Spectral CT in the reduction of metal artefacts. We defined metal artefacts as a distortion on (unaffected) mean HUs, noise and CNRs. To quantify the degree of metal artefacts and the value of O-MAR, IMR and monochromatic Spectral CT-imaging mean HUs, noise and CNR values of ROIs located in and around the hydroxyapatite pellets are analysed.

A strong aspect of the used quantitative phantom analyses is the reliability and reproducibility. To enhance the reliability in scan acquisitions and in order to use the same measurement template for all acquisitions we ensured no possible movement of the phantom during all acquisitions. All scans were acquired consecutively at the iCT and IQon CT-scanners where the same surview was used for each scan. By adding custom made PMMA holders, the different prosthetic configurations were correctly aligned in all acquisitions. The phantom design itself is unique relative to other solid phantoms used for quantitative analyses. This phantom can be filled with water and different prosthetic composites, shapes and sizes can be inserted. Also inserting other phantoms like a prostate phantom or small soft tissue phantoms can be done easily. The reliability and reproducibility of the analysis is strongly enhanced by the use of a standardized measurement template used for all image analyses, illustrated in Figure 5.6. The amount of pixels and size of the ROIs is optimized to avoid influence of the partial volume effect and in order to be able to perform a reliable statistical analysis. Water-bubbles on and around the pellets are removed in order to minimize distortions on mean HUs and CNRs close to the measurement ROI.

When focussing on the performance of the iCT and IQon scanners on image quality parameters; HU, noise and CNR are statistically different for similar conventional iCT and IQon acquisitions, shown in Chapter 7. For unaffected pellets, HU values are higher, noise is higher and CNRs are lower for IQon acquisitions compared to iCT acquisitions using 120 and 140 kVp tube voltages and $CTDI_{vol}$ dose-levels of 8, 24 and 40 mGy. When focussing on influence of metal artefacts, the effects of metal artefacts are most pronounced on conventional IQon acquisitions resulting in greater HU, noise and CNR differences relative to values of unaffected pellets. The observed differences are most pronounced in 120-kVp and low-dose acquisitions. These differences can be declared to differences in x-ray filtration between IQon en iCT. The filtration of the IQon is reduced compared to the filtration of iCT. The beam-hardening artefact is larger at reduced filtration resulting in more severe artefacts in IQon acquisitions based on quantitative measurements on mean HUs, noise and CNRs.

With the acquisition-data made on the spectral CT IQon both conventional polychromatic images and monochromatic images can be reconstructed. The virtual monochromatic images can be reconstructed at various energy levels over the full spectrum from 40 to 200 keV. High keV monochromatic imaging results in a

decrease in HU and CNRs. Noise remains relatively constant over the entire keV spectrum. Initially, in 40 keV monochromatic images mean HUs and CNRs are very high and show a decay, shown in Figures 8.3 and 8.5. Mean HUs of unaffected HA pellets are similar at kVp equivalent keVs of approximately 70 and 74 keV for respectively 120 and 140-kVp polychromatic results. For all 6 box configurations the monochromatic images of 200 keV images are least affected by metal artefacts. Monochromatic imaging results in a reduced beam-hardening effect and streak artefacts therefore increasing deviated mean HUs and CNRs values bringing these values back towards baseline values of unaffected pellets. Based on mean HUs, noise and CNR trends obtained from 40-200 keV monochromatic images, a separation into four categories of metal artefacts can be made, which are illustrated in Figures 8.14-8.16. The effectiveness of high keV monochromatic imaging in the reduction of metal artefacts strongly depends on the metallic alloy, the use of bilateral of unilateral prostheses and the distance and location of the pellets relative to the inserted prostheses.

Virtual monochromatic images can provide acceptable image quality parameters relative to conventional 120 and 140-kVp images at similar $CTDI_{vol}$. However, noise is lower and CNR higher for conventional polychromatic IQon results. In the imaging of a metal hip prosthesis, the kVp equivalent monochromatic results show greater HU, noise and CNR deviations from baseline values relative to polychromatic results. Virtual monochromatic imaging has the potential to reduce beam-hardening and streak-artefacts. Virtual high-keV monochromatic imaging itself is most effective in case of moderate artefacts. O-MAR is superior in MAR since absolute corrections towards reference HUs, noise and CNRs are greater for all categories of artefacts. Additionally, O-MAR has no effect on mean HU, noise and CNR in the absence metal artefacts where a great downside of 200 keV monochromatic imaging is the loss in contrast and consequently in CNR in unaffected regions. Virtual high-keV monochromatic imaging can only correct for beam-hardening and streak artefacts and not for metal artefacts caused by photon-starvation, unlike O-MAR. In both MAR approaches, the metal alloy, the use of unilateral or bilateral prostheses and the location and distance of the pellets relative to the prostheses greatly influences the effectiveness in metal artefact reduction. Further clinical evaluation is needed to determine optimal keVs in the CT imaging of metal hip prosthesis in patients due to a substantial loss in overall image contrast and higher influence of Compton scatter at these high keVs. Additionally, dual energy is not sufficient to capture the full absorption spectrum – for example, it does not detect K-edges that are unique to specific materials. In contrast, a next promising step can be energy-sensitive photon counting CT since it measures the full X-ray energy spectrum and thus can be used to detect K-edges, allowing accurate identification of specific materials (59,60). This should also result in improved reduction of beam hardening and scatter artefacts (24).

The use of model-based iterative reconstruction techniques has shown to substantially increasing image quality parameters at similar dose levels, or facilitating ultra-low-dose imaging while maintain sufficient image quality. At the ultra-low-dose of 4 mGy IMR level 1, 2 and 3 show respectively 83%, 89% and 95% lower values in noise relative to standard FBP reconstructions while maintaining acceptable HU values. In case of imaging metal prosthesis, IMR combined with O-MAR significantly improves CNR and reduces noise and metal artefacts in the CT- imaging of MoM-prosthesis. O-MAR is most effective at 140-kVp and when combined with IMR resulting in the greatest HU, noise and CNR corrections towards baseline values. Image quality with IMR is superior compared to FBP and iDose^4 at all dose levels and IMR is capable of maintaining acceptable noise levels even at ultra-low-dose, shown in Chapter 10. Mean HUs and CNRs of unaffected pellets remain acceptable even at a dose of 4 mGy in all iCT acquisitions, thus providing promising dose reduction capabilities in current clinical practice in various CT-protocols.

Our study also encounters weaknesses that we want to address. We only performed quantitative and objective analyses by using a standardized measurement template. Adding subjective image quality scoring by several radiologists could give more insights in the clinical usefulness and additional value of the CT-techniques. The hydroxyapatite pellets with a high density result in high contrast values between the pellets and its background. By adding pellets with different densities or by adding soft tissue, the value of the novel CT-techniques can give more insights in the possible additional clinical value. We addressed metal artefacts and the degree of MAR by quantifying mean HU, noise and CNR values. Despite the fact that these are justified and commonly used image quality parameters, additional analyses of the noise-power spectrum (NPS) and modulation transfer function (MTF) can give more insights in the nature of the noise and spatial resolution.

At the moment, in the CT-imaging of metal hip prosthesis, iCT imaging is superior to IQon imaging since the influence of metal artefacts is less pronounced due to differences in detector technology and filtration and since O-MAR combined with IMR can be used on the iCT system. High-keV monochromatic imaging is capable of reducing metal artefacts by reducing beam-hardening artefacts and streak-artefacts, but poor overall contrast at high keVs and its inability to reduce scatter and photon-starvation artefacts makes O-MAR superior in the reduction of metal artefacts.

In near future, the combination of the novel CT-techniques O-MAR, IMR and Spectral CT seems imaginable. This research fuels the necessity to implement these techniques for Spectral CT. In this way we can fully appreciate the superior way to deal with MAR by monochromatic Spectral CT in combination with handling inevitable photon-starvation. The combination of reducing beam-hardening and streak artefacts using monochromatic imaging, suppressing the effects of photon-starvation with the use of O-MAR and substantially improving overall image quality using the model-based iterative reconstruction technique IMR seems an ultimate subset in the CT-imaging of metallic composites, at a substantially lower radiation dose. Further research and clinical validation is essential to determine the value of these techniques in a clinical setting.

12 Bibliography

1. Pilania K, Jankharia B. Imaging features of complications following hip replacement: A pictorial assay. ECR 2014 poster. 2014;C-2041.

2. Boomsma MF, Warringa N, Kollen BJ, Dalen J van, D. Mueller, Vlassenbroek A, et al. Quantitative analysis of orthopedic metal artifact reduction (O-MAR™) on streak artifacts in CT scans caused by metal-on-metal total hip arthroplasty in a phantom study. Not Publ yet [Internet]. 2015; Available from: http://posterng.netkey.at/esr/viewing/index.php?module=viewing_poster&pi=120966

3. Witt F, Bosker BH, Bishop NE, Ettema HB, Verheyen CCPM, Morlock MM. The Relation Between Titanium Taper Corrosion and Cobalt-Chromium Bearing Wear in Large-Head Metal-on-Metal Total Hip Prostheses. J Bone Jt Surg Am. 2014;96(18).

4. Bosker BH, Ettema HB, van Rossum M, Boomsma MF, Kollen BJ, Maas M, et al. Pseudotumor formation and serum ions after large head metal-on-metal stemmed total hip replacement. Risk factors, time course and revisions in 706 hips. Arch Orthop Trauma Surg [Internet]. 2015 Mar [cited 2015 Feb 18];135(3):417–25. Available from: http://www.ncbi.nlm.nih.gov/pubmed/25663048

5. Han SC, Chung YE, Lee YH, Park KK, Kim MJ, Kim KW. Metal artifact reduction software used with abdominopelvic dual-energy CT of patients with metal hip prostheses: assessment of image quality and clinical feasibility. AJR Am J Roentgenol [Internet]. 2014 Oct [cited 2014 Dec 3];203(4):788–95. Available from: http://www.ncbi.nlm.nih.gov/pubmed/25247944

6. Li H, Noel C, Chen H, Li HH, Low D, Moore K, et al. Clinical evaluation of a commercial orthopedic metal artifact reduction tool for CT simulations in radiation therapy. Med Phys. 2012;39(December):7507–17.

7. Morsbach F, Bickelhaupt S, Wanner GA. Reduction of Metal Artifacts from Hip Prostheses on CT Images of the Pelvis : Value of. Radiology. 2013;268(1):237–44.

8. Kidoh M, Nakaura T, Nakamura S, Tokuyasu S, Osakabe H, Harada K, et al. Reduction of dental metallic artefacts in CT: value of a newly developed algorithm for metal artefact reduction (O-MAR). Clin Radiol [Internet]. The Royal College of Radiologists; 2014 Jan [cited 2014 Dec 3];69(1):e11–6. Available from: http://www.ncbi.nlm.nih.gov/pubmed/24156796

9. Hilgers G, Nuver T, Minken A. The CT number accuracy of a novel commercial metal artifact reduction algorithm for large orthopedic implants. J Appl Clin Med Phys. 2014;15(1):274–8.

10. Yu L, Leng S, Kofler JM, Vrieze TJ, Fletcher J, McCollough CH. Virtual Monochromatic Imaging in Dual-energy CT: Radiation Dose, Image Quality, and Clinical Applications. Dep Radiol Mayo Clin Coll Med Mayo Clin Rochester, MN. 2012;2012 Mayo.

11. Goodsitt MM, Christodoulou EG, Larson SC. Accuracies of the synthesized monochromatic CT numbers and effective atomic numbers obtained with a rapid kVp switching dual energy CT scanner. Med Phys. 2011;38:2222–32.

12. Raupach R, Becker CR, Johnson TR, Krauss B, Flohr T, Schmidt B. Metal artifact reduction for dual source dual energy computed tomographyIn: Hricak H, ed. 96th Scientific Assembly and Meeting of the Radiological Society of North America. Oak Brook, Radiol Soc North Am. 2010;

13. Bamberg F, Dierks A, Nikolaou K, Reiser MF, Becker CR, Johnson TR. Metal artifact reduction by dual energy computed tomography using monoenergetic extrapolation. Eur Radiol. 2011;21:1424–9.

14. Bruesewitz M., Yu L, Leng S, Kofler J, Vrieze T, Fletcher J, et al. Virtual Monochromatic Imaging in Dual-energy CT: Radiation Dose, Image Quality, and Clinical Applications. Dep Radiol Mayo Clin Coll Med Mayo Clin Rochester, MN. 2012;Mayo Found.

15. Sagara Y, Hara AK, Pavlicek W, Silva AC, Paden RG, Wu Q. Abdominal CT: comparison of low-dose CT with adaptive statistical iterative reconstruction and routine-dose CT with filtered back projection in 53 patients. AJR Am J Roentgenol [Internet]. 2010 Sep [cited 2014 Oct 22];195(3):713–9. Available from: http://www.ncbi.nlm.nih.gov/pubmed/20729451

16. Nakaura T, Nakamura S, Maruyama N, Funama Y, Awai K, Harada K, et al. Low Contrast Agent and Radiation Dose Protocol for Hepatic Dynamic CT of Thin Adults at 256 – Detector Row CT : Effect of Low Tube Voltage and Hybrid. 2012;264(2):445–54.

17. Huang Y, Zhao T, Jiang Y, Liu Y, Zhao Y, Xu K. Knowledge based iterative reconstruction technique reduces noise and improves image quality for low dose thyroid CT. EPOS 2014. 2014;1–8.

18. Funama Y, Taguchi K, Utsunomiya D, Oda S, Katahira K, Tokuyasu S, et al. Image quality assessment of an iterative reconstruction algorithm applied to abdominal CT imaging. Phys Med [Internet]. Elsevier Ltd; 2014 Jun [cited 2014 Nov 27];30(4):527–34. Available from: http://www.ncbi.nlm.nih.gov/pubmed/24662097

19. Halpern EJ, Gingold EL, White H, Read K. Evaluation of coronary artery image quality with knowledge-based iterative model reconstruction. Acad Radiol [Internet]. Elsevier Ltd; 2014 Jun [cited 2014 Nov 27];21(6):805–11. Available from: http://www.ncbi.nlm.nih.gov/pubmed/24809321

20. Oda S, Utsunomiya D, Funama Y, Katahira K, Honda K, Tokuyasu S, et al. A knowledge-based iterative model reconstruction algorithm: can super-low-dose cardiac CT be applicable in clinical settings? Acad Radiol [Internet]. Elsevier Ltd; 2014 Jan [cited 2014 Oct 30];21(1):104–10. Available from: http://www.ncbi.nlm.nih.gov/pubmed/24331272

21. Oda S, Weissman G, Vembar M, Weigold WG. Iterative model reconstruction: improved image quality of low-tube-voltage prospective ECG-gated coronary CT angiography images at 256-slice CT. Eur J Radiol [Internet]. Elsevier Ireland Ltd; 2014 Aug [cited 2014 Nov 27];83(8):1408–15. Available from: http://www.ncbi.nlm.nih.gov/pubmed/24873832

22. Molteni R. From CT Numbers to Hounsfield Units in Cone Beam Volumetric Imaging: the effect of artifacts. 62th AAOMR - Chicago 2011.

23. Joseph P, Spital R. The effects of scatter in x-ray computed tomography. Med Phys. 1982;9(4):464–72.

24. Boas FE, Fleischmann D. CT artifacts: causes and reduction techniques. Imaging Med [Internet]. 2012 Apr;4(2):229–40. Available from: http://www.futuremedicine.com/doi/abs/10.2217/iim.12.13

25. Mehta D, Thompson R, Morton T, Dhanantwari A, Shefer E, Healthcare P. Iterative Model Reconstruction: Simultaneously Lowered Computed Tompgraphy Radiation Dose and Improved Image Quality.

26. Hanson KM. Noise and contrast discrimination in computed tomography. Radiol skull brain. 1981;5(1):3941–56.

27. Yu L, Leng S. Image Reconstruction Techniques. Am Coll Radiol [Internet]. 2010;(November):1–3. Available from: www.imageqisely.org

28. White paper: Knowledge-Based Iterative Reconstruction New Era Image quality and dose. p. 15.

29. Gaizo AJ Del, Silva AC, Hara AK. The utility of dual-energy computed tomography in abdominal imaging. Appl Radiol [Internet]. 2014; Available from: http://www.appliedradiology.com/articles/the-utility-of-dual-energy-computed-tomography-in-abdominal-imaging

30. Vlassenbroek A. Clinical outcome of novel CT reconstruction techniques. Oral presentation 2014 p. 53.

31. White paper: iDose 4 iterative reconstruction technique.

32. Gordon R. Three-Dimensional Reconstruction from Projections: A Review of Algorithms". ternational Rev Cytol. 1974;38.

33. Xu J, Mahesh M, Tsui BM. s iterative reconstruction ready for MDCT? J Am Coll Radiol. 2009;6(4):274–6.

34. Xie Q, Wu J, Tang Y, Dou Y, Hao S, Xu F, et al. Whole-Organ CT Perfusion of the Pancreas : Impact of Iterative Reconstruction on Image Quality , Perfusion Parameters and Radiation Dose in 256-Slice CT- Preliminary Findings. 2013;8(11):4–11.

35. Schilham A. Clinical studies on IR in CT. Oral presentation 2013;

36. White paper: Knowledge-Based Iterative Reconstruction Technique. :1–11.

37. Li Q, Yu H, Jiang Y, Liu SY. Comparison of image quality between knowledge based iterative reconstruction and filtered back projection techniques in evaluation of pulmonary diffuse disease with thin-section CT. EPOS 2014. 2014;C-2065:10.

38. Löve a, Olsson M-L, Siemund R, Stålhammar F, Björkman-Burtscher IM, Söderberg M. Six iterative reconstruction algorithms in brain CT: a phantom study on image quality at different radiation dose levels. Br J Radiol [Internet]. 2013 Nov [cited 2014 Nov 27];86(1031):1–11. Available from: http://www.pubmedcentral.nih.gov/articlerender.fcgi?artid=3830436&tool=pmcentrez&rendertype=abstract

39. Vlassenbroek A, Millon D, Michoux N, Coche E. Low contrast detectability improvements with iterative reconstructions of multi detector computed tomography images: a phantom study. Poster # 2073 ECR 2014. 2014;

40. Philips. White paper: Metal Artifact Reduction for Orthopedic Implants (O-MAR) [Internet]. [cited 2014 Apr 12]. Available from: http://clinical.netforum.healthcare.philips.com/us_en/Explore/White-Papers/CT/Metal-Artifact-Reduction-for-Orthopedic-Implants-(O-MAR)

41. Philips. White paper:Iterative-techniques-for- reducing-metal-artifacts-in-CT-scanning [Internet]. [cited 2014 Apr 16]. Available from: http://clinical.netforum.healthcare.philips.com/us_en/Explore/White-Papers/CT/Iterative-techniques-for- reducing-metal-artifacts-in-CT-scanning

42. Kalender WA. Computed Tomography: Fundamentals, System Technology, Image Quality, Applications. 3rd Editio. 2011.

43. Kalender WA. Basic Principles of Dual Energy CT [Internet]. 2011. Available from: http://www.imp.uni-erlangen.de/ECR2011/Kalender ECR 2011 NH8 DECTsw.pdf

44. Vlassenbroek A. Dual Layer CT. Med Radiol. 2011;21–34.

45. Macari M, Graser A, Katz DS. Invited Commentary of Dual-energy multidetector CT: How does it work, what can it tell us, and when can we use it in abdominopelvic imaging? Radiographics. 2010;(August):1052–5.

46. Alvarez R, Makovski A. Energy-selective reconstructions in x-ray computed tomography. Phys Med Biol. 1976;21:733–44.

47. Vlassenbroek A. Spectral Detector CT (SDCT). Oral presentation 2013 p. 1–50.

48. Meinel F, Bischoff B, Zhang Q, Bamberg F, Reiser M, Johnson T. Metal artifact reduction by dual-energy computed tomography using energetic extrapolation: a systematically optimized protocol. Invest Radiol. 2012;47(7):406–14.

49. National Institute of Standards and Technology's [Internet]. [cited 2014 Jun 25]. Available from: http://www.nist.gov/pml/data/xraycoef/index.cfm

50. Menke J. Radiology Comparison of Different Body Size Parameters for Individual Dose Adaptation in Body CT of Adults 1. 2005;(8):10–4.

51. Langton D. The Incidence of Adverse Reactions to Metal Debris (ARMD) Following Hip Resurfacing. Acad Orthop Surg. 2010;

52. Biomet [Internet]. [cited 2014 Jan 21]. Available from: http://www.biomet.com/patients/m2a_magnum.cfm

53. Ceramtec [Internet]. [cited 2014 Nov 3] Available from: http://www.ceramtec.com/ceramic-materials/biolox/delta/

54. Hounsfield G. Computed Medical Imaging Nobel Lecture. J Radiol. 1980;61(7):459–68.

55. University of Michigan [Internet]. [cited 2014 Apr 21] Available from: http://www.umich.edu/~ners580/ners-bioe_580/labs/_printViews/10-Image-B-prt.htm

56. Edens MA. Oral scource. 2014.

57. Kim H, Park CM, Song YS, Lee SM, Goo JM. Influence of radiation dose and iterative reconstruction algorithms for measurement accuracy and reproducibility of pulmonary nodule volumetry: A phantom study. Eur J Radiol [Internet]. Elsevier Ireland Ltd; 2014 May [cited 2014 Nov 27];83(5):848–57. Available from: http://www.ncbi.nlm.nih.gov/pubmed/24572380

58. Lee YH, Park KK, Song H-T, Kim S, Suh J-S. Metal artefact reduction in gemstone spectral imaging dual-energy CT with and without metal artefact reduction software. Eur Radiol [Internet]. 2012 Jun [cited 2014 Dec 3];22(6):1331–40. Available from: http://www.ncbi.nlm.nih.gov/pubmed/22307814

59. Iwanczyk J, Nygard E, Meirav O. Photon Counting Energy Dispersive Detector Arrays for X-ray Imaging. IEEE Trans Nucl Sci. 2009;56(3):535–42.

60. Boll D, Patil N, Paulson E. Focal cystic high-attenuation lesions: characterization in renal phantom by using photon-counting spectral CT--improved differentiation of lesion composition. Radiology. 2010;254(1):270–6.

61. Virgina Mason Medical Centre [Internet]. [cited 2014 Apr 3]. Available from: https://www.virginiamason.org/images/orthopedics/hip_joint_replace.jpg

13 Appendix A

Spectral results of Box 2, 4, 5 and 6

13.1.1 Spectral results of Box 2

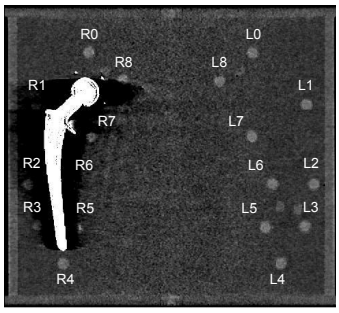

Figure 13.1: Box 2 including the 18 ROI

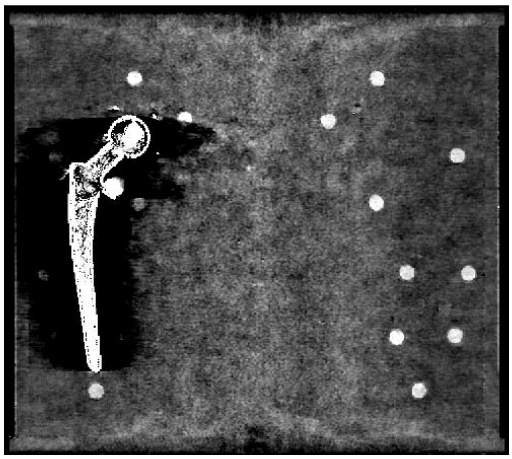

a) 40 keV

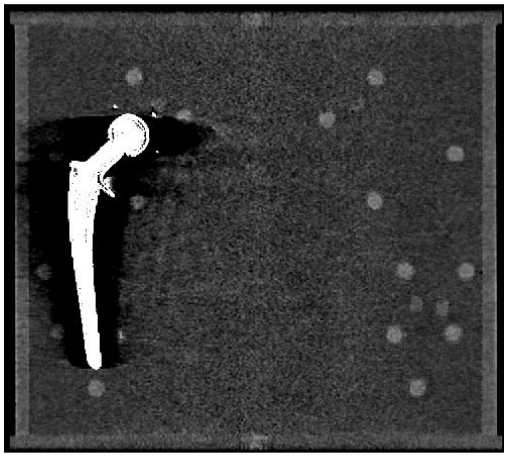

b) 70 keV

c) 140 keV

d) 200 keV

Figure 13.2: Monochromatic images of Box 2 at 40, 70, 140 and 200 keV

In order to focus on the effect of Spectral CT imaging regarding metallic hip prostheses, only results of the relevant right side of the phantom are evaluated.

HU analysis

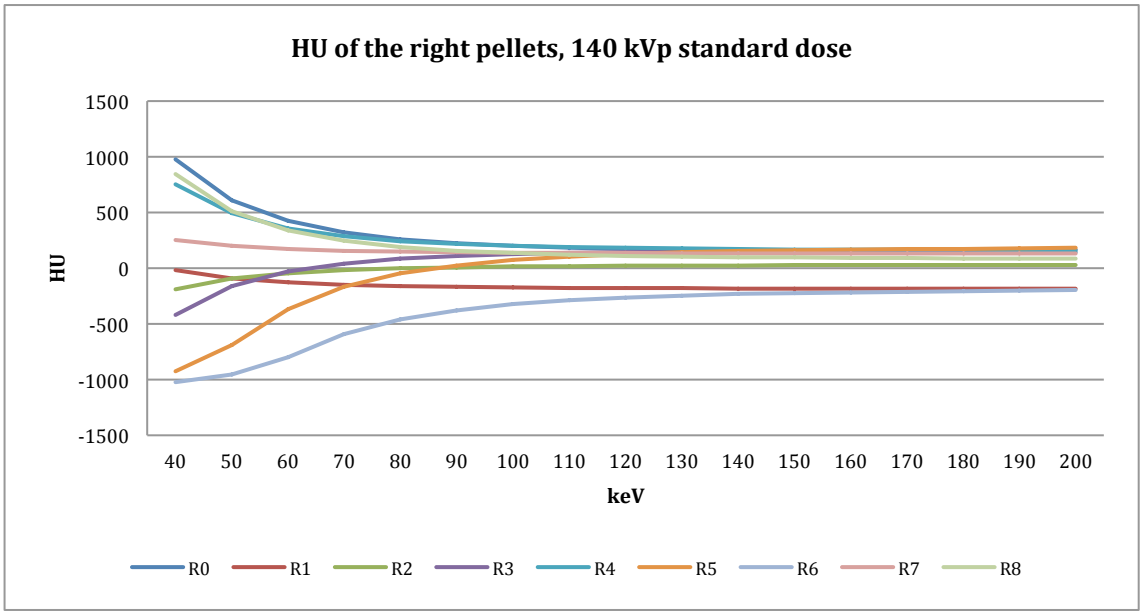

Figure 13.3: Average HU trends of the right pellets

Pellet R0 and R4 are unaffected by metal artefacts and HU values show the described decreasing trend in case of Box 1. Pellets R5 and R6 show a positive effect when extrapolating to higher keV where HU and CNR increase to a certain steady state from around 140 / 150 keV. HU values of R5 and R6 do not reach HU values of unaffected pellets. Pellet R8 seems to be affected based on the images illustrated in Figure 13.3, but HU values are as high as reference values of the unaffected pellets R0 and R4. Pellet R2 and R3 show a slight increase in HU values with increasing keVs, where pellet R1 and R7 show a slight decrease of HU values.

Noise analysis

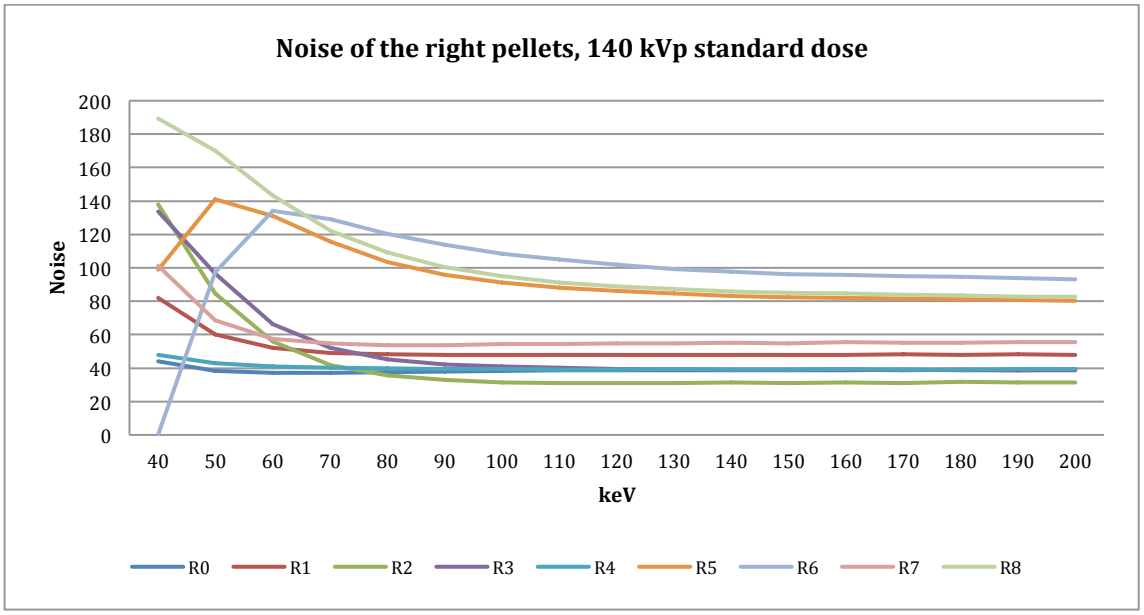

Figure 13.4: Average noise of the right pellets.

Average noise of pellets R0 and R4 are low and remain constant as expected. Pellet R5 an R6 show an interesting trend where initially an increase in noise is observed and a decrease from approximately 50-60 keV but still to high noise levels. Noise level of pellet R8 is very high and remains high at approximately the noise level of R5 and R6. Noise levels of the remaining pellets are clearly lower.

CNR analysis

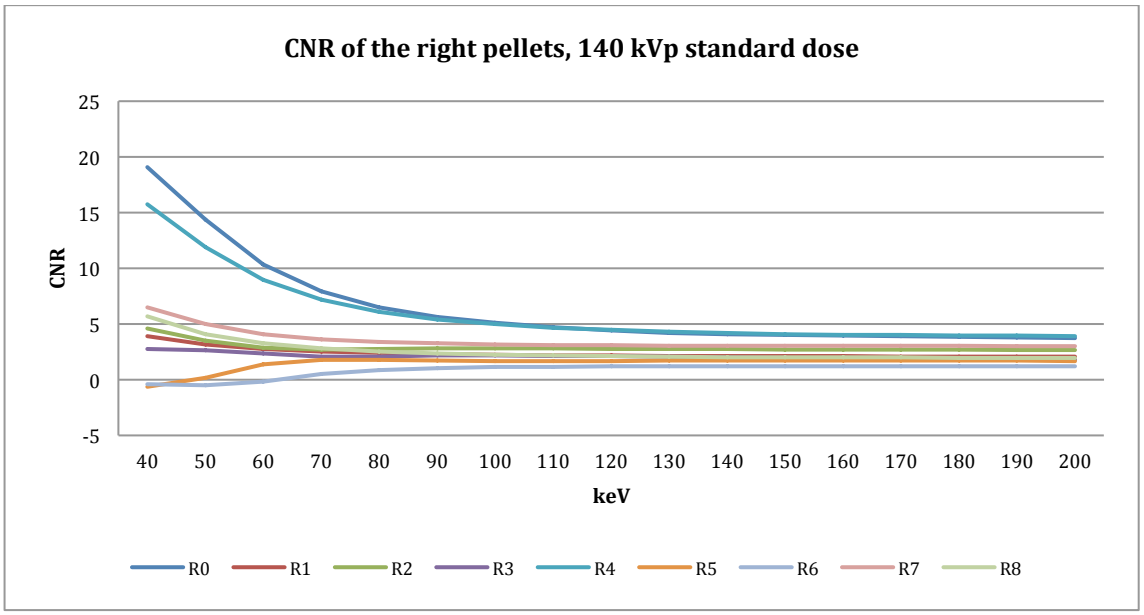

Figure 13.5: Average CNR of the right pellets.

CNR of R5 and R6 significantly increase when extrapolating to higher keV but as with HU values not to baseline levels of unaffected pellets. CNR of pellet R0 and R4 is initially high as expected, and decreases exponentially. When focussing on the remaining pellets a slight decrease in CNR is seen with increasing keVs.

13.1.2 Spectral results of Box 4

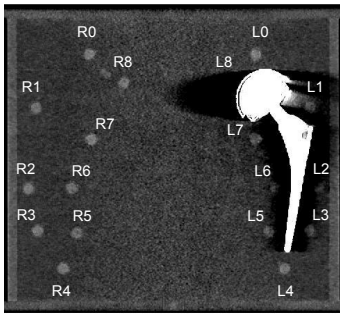

Figure 13.6: Box 4 including the 18 ROIs

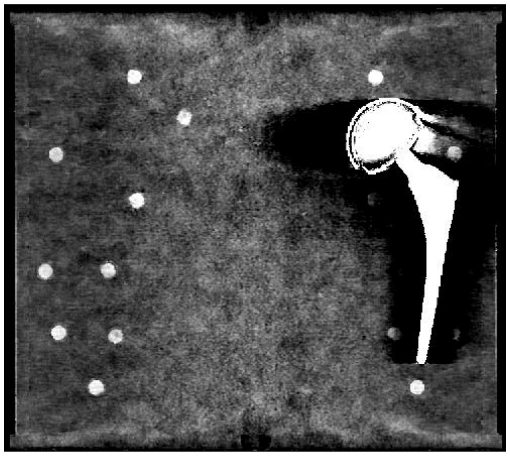

a) 40 keV

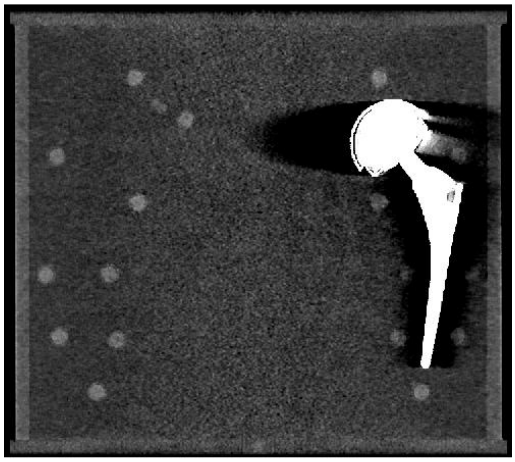

b) 70 keV

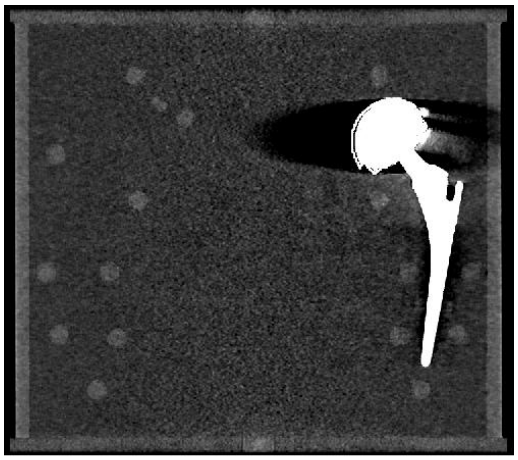

c) 140 keV

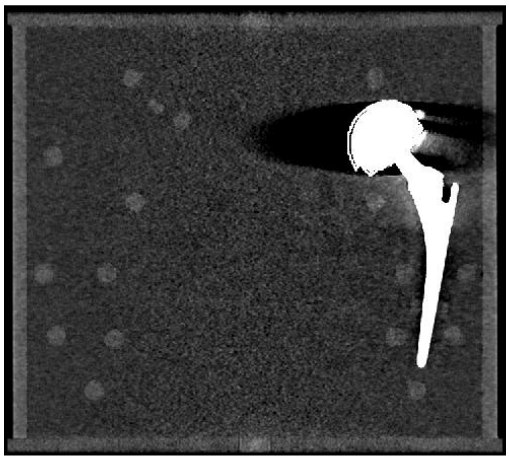

d) 200 keV

Figure 13.7: Monochromatic images of Box 4 at 40, 70, 140 and 200 keV.

HU analysis – left side

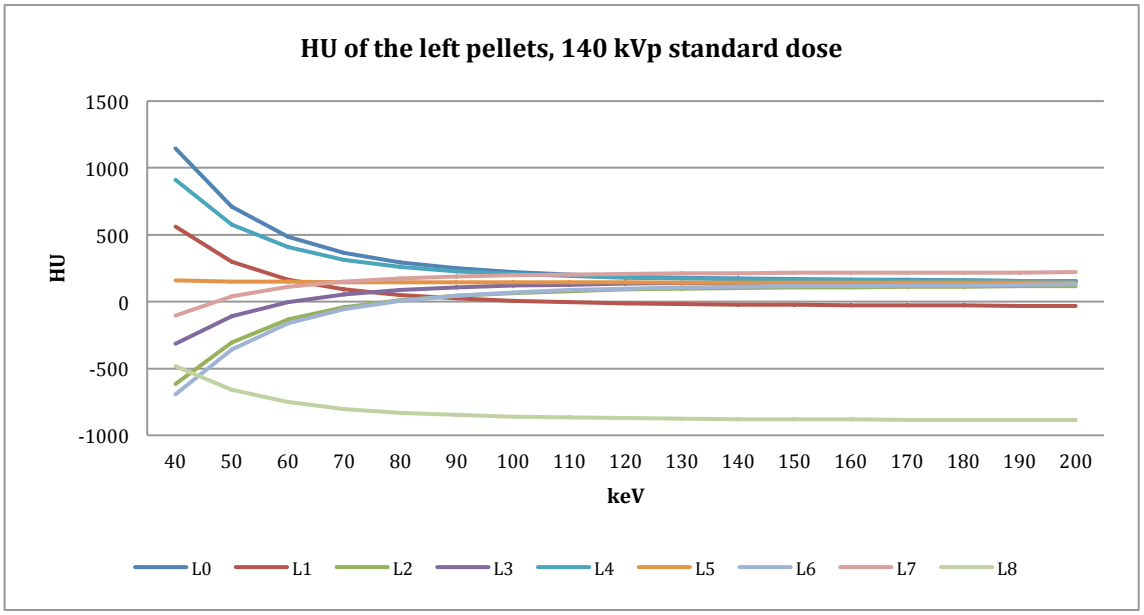

Figure 13.8: Average HU of the left pellets.

HU value of pellet L8 is very low and decreases even further at higher keV levels as with Box 3. HU values of pellet L2, L3, L6 and L7 increase with increasing keV. HU values of pellet L5 are low and remain constant over the full keV spectrum. HU values of pellet L1 are lowered and decrease further with increasing keV.

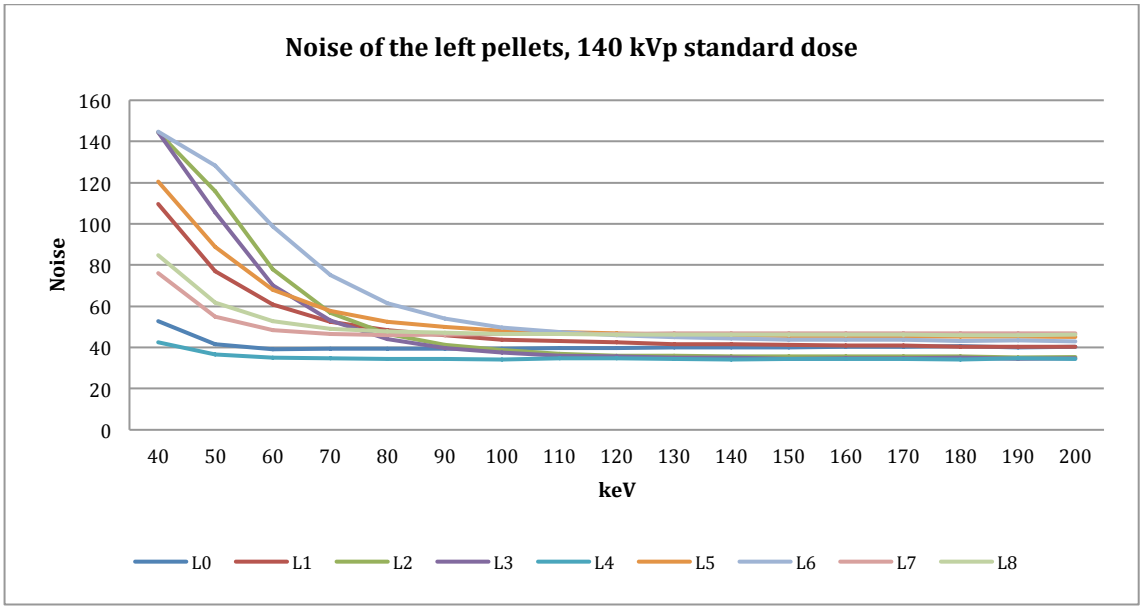

Figure 13.9: Average noise of the left pellets.

Noise analysis – left side

The noise of the left pellets show the same trends as for the left side of Box 3 where noise levels are lowered for all pellets when extrapolating to higher keV.

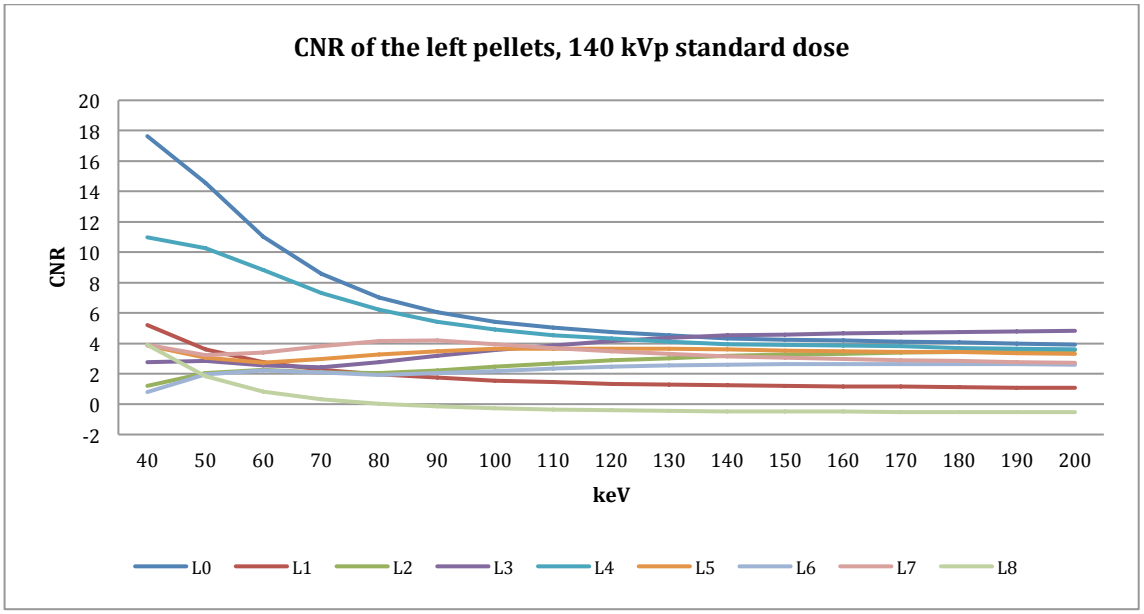

Figure 13.10: Average CNR of the left pellets.

CNR analysis – left side

CNR values of L0 and L4 decrease with increasing keV where CNR of pellet L4 is lower, especially at low keV. Severely affected pellet L8 shows a decreasing CNR with increasing keV. CNR of L2, L3 and L6 show increase with increasing keV. Pellet L5 and L7 show variable behaviour with increasing keV. Pellet L1 shows a decreasing CNR with increasing keV.

13.1.3 Spectral results of Box 5

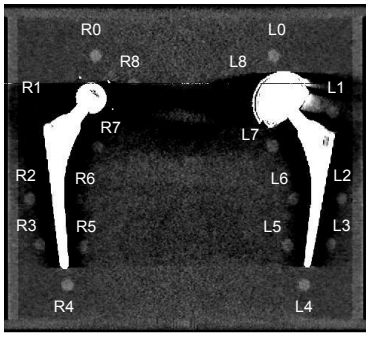

Figure 13.11: Box 5 including all 18 ROIs.

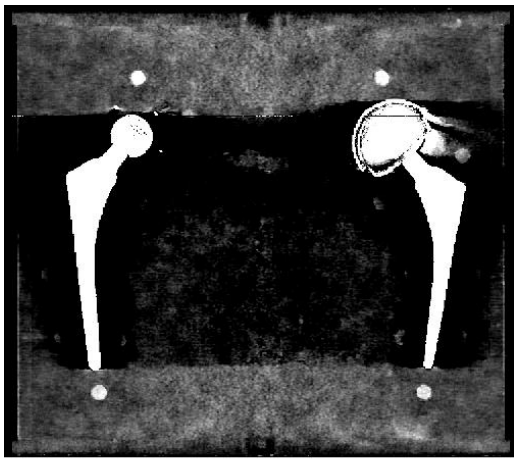

a) 40 keV

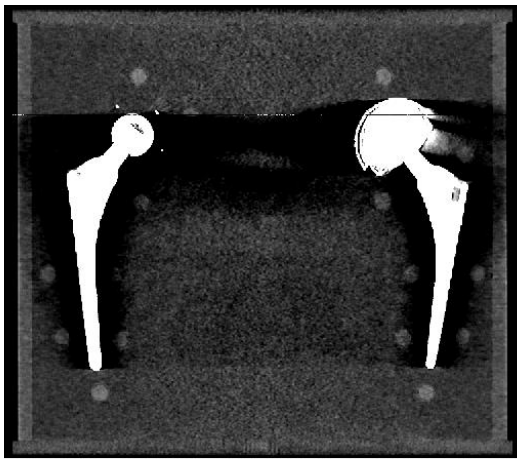

b) 70 keV

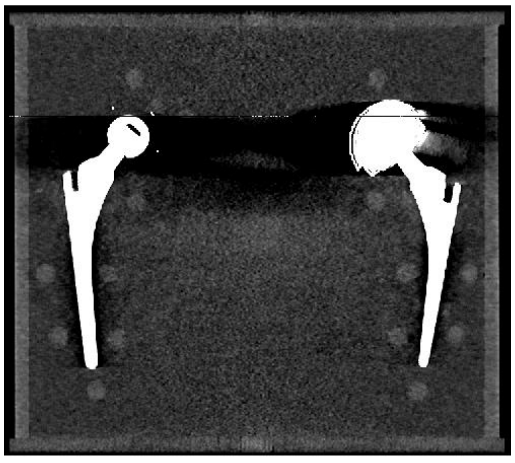

c) 140 keV

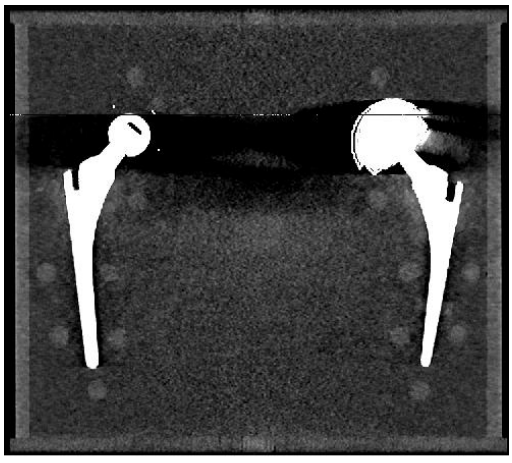

d) 200 keV

Figure 13.12: Monochromatic images of Box 5 at 40, 70, 140 and 200 keV.

HU analysis – left side

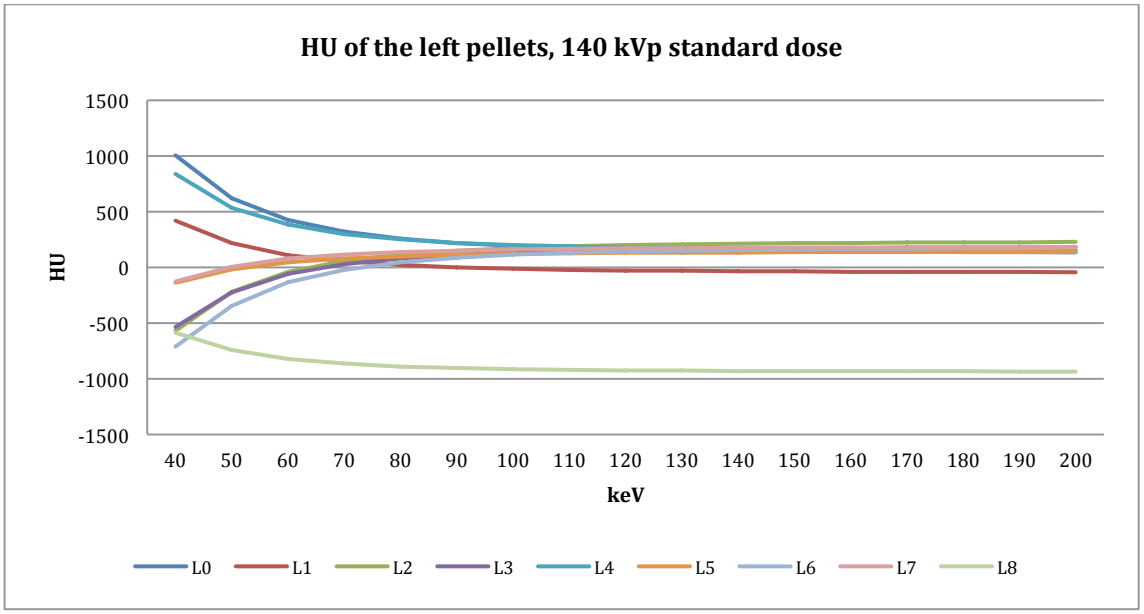

Figure 13.13: Average HU of the left pellets.

The same trends are observed as for the left side of Box configuration 4 where HU values are slightly lower due to the influence of the contralateral prosthesis.

Noise analysis – left side

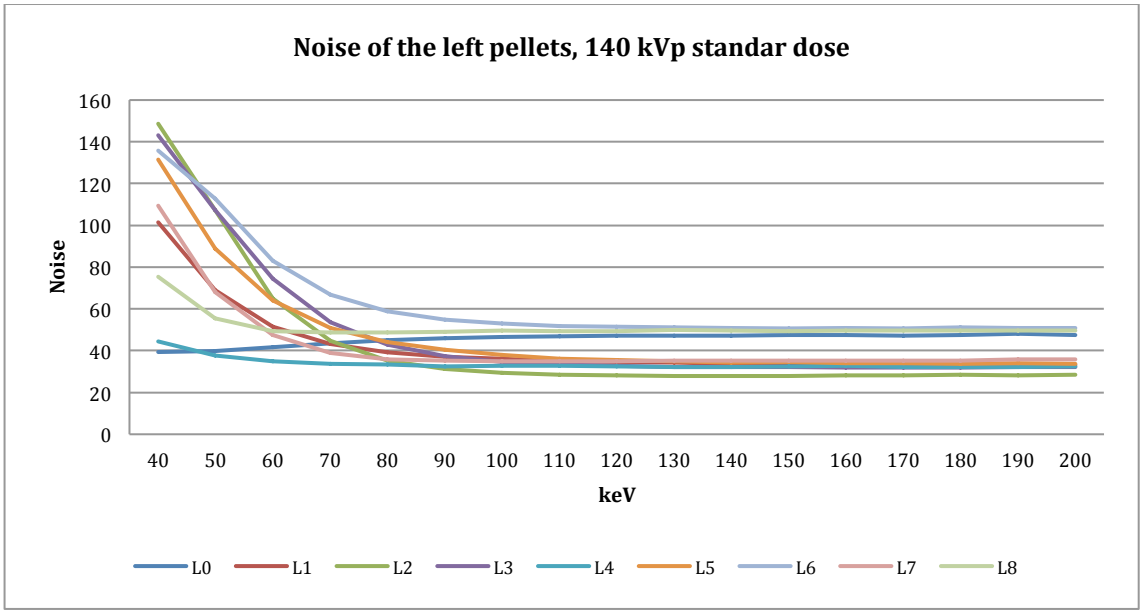

Figure 13.14: Average noise of the left pellets.

Noise trends are similar to those regarding Box configuration 4.

CNR analysis – left side

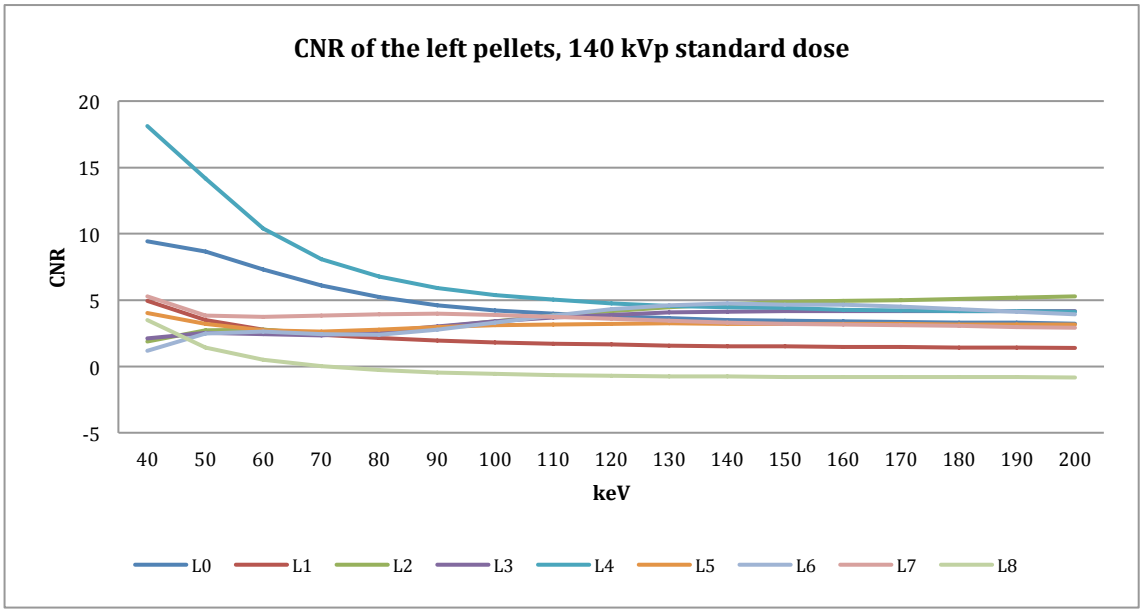

Figure 13.15: Average CNR of the left pellets.

CNR trends are similar to those regarding Box configuration 4.

HU analysis – right side

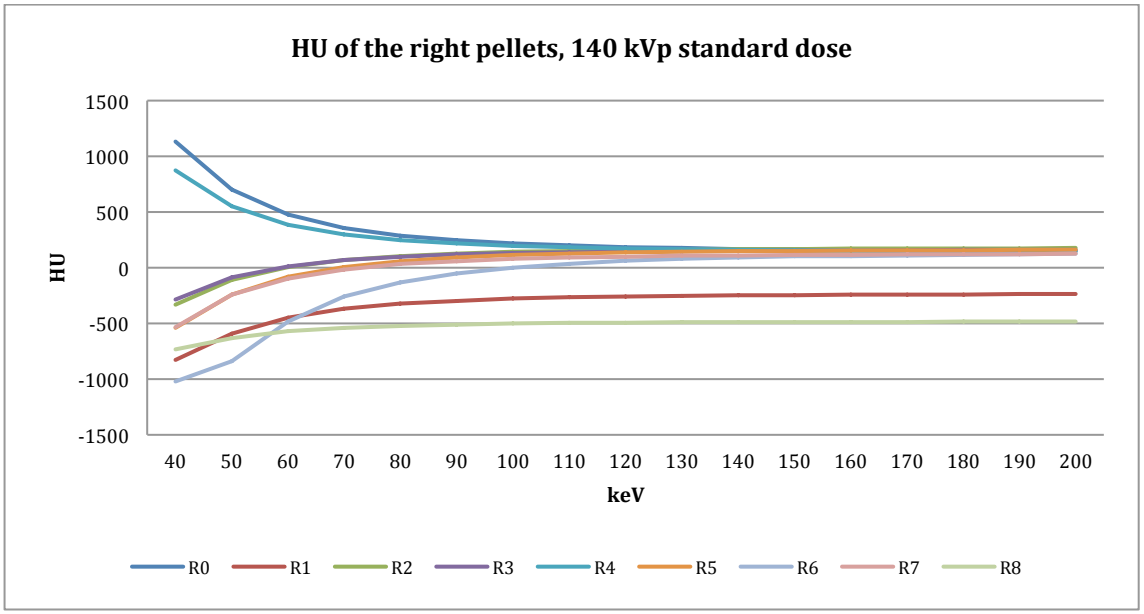

Figure 13.16: Average HU of the right pellets.

As for all box configurations HU and CNR of pellets L0 and L4 are unaffected and show decreasing HU with increasing keV. All other pellets show increasing HU values with increasing keV where HU of pellet R1 and R8 do not return to baseline levels. These pellets seem to be affected by the large MoM head located at the contralateral side.

Noise analysis – right side

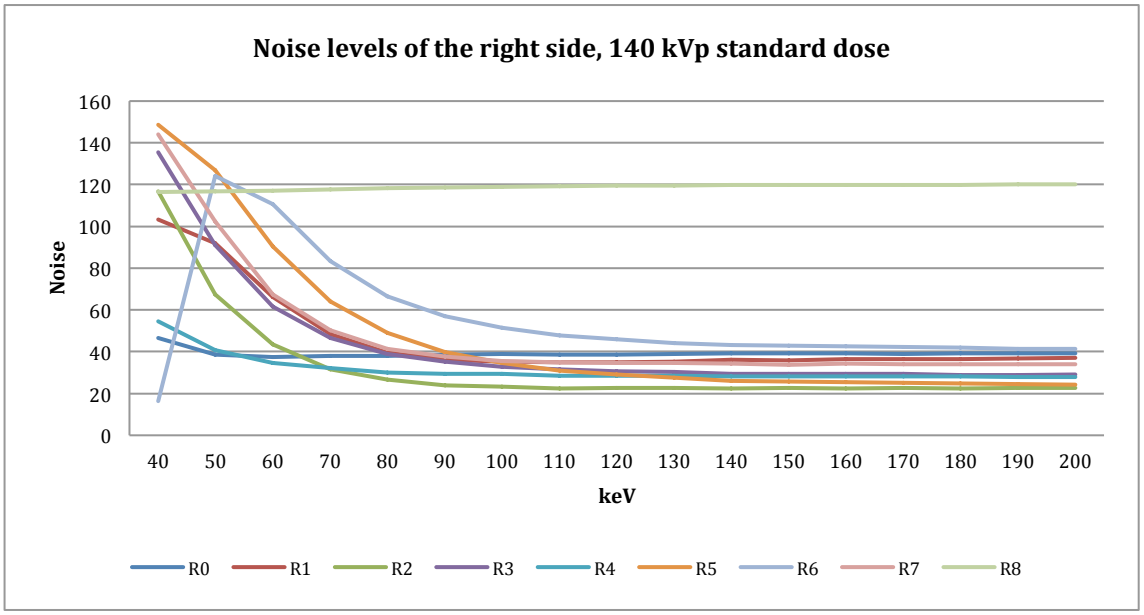

Figure 13.17: Average noise of the right pellets.

Noise levels of pellet R6 and R8 stand out. Noise of pellet R8 is high and remains totally constant throughout the entire spectrum. Noise of R6 is very low initially and increases heavily till approximately 55 keV. From 55 keV till 200 keV the noise decreases just as the other pellets.

CNR analysis – right side

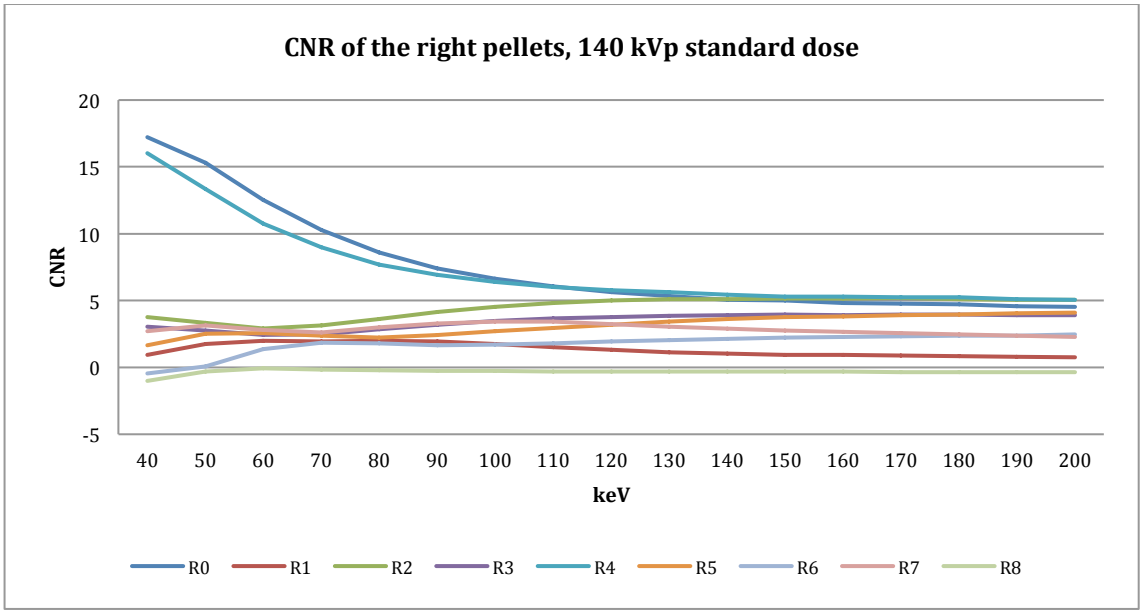

Figure 13.18: Average CNR of the right pellets.

CNR values of R1 and R8 decrease with increasing keV as for pellets R0 and R4. The other pellets show increasing CNR with increasing keV where pellet R6 and R7 do not return to baseline levels of unaffected pellets.

13.1.4 Spectral results of Box 6

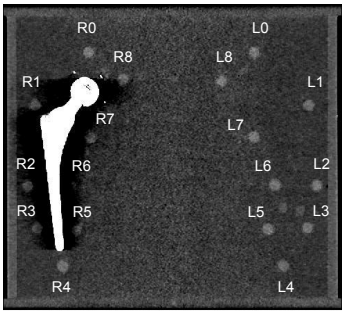

Figure 13.19: Box 6 including 18 ROIs.

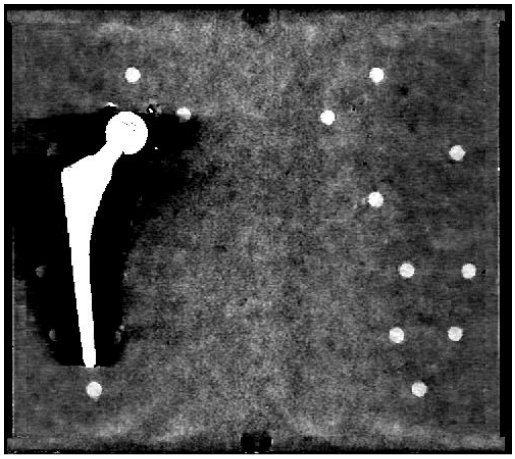

a) 40 keV

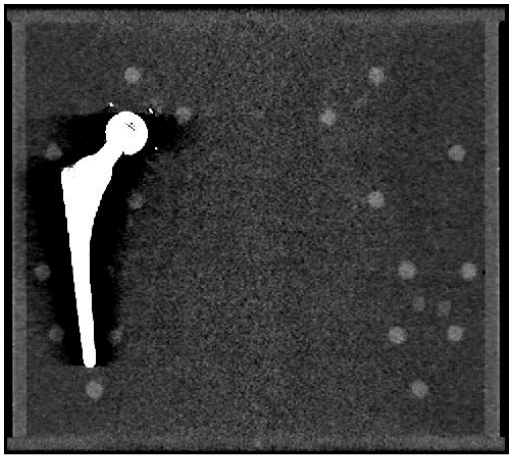

b) 70 keV

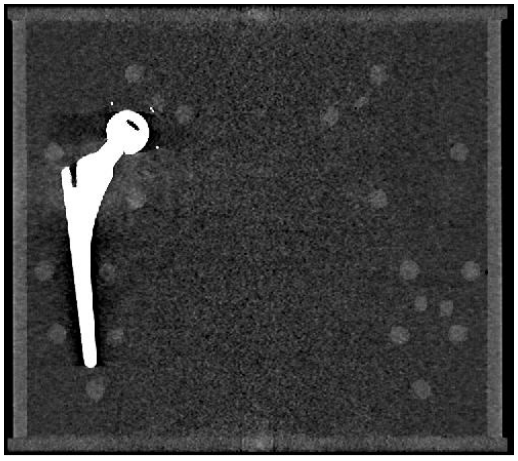

c) 140 keV

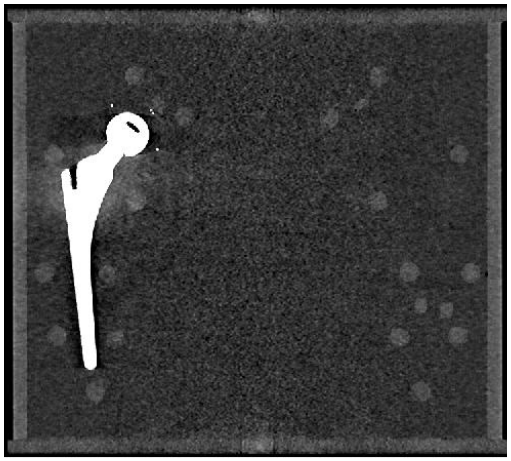

d) 200 keV

Figure 13.20: Monochromatic images of Box 6 at 40, 70, 140 and 200 keV.

HU analysis – right side

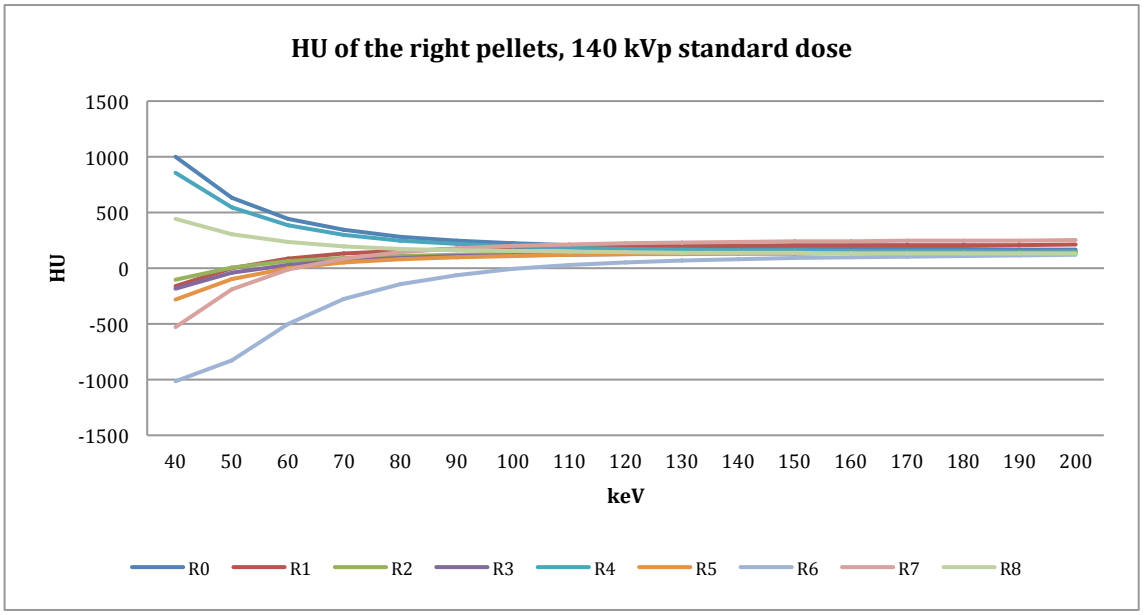

Figure 13.21: Average HU of the right pellets.

HU of pellet R8 are slightly affected where baseline HU is a factor 2 lower than pellet R0 and R4. Pellet R6 is moderately affected and shows a great HU improvement with increasing keV. Pellets R1, R2, R3, R5 show an increase in HU with increasing keV and all return to baseline HU.

Noise analysis – right side

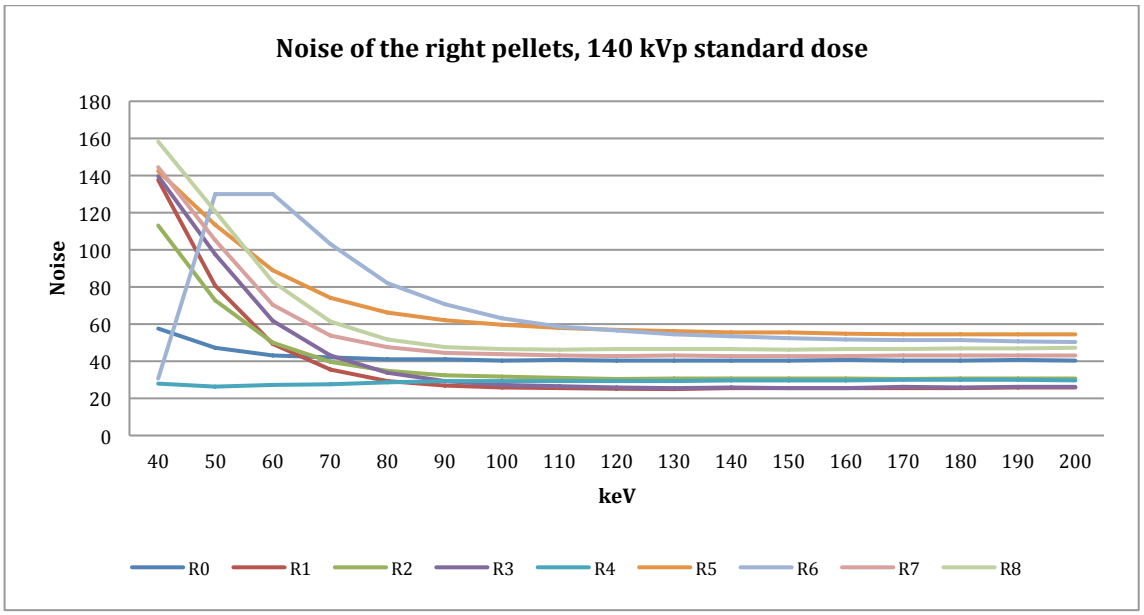

Figure 13.22: Average noise of the right pellets.

The same trends are observed as for the right side of box configuration 5. The only difference observed in noise trends is pellet R8 that is no longer affected by a contralateral prosthesis as for box configuration 5.

CNR analysis – right side

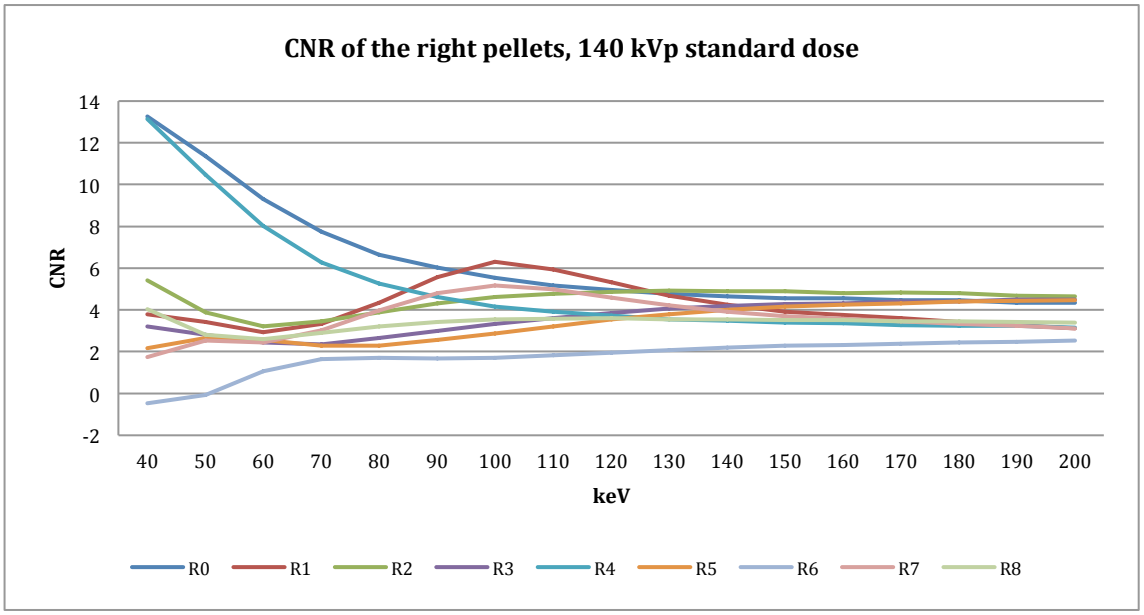

Figure 13.23: Average CNR of the right pellets.

Pellet R1 and R7 show a variable effect with increasing keV where CNR increases from 40 up to 100 keV. Starting from 100 keV, CNR of pellet R2 and R7 decrease. CNR of pellets R2, R3, R5 and R8 initially decrease and increase from 60 keV till 200 keV. Pellet R6 shows the greatest improvement in CNR.

14 Appendix B

14.1 HU values of pellet R6 from high to ultra-low-dose

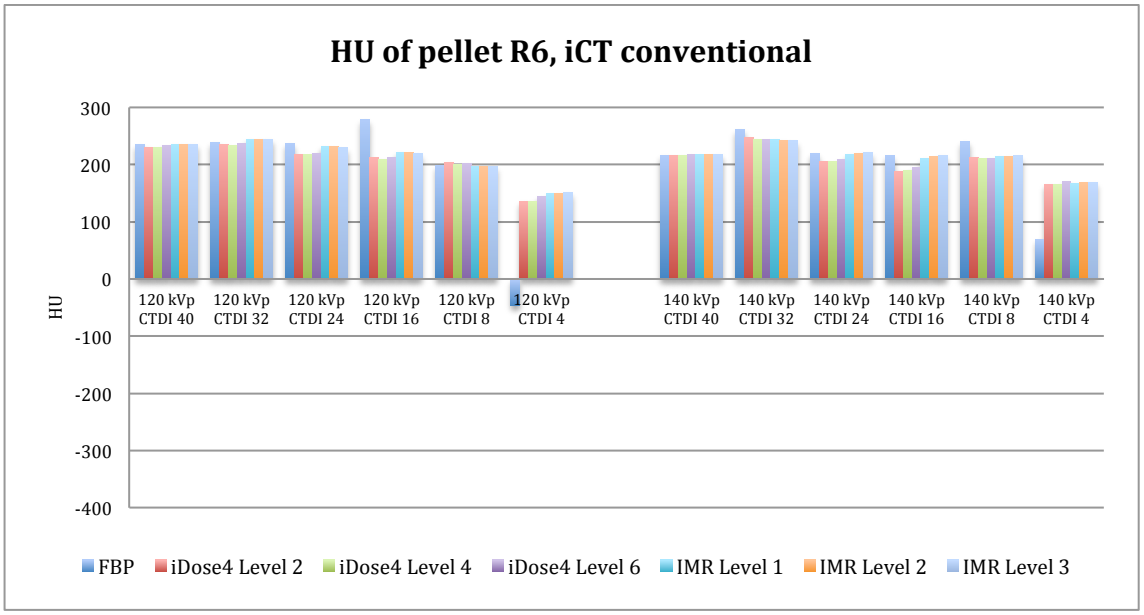

Figure 14.24: iCT conventional; average HU value of pellet R6 at 120 and 140 kVp and at 40, 32, 24, 16, 8 and 4 mGy.

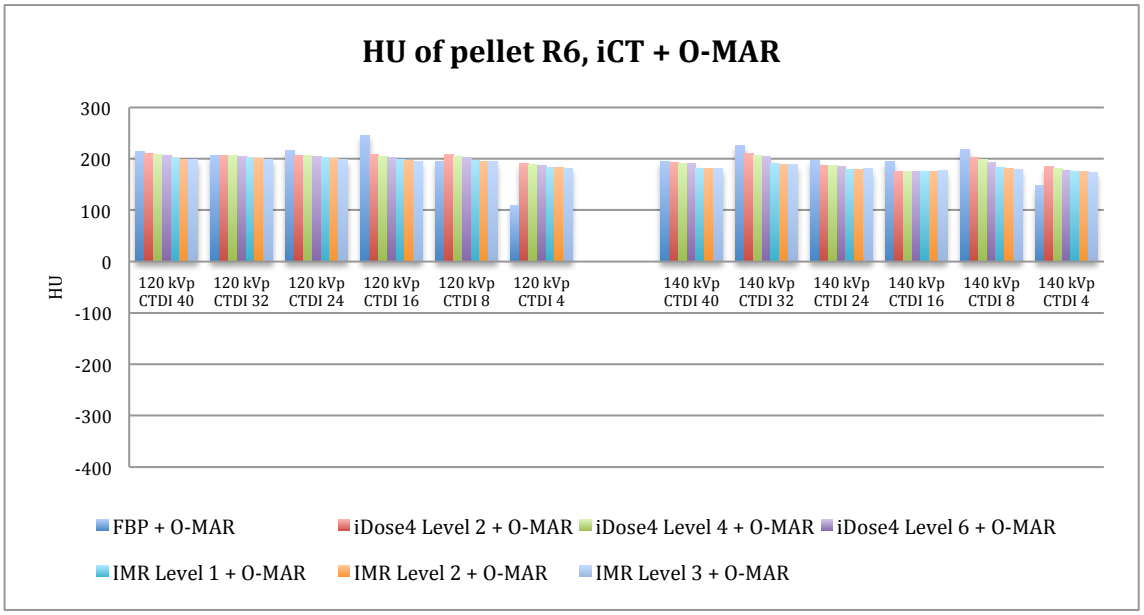

Figure 14.25: iCT conventional + O-MAR; average HU value of pellet R6 at 120 and 140 kVp and at 40, 32, 24, 16, 8 and 4 mGy.

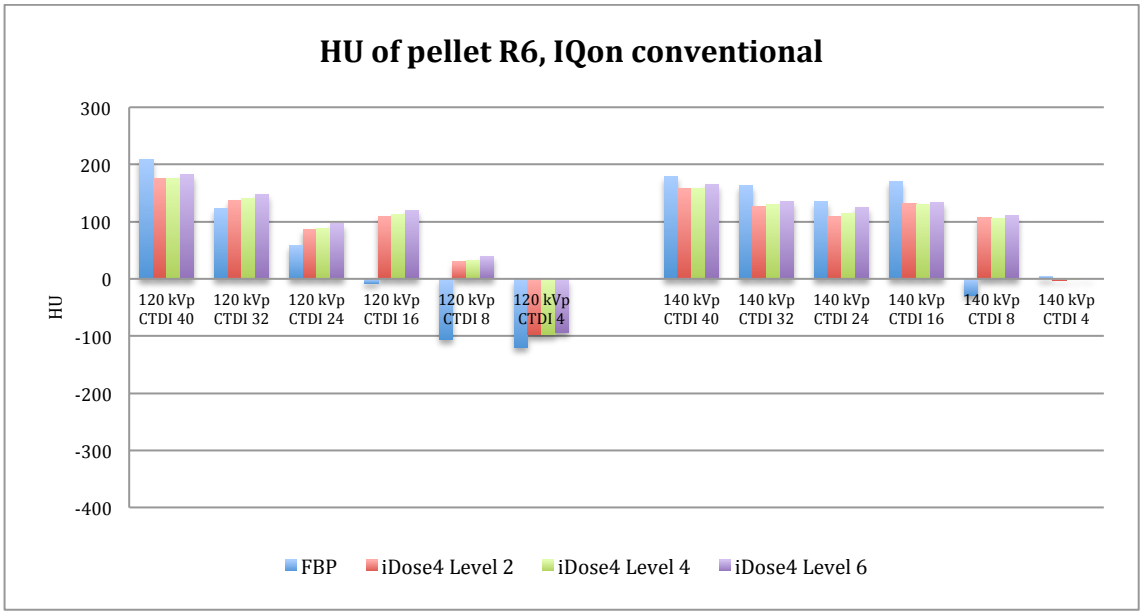

Figure 14.26: IQon conventional; average HU value of pellet R6 at 120 and 140 kVp and at 40, 32, 24, 16, 8 and 4 mGy.

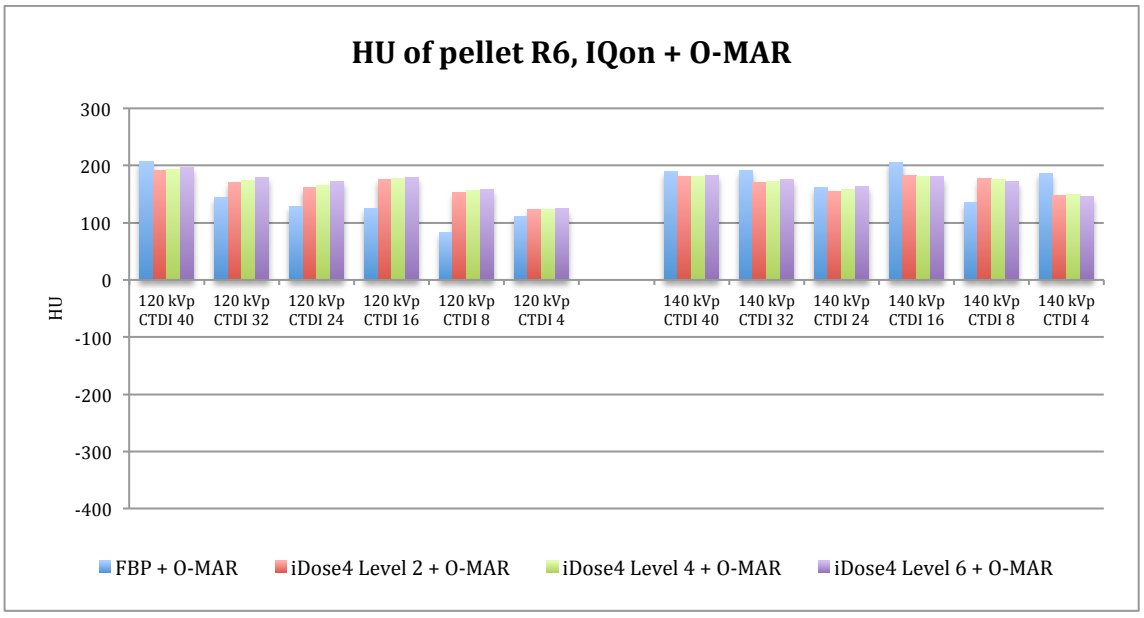

Figure 14.27: IQon conventional + O-MAR; average HU value of pellet R6 at 120 and 140 kVp and at 40, 32, 24, 16, 8 and 4 mGy.

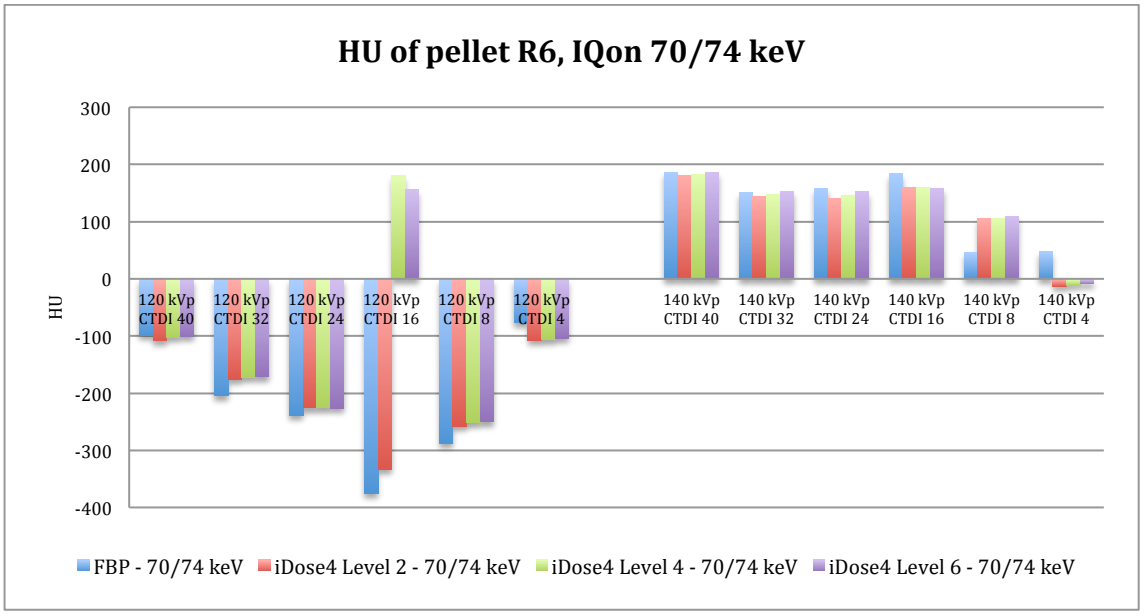

Figure 14.28: Monochromatic IQon results at 74 keV; average HU value of pellet R6 at 120 and 140 kVp and at 40, 32, 24, 16, 8 and 4 mGy.

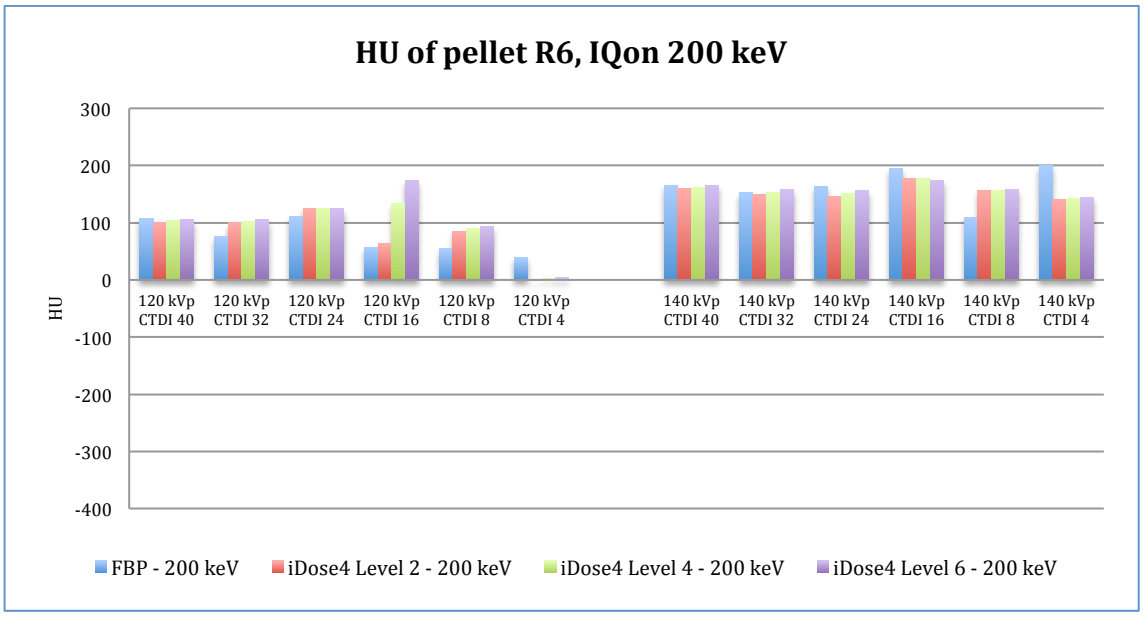

Figure 14.29: Monochromatic IQon results at 200 keV; average HU value of pellet R6 at 120 and 140 kVp and at 40, 32, 24, 16, 8 and 4 mGy.

14.2 CNR values of pellet R6 from high to ultra-low-dose

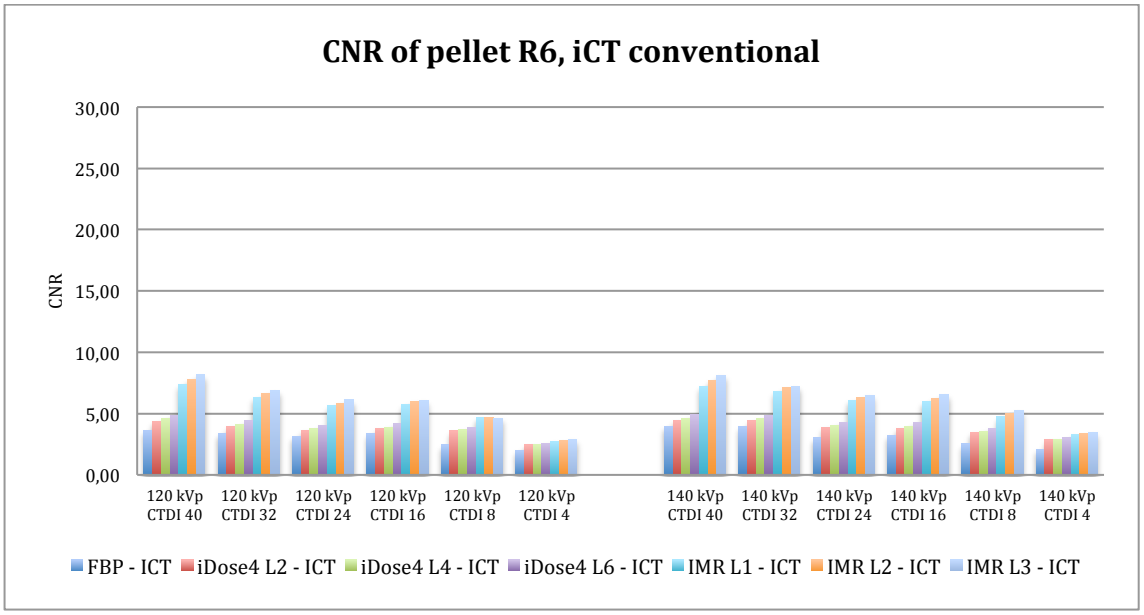

Figure 14.30: iCT conventional; average CNR value of pellet R6 at 120 and 140 kVp and at 40, 32, 24, 16, 8 and 4 mGy.

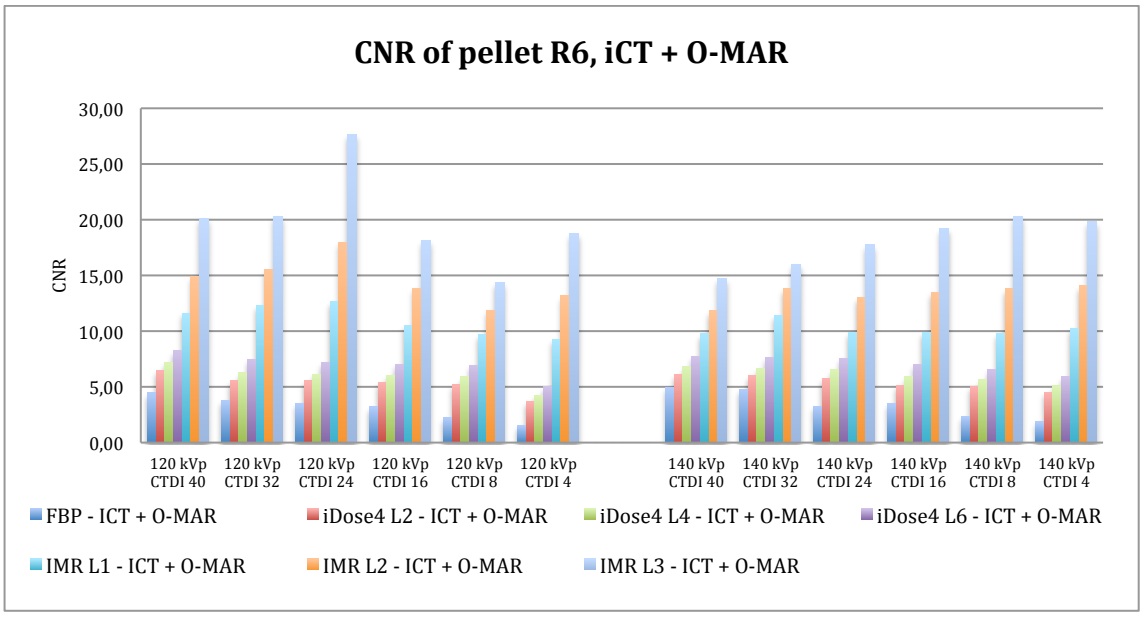

Figure 14.31: iCT conventional + O-MAR; average CNR value of pellet R6 at 120 and 140 kVp and at 40, 32, 24, 16, 8 and 4 mGy.

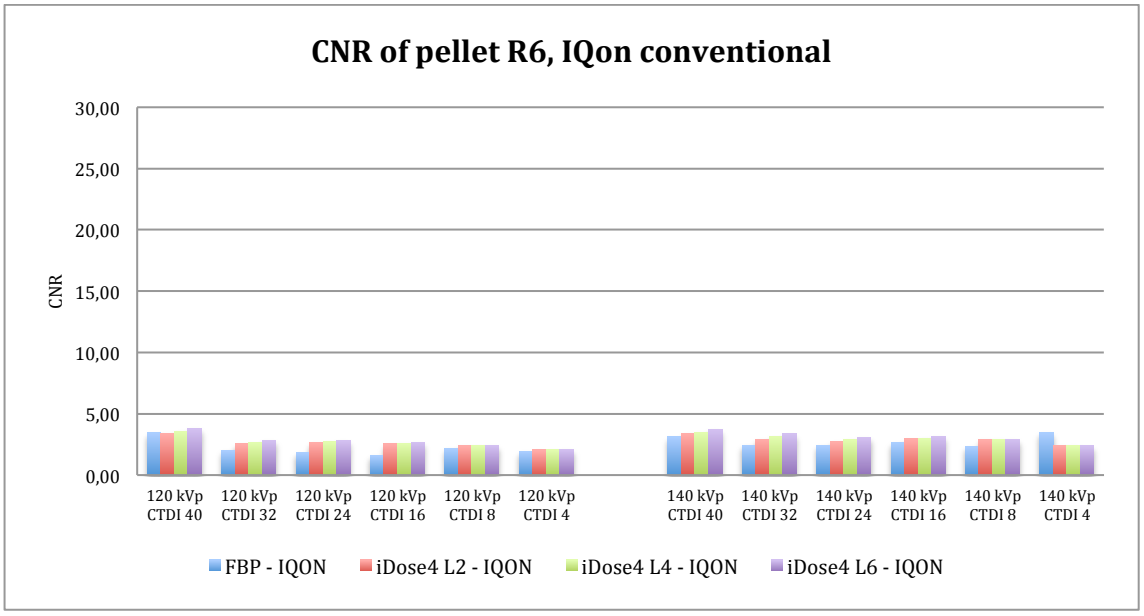

Figure 14.32: IQon conventional; average CNR value of pellet R6 at 120 and 140 kVp and at 40, 32, 24, 16, 8 and 4 mGy.

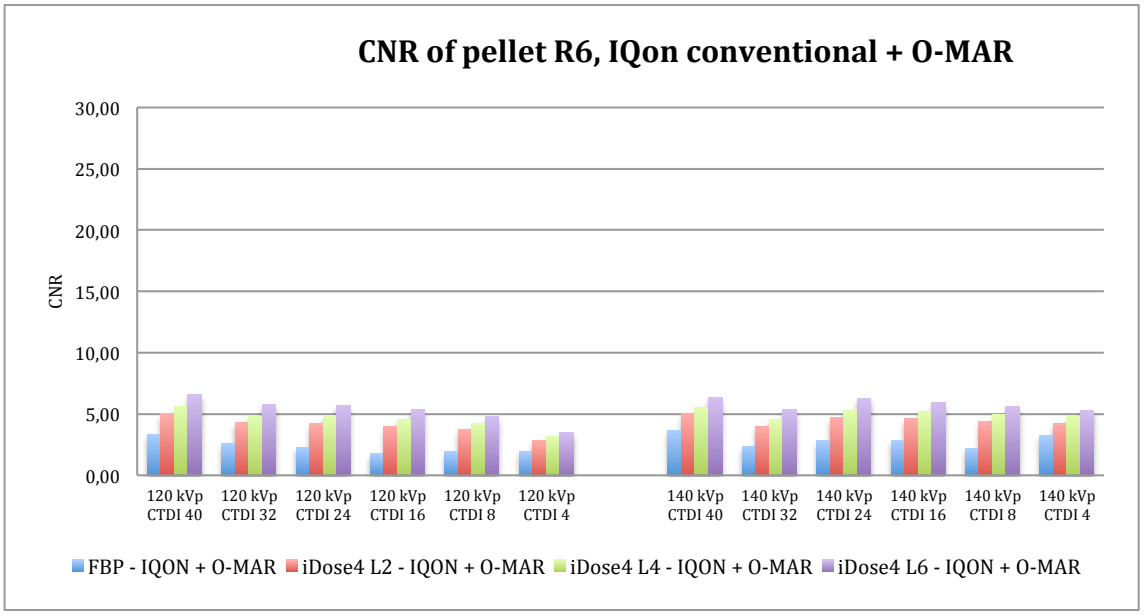

Figure 14.33: IQon conventional + O-MAR; average CNR value of pellet R6 at 120 and 140 kVp and at 40, 32, 24, 16, 8 and 4 mGy.

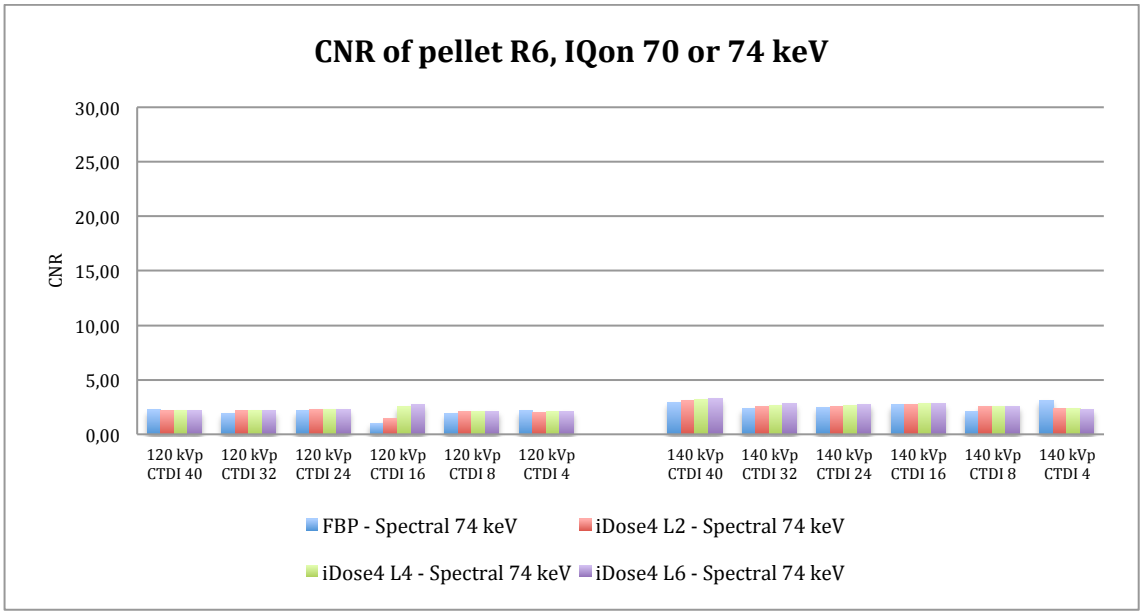

Figure 14.34: Monochromatic IQon results at 74 keV; average CNR value of pellet R6 at 120 and 140 kVp and at 40, 32, 24, 16, 8 and 4 mGy.

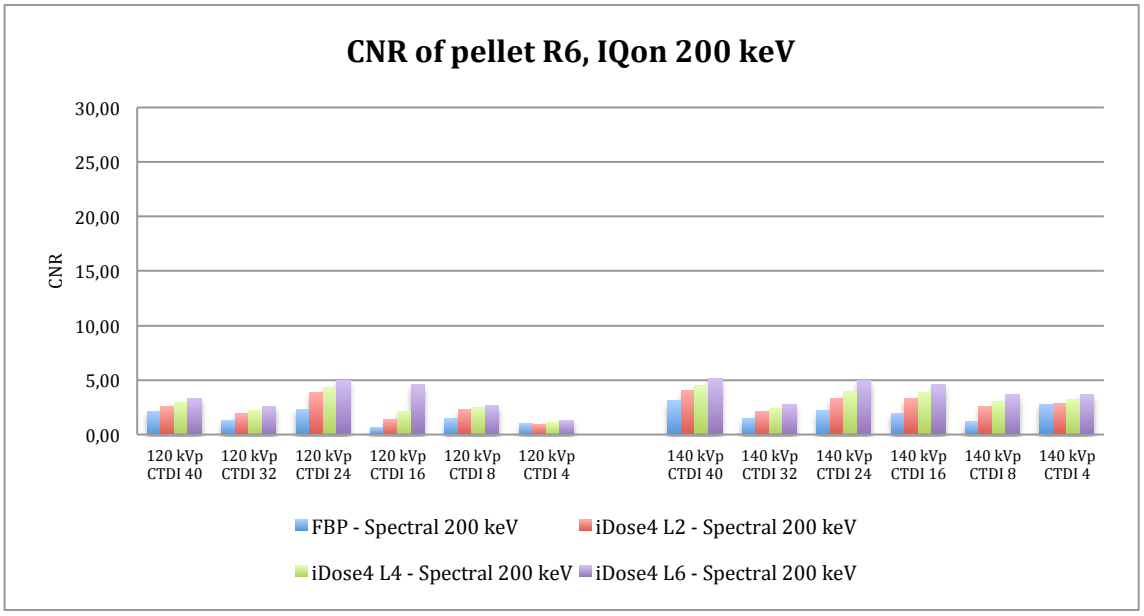

Figure 14.35: Monochromatic IQon results at 200 keV; average CNR value of pellet R6 at 120 and 140 kVp and at 40, 32, 24, 16, 8 and 4 mGy.